

Copyright
by
Matthew John Ramos
2018

**The Dissertation Committee for Matthew John Ramos
certifies that this is the approved version of the following dissertation:**

**Quantification of Static and Dynamic Mechanical Anisotropy in
Fractured and Layered Rock Systems: Experimental Measurement and
Numerical Modeling**

Committee:

Stephen Laubach, Supervisor

David Nicolas Espinoza, Co-Supervisor

Kyle Spikes

Nicola Tisato

Scott Tinker

**Quantification of Static and Dynamic Mechanical Anisotropy in
Fractured and Layered Rock Systems: Experimental Measurement and
Numerical Modeling**

by

Matthew John Ramos

Dissertation

Presented to the Faculty of the Graduate School of

The University of Texas at Austin

in Partial Fulfillment

of the Requirements

for the Degree of

Doctor of Philosophy

The University of Texas at Austin

August 2018

Acknowledgements

This work was funded by the Statoil Fellows Program at the University of Texas at Austin awarded to Matthew John Ramos in the Jackson School of Geosciences. Additional resources for microCT imaging were provided by the Chevron Digital Petrophysics Laboratory at UT Austin. I would like to thank my co-supervisor, Dr. D. Nicolas Espinoza and Dr. Stephen Laubach for their support, motivation, and mentorship. I would also like to thank my dissertation committee for their technical insight and guidance, and Sara Elliot and Stephanie Forstner for their assistance in SEM analyses.

Abstract

Quantification of Static and Dynamic Mechanical Anisotropy in Fractured and Layered Rock Systems: Experimental Measurement and Numerical Modeling

Matthew John Ramos, Ph.D.

The University of Texas at Austin, 2018

Co-Supervisors: Stephen Laubach and David Nicolas Espinoza

Shales often exhibit mechanical anisotropy, which directly impacts the accuracy of seismic imaging and the geomechanical response to drilling and completions. Anisotropy is often caused by mineralogical layering, fractures, and rock fabric. However, the relative impact of each of these features on static and dynamic measurements is not well understood. We utilize simultaneous triaxial stress-testing and ultrasonic monitoring, in addition to CT and SEM imaging to highlight the impacts of rock type (sandstone, dolomite, shale), confining stress, stress loading path (isotropic and deviatoric), lithological heterogeneity and layering, and fractures (pre-existing and stress-induced) on static and dynamic mechanical properties and rock failure. We show that: (1) changes in shear wave anisotropy during deviatoric loading are evidence of the onset of microfracturing in isotropic rocks. This new dynamic method is valuable because it detects stress-induced damage before the typical static method (dilatancy), allowing for rock failure property estimation while still preserving sample competence for future tests. (2) The deviatoric stress-dependence of anisotropic static and dynamic mechanical properties can be estimated by combining measurements from several cores as a function of the % of peak stress. Samples exhibit strength variability due to layering orientation and heterogeneity. Therefore, using % of peak stress rather than the stress magnitude ensures that measurements are combined from samples undergoing similar deformational processes (i.e., primarily elastic vs plastic strains). (3) Rock mechanical properties vary with applied stress and the presence of fractures. Thus, dynamic-static transforms must not only account for anisotropy, but also stress-induced changes in anisotropy and rock damage. (4) The relative impacts of layering and fractures on shale velocity anisotropy can be decoupled and modeled by combining CT and SEM imaging to develop mineralogically and structurally heterogeneous velocity models. Quantifying the contribution of these features to overall anisotropy provide an avenue for evaluating subsurface variations in rock heterogeneity (i.e., spatial changes in natural fracturing). Overall, this study evidences the complexity of rock mechanical behavior, which dictates robust mechanical characterization to accurately predict a rock's response to human-induced stress changes during hydrocarbon exploitation.

Table of Contents

List of Tables	viii
List of Figures	x
List of Symbols	xiii
1. Introduction.....	1
1.1 Motivation.....	1
1.2 Objectives and Dissertation Outline	6
2. Experimental Methods.....	9
2.1 Rock Types	9
2.2 Triaxial Load Frame, Ultrasonic Monitoring.....	13
2.3 Stress Paths and Testing Conditions.....	14
2.4 X-ray Micro-computed Tomography.....	16
2.5 Scanning Electron Microscopy	17
3. Theoretical Background.....	18
3.1 Calculation of Static and Dynamic Mechanical Properties	18
3.2 Combining Measurements from Multiple Cores to Evaluate Deviatoric Stress Dependence.....	25
4. The Use of Shear-Wave Anisotropy to Quantify the Onset of Stress-Induced Microfracturing	27
4.1 Chapter Abstract	27
4.2 Introduction.....	28
4.3 Calculation of Shear-wave Anisotropy.....	32
4.4 Results.....	32
4.4.1 Shear-Wave Crossover (SWX)	35
4.4.2 Berea Sandstone: SWX, PPD and peak strength	36
4.4.3 Silurian Dolomite: SWX, PPD and peak strength	38
4.5 Analysis and Discussion	39
4.5.1 Onset of damage from shear-wave anisotropy and dilatancy	39
4.5.2 Evolution of dynamic and static moduli with deviatoric loading and induced damage	43
4.5.3 Effect of micro and macro fractures on shear-wave anisotropy	45

4.6	Conclusions.....	49
5.	Stress-Dependent Dynamic-Static Transforms of Anisotropic Mancos Shale	51
5.1	Chapter Abstract	51
5.2	Introduction.....	52
5.3	Results.....	54
5.3.1	Case 1: Effects of Confining Stress on Non-Fractured Samples	54
5.3.2	Case 2: Effects of Pre-Existing Fractures	57
5.4	Discussion.....	60
5.4.1	Effect of Plastic Strains and Stress-Induced Damage on Dynamic -Static Transforms	60
5.4.2	Effects of Pre-Existing Fractures on Dynamic-Static Transforms	62
5.4.3	Accurate Horizontal Stress Determination	64
5.5	Conclusions.....	65
5.6	Supporting Information.....	66
6.	Quantifying Static and Dynamic Stiffness Anisotropy and Nonlinearity in Finely Laminated Shales: Experimental Measurement and Modeling	69
6.1	Chapter Abstract	69
6.2	Introduction.....	70
6.3	Results and Analysis.....	73
6.3.1	Strain Response to Isotropic and Deviatoric Loading	73
6.3.2	Nonlinear Dynamic and Static Stiffness during Isotropic Loading	75
6.3.3	Nonlinear Dynamic and Static Stiffness During Deviatoric Loading	79
6.4	Discussion.....	84
6.4.1	Inability of isotropically derived nonlinear coefficients to predict deviatoric nonlinearity	84
6.4.2	Impact of layering and heterogeneity on stress-strain response	86
6.4.3	Field Implications	89
6.5	Conclusions.....	90
6.6	Supporting Information.....	92
7.	Microstructural Controls on Elastic Anisotropy of Finely Laminated Mancos Shale..	101
7.1	Chapter Abstract	101
7.2	Mancos Shale Characterization.....	102
7.2.1	Elastic Anisotropy.....	105

7.2.2 Mineralogical Variations Measured from SEM.....	108
7.2.3 Structural Variability from X-ray Micro-Computed Tomography.....	110
7.3 Methods for Developing Mineralogically and Structurally Heterogeneous Velocity Models.....	110
7.3.1 Combining SEM and CT Imaging Results	112
7.3.2 Wave Propagation Modeling	118
7.4 Results and Analysis.....	120
7.4.1 Synthetic Layered Models	120
7.4.2 CT Models of Oriented Cores.....	120
7.4.3 CT Models at 13 μm Resolution Testing the Impacts of Layering and Fractures.....	123
7.4.4 SEM Models at 0.9 μm Resolution Testing the Impacts of Layering and Fractures.....	126
7.5 Discussion.....	129
7.5.1 Impact of Model Type on Velocities	129
7.5.2 Impact of SEM Resolution on Velocities	129
7.5.3 Impact of CT Resolution on Velocities	131
7.5.4 Insights into the Controls on Shale Velocity Anisotropy	132
7.6 Conclusions.....	133
7.7 Supporting Information.....	134
8. Conclusions.....	137
8.1 SWX for Identifying the Onset of Stress-Induced Damage.....	137
8.2 Using % of Peak Failure Stress From Oriented Cores to Evaluate the Deviatoric Stress Dependences of Anisotropic Mechanical Properties.....	138
8.3 Dynamic-Static Transforms	138
8.4 Microstructural Controls on Elastic Anisotropy	139
Appendix: Recommendation for Best Practices: Sample Preparation and Laboratory Measurements	141
References.....	141

List of Tables

Table 4-1 Berea Sandstone and Silurian Dolomite rock properties and testing results	37
Table 5-1 Mancos Shale sample ID, rock properties and testing results.	66
Table 5-2 Intact Mancos Shale dynamic and static Young’s moduli E and Poisson’s ratios ν during deviatoric loading under 0.69 MPa confining stress.	67
Table 5-3 Fractured Mancos Shale sample dynamic and static Young’s moduli E and Poisson’s ratios ν during deviatoric loading under 0.69 MPa confining stress	67
Table 5-4 Intact Mancos Shale sample dynamic and static Young’s moduli E and Poisson’s ratios ν during deviatoric loading under 3.45 MPa confining stress.	68
Table 5-5 Intact Mancos Shale sample dynamic and static Young’s moduli E and Poisson’s ratios ν during deviatoric loading under 6.9 MPa confining stress.....	68
Table 6-1 Third-order nonlinear stiffness coefficients C_{111} , C_{333} , C_{112} , C_{133} , C_{144} , C_{255} , and C_{366} for the isotropic and deviatoric stress loading of Mancos Shale	77
Table 6-2 Ratios of static-to-dynamic E_h , E_v , ν_{12} , ν_{13} , and ν_{31} during deviatoric loading, and K during isotropic loading	78
Table 6-3 Mancos Shale results from tests at several confining stresses used to determine shear failure envelopes for oriented plugs.....	93
Table 6-4 Isotropic stresses for the three Mancos plug orientations and the corresponding stiffness coefficients C_{ij} , and dynamic and static bulk moduli, K_{Dyn} and K_{St}	94
Table 6-5 The P - and S -wave velocities measured during isotropic loading.....	95
Table 6-6 Static strains for the three Mancos plug orientations during isotropic loading	96
Table 6-7 The deviatoric stresses for the three Mancos plug orientations and the corresponding stiffness coefficients C_{ij}	97
Table 6-8 The P - and S -wave velocities measured at each % of peak stress during deviatoric loading for the three orientations of Mancos plugs	98
Table 6-9 Static strains for the three Mancos plug orientations during deviatoric loading	99
Table 6-10 Mancos dynamic and static Young’s moduli E and Poisson’s ratios ν during deviatoric loading.....	100
Table 7-1 Experimental measurements of P - and S -wave velocities on unconfined oriented Mancos cores, and the calculated the Thomsen anisotropy parameters ϵ , γ , and δ	105

Table 7-2 Major minerals present in Mancos Shale and their respective mass density (ρ), bulk (K) and shear (μ) moduli..... 110

Table 7-3 *P*- and *S*-wave velocities, volume average densities ($\langle\rho\rangle$), and velocity anisotropies from experimental measurements and simulation results..... 117

List of Figures

Figure 2-1 Core and microscope images of Berea Sandstone and Silurian Dolomite	10
Figure 2-2 Mancos Shale samples with bedding and measurement orientations indicated.	12
Figure 2-3 Schematic of triaxial load frame.	14
Figure 2-4 Mancos Shale stress loading paths.	16
Figure 4-1 Example of Berea Sandstone deviatoric loading experiment and definition of SWX and PPD	34
Figure 4-2 Comparison of static and dynamic results from Berea Sandstone and Silurian Dolomite subjected to deviatoric loading to failure at confining stresses of 10.3 MPa	36
Figure 4-3 Effective axial stress at SWX, PPD, and Peak as a function of radial confining stress for Berea Sandstone and Silurian Dolomite.....	38
Figure 4-4 Relationship between the effective axial stress at peak strength and effective axial stress at PPD and SWX for Berea Sandstone and Silurian Dolomite.....	40
Figure 4-5 Shear-wave anisotropy as a function of the fraction of peak stress at which they occur for Berea Sandstone and Silurian Dolomite.....	41
Figure 4-6 Comparison of static axial stiffness $\Delta\sigma_1/\Delta\varepsilon_1$ and ratio of radial expansion to axial shortening $-\varepsilon_3/\varepsilon_1$ as a function of the fraction of peak stress at which they were measured, and the corresponding dynamic-to-static transforms of Young’s modulus for Berea Sandstone Silurian Dolomite.....	44
Figure 4-7 X-ray CT images of Berea Sandstone and Silurian Dolomite with shear wave measurement axes compared to fracture orientations.	47
Figure 5-1 Dynamic-static transforms for Young’s moduli E_v and E_h of Mancos Shale samples at different confining stresses	55
Figure 5-2 Dynamic-static transforms for Poisson’s ratios ν_{12} , ν_{13} , and ν_{31} of Mancos Shale samples at different confining stresses	56
Figure 5-3 Dynamic-static transforms for Young’s moduli E_v and E_h for fractured and intact Mancos Shale samples both tested at 0.69 MPa confining stress.	58
Figure 5-4 Dynamic-static transforms for Poisson’s ratios ν_{12} , ν_{13} , and ν_{31} for fractured and intact Mancos Shale samples both tested at 0.69 MPa confining stress..	59
Figure 5-5 Pre- and post- testing X-ray CT images highlighting initially intact microstructure and stress-induced fractures in plugs parallel and at 45° to bedding.....	61

Figure 5-6 Pre- and post- testing X-ray CT images highlighting pre-existing fractures and their interaction with stress-induced fractures in plugs taken parallel, perpendicular and at 45° to bedding.....	63
Figure 6-1 Stress-strain curves of oriented Mancos Shale samples during isotropic loading and unloading, and deviatoric loading to failure.	74
Figure 6-2 Mancos Shale dynamic stiffness coefficients C_{11} , C_{33} , C_{55} , C_{66} , C_{12} , and C_{13} as a function of mean stress during isotropic loading.....	76
Figure 6-3 Measured and modeled dynamic and static bulk moduli as a function of mean stress during isotropic loading.	79
Figure 6-4 Mancos Shale dynamic stiffness coefficients C_{11} , C_{33} , C_{55} , C_{66} , C_{12} , and C_{13} as a function of % of peak stress during deviatoric loading.	80
Figure 6-5 Measured and modeled anisotropic dynamic and static Young’s Moduli E_h and E_v as a function of % of peak stress during deviatoric loading.....	83
Figure 6-6 Measured and modeled anisotropic dynamic and static Poisson’s ratios ν_{12} , ν_{13} , and ν_{31} as a function of % of peak stress during deviatoric loading.....	83
Figure 6-7 X-ray CT images of oriented Mancos Shale samples after failure.	87
Figure 6-8 Mancos static and dynamic bulk moduli during isotropic loading and unloading.....	92
Figure 6-9 Tangent static and dynamic Young’s moduli E_h and E_v during deviatoric loading ...	93
Figure 7-1 Experimentally determined Thomsen anisotropy parameters for Mancos Shale.....	107
Figure 7-2 Evidence of layering, fractures, and rock fabric in the same Mancos Shale sample at different scales	109
Figure 7-3 Workflow for determining mineralogy from SEM-derived BSE and elemental maps	113
Figure 7-4 Workflow for creating velocity models from X-ray CT scans.....	115
Figure 7-5 Example of the Synthetic V_p model showing wave propagation model setup and output waveforms.....	119
Figure 7-6 P-wave velocity models Core_0° and Core_90°, derived from 40 μm resolution CT scan of Mancos Shale cores	122
Figure 7-7 P-wave velocity models 13 μm _All, 13 μm _Layer, and 13 μm _Frac derived from 13 μm resolution CT scan of Mancos Shale core	124
Figure 7-8 SEM mineralogy maps and P -wave velocity models SEM_Layer and SEM_Frac derived from 0.9 μm resolution SEM scanline	127

Figure 7-9 Comparison between the *P*- and *S*-wave velocities from experimental and modeled results. 128

Figure 7-10 Comparison between the % of *P*-wave and *S*-wave anisotropy from the various models normalized to the experimental measurements**Error! Bookmark not defined.**

Figure 7-11 Measured and modeled *P*- and *S*-wave anisotropy and impedance. 136

List of Symbols

C_{ij}	Second-order stiffness coefficients
C_{ijk}	Third-order stiffness coefficients
ε_{ij}	Directional strain
$\varepsilon_a, \varepsilon_r,$ and ε_v	Axial, radial, and volumetric strain
E_v and E_h	Vertical and horizontal Young's moduli
E_5 and E_{95}	Young's moduli at 5% and 95% of peak deviatoric stress
K	Bulk modulus
σ_1, σ_3	Maximum and minimum principal stresses
σ_{ij}	Directional stress
σ_D	Deviatoric stress ($\sigma_1 - \sigma_3$)
σ_{DPeak}	Peak deviatoric stress
σ_m	Mean Stress
ν_{ij}	Poisson's ratios ($ij=12, 13,$ or 31)
V_p	P-wave velocity
V_{sx} and V_{sy}	Directional shear-wave velocity

1. Introduction

The upper brittle 10 km of the Earth's crust provide critical resources to society. Efficient energy extraction, wastewater disposal or storage, and other activities depend on rock permeability and strength. Frequently, these attributes depend on naturally occurring fractures or on fractures created in engineering operations. In the past decade, the need to understand both types of fracture in the fine-grained sedimentary rock known as *shale* has become urgent, as an increasing proportion of hydrocarbon resources are being produced from these rocks. Chapter 1 discusses the motivation for conducting the dissertation research. Specific motivations include the necessity for enhanced methods to quantify natural fracturing and rock damage, and the often ignored complexities in rock mechanical behavior such as elastic anisotropy and nonlinearity when estimating in-situ rock properties. Previous studies pertaining to fracture and damage characterization, as well as rock nonlinearity and anisotropy, are presented in order to demonstrate current limitations and potential implications for overcoming knowledge and technological gaps.

1.1 MOTIVATION

Unconventional shale reservoirs host vast amounts of hydrocarbons and have become increasingly important to global oil markets. In 2017, shale and other tight reservoirs were estimated to account for roughly 65% and 72% of produced oil and natural gas in the US, respectively (EIA 2018). Despite their immense hydrocarbon storage and production capacity, shale matrix porosity is low and permeabilities typically fall in the nano- to micro-darcy range, making production from these tight reservoirs economically

unfeasible without recent technological advances in horizontal drilling and hydraulic fracturing (Zoback 2007). Advanced drilling and completions techniques are further complicated by subsurface heterogeneity such as the presence of pre-existing fractures (Gale et al., 2014) and lithological variations, which can both cause anisotropic mechanical properties and impact the rock stress-strain response (Warpinski 1991, Wang 2002, Laubach et al. 2009, Mokhtari et al. 2014). Pre-existing fractures and stratigraphic variations in mechanical properties are known to influence the growth of engineered fractures (Warpinski and Teufel 1987, Gale et al., 2007, Bodziak et al. 2014, Lee et al. 2015). For example, rock laminations and aligned heterogeneities can be beneficial, acting as planes of weakness, which may facilitate the branching of hydraulic fractures and increase stimulated reservoir volume (Fisher et al. 2002). Conversely, these tabular features may give rise to mechanical stratigraphy, which can limit the growth of hydraulic fractures, as well as increase the risk of borehole stability related issues such as hole collapse and lost circulation (Horsrud 2001, Mokhtari et al. 2014). Drilling issues associated with mechanical uncertainty typically account for 10-15% of total well cost (Mody et al. 2007).

The potential role fractures and heterogeneities might play as preferential planes of weakness or conduits for flow depends on several factors, including their size, orientation, and the degree to which they may be filled by natural cements during diagenesis (Gale et al. 2014). Therefore, a more detailed characterization of pre-existing fractures and layering, and evaluation of their impacts on rock mechanical properties can reduce the uncertainty associated with implementing advanced drilling and completion techniques and increase the profitability of producing from unconventional reservoirs (Suarez-Rivera et al. 2005).

Indirect multi-scale measures of rock mechanical properties yield insights into the attributes of pre-existing fractures and layering but are inadequate for completely describing rock behavior. Coupling these indirect methods with more direct measurements offers avenues for decreasing mechanical uncertainty, thus increasing the financial feasibility of drilling and hydraulic stimulation in shale formations. Mechanical properties are measured at several scales, including: static and ultrasonic measurements on centimeter-sized plugs, acoustic well-logging of the near wellbore region, and surface seismic surveying at significantly larger scales (Vernik and Nur 1992, Eberhardt et al. 1998, De Almeida et al. 2008). Each measurement bears important information about subsurface mechanical properties. However, upscaling between core and seismic scales is commonly limited by velocity dispersion and attenuation, where wave velocities depend on measurement resolution (wavelength) with respect to the scale of internal rock heterogeneity; they also can be impacted by the presence of fluids within the rock (Marion 1994, Gurevich et al. 2009, Holt et al. 2012,). Furthermore, anisotropy measured at multiple scales may be manifestations of different lithological characteristics. For example seismic scale anisotropy may be attributed to impedance contrasts between formations, whereas core scale anisotropy could be most heavily impacted by variations in clay content between mm-scale layers. Additional challenges arise in attempting to relate purely elastic dynamic measurements (ultrasonic, borehole sonic, seismic) to static measurements (core scale stress-strain testing). The latter likely more closely represents the rock behavior in response to large strains imposed during drilling and hydraulic fracturing (Zoback 2007).

Although static measurements more accurately represent subsurface rock behavior, they typically can only be reliably obtained in the laboratory, and they vary considerably from dynamically measured rock properties at the same scale due to dispersion, attenuation, and plasticity. For example, small magnitude elastic strains ($\epsilon \approx 10^{-7}$) are imparted at a high strain rate through dynamic testing and frequently yield several times higher dynamic moduli than static measurements requiring higher strain magnitudes ($\epsilon \approx 10^{-2}$ - 10^{-3}) at lower strain rates and often exhibit plastic strains and creep (Ciccotti and Mulargia 2004, Mavko et al. 2009, Frydman et al. 2016, Ramos et al. 2017). Because wellbore sonic tools do not provide a direct measurement of rock strength, static elastic properties, or in-situ stresses, we currently rely on potentially unreliable correlations and interpretations (Holt et al. 1989, Donald et al. 2013; 2015, Donald and Prioul 2015, Jin et al. 2016). Simultaneous dynamic and static measurements in the laboratory can shed light on this strain-rate magnitude dependence, and they are required for the development of more accurate dynamic-static transforms $(E_{ST}, \nu_{ST}) = f(E_{DYN}, \nu_{DYN})$, which can be applied to dynamic measurements (such as acoustic well logs) to estimate the in-situ static moduli and stress-strain behavior (Amadei 1996, Yale et al. 1994, Fjaer 1999).

Dynamic-static transforms have been attempted for several shales (Lacy 1997, Fjaer and Nes 2013, Sone and Zoback 2013, Jin et al. 2016, Mikhaltsevitch et al. 2016). For example, previous studies of Mancos Shale show dynamic Young's moduli being more than double those measured statically (Holt et al. 2013). However, because rocks exhibit elastic nonlinearity, it is important to understand how dynamic and static rock properties evolve with changing stress and with stress-induced damage. Studying the stress

dependencies of dynamic and static measurements would also help constrain the various sources of elastic anisotropy. Rock elastic anisotropy can be caused by intrinsic lithological features such as clays, layering, and the presence of compliant grain contacts and fractures. Anisotropy can also be induced when rocks are subjected to anisotropic stresses, which may close preferentially oriented compliant features or impart microstructural changes such as strain localization and damage (Vernik 1993, Sayers and Kachanov 1995, Ayling et al. 1995, Jaeger et al. 2009, Mokhtari et al. 2013, Ramos et al. 2017). The stress dependencies of anisotropic elastic moduli are typically only evaluated during isotropic stress loading, where measurements are made on samples subjected to the same stress states and magnitudes. However, subsurface stress changes (tectonic and human-induced) are rarely isotropic, and rock mechanical properties can vary significantly depending on the stress loading path (Lo et al. 1986, Eberhart-Phillips et al. 1989, Schwartz et al. 1994, Scott and Abousleiman 2005). Therefore, evaluating the deviatoric stress dependences of the anisotropic stiffness terms can provide insight into the rock deformational behavior under more realistic stress conditions. To the best of my knowledge, no attempts have been made to develop dynamic-static transforms that account for stiffness anisotropy and nonlinearity, the effects of pre-existing fractures, or the impact of stress-induced damage during deviatoric loading to failure (Liming and Fjaer 2012, Holt et al. 2012, Holt et al. 2013). Considering these variables when developing dynamic-static transforms is necessary for accurately estimating in-situ rock mechanical properties, horizontal stresses, and rock mechanical behavior in response to stress changes during the life of a well (i.e. drilling, completions, depletion) (Prioul et al. 2011).

1.2 OBJECTIVES AND DISSERTATION OUTLINE

The objective of this study is to quantify the impacts of fractures and layering on shale mechanical properties by investigating quasi-static strain measurements and ultrasonic *P*- and *S*- wave propagation under various stress loading paths. This work builds and expands on previous studies, but for the first time addresses the development of dynamic-static transforms that account for anisotropic and nonlinear rock mechanical properties during deviatoric stress loading, and the impacts of pre-existing fractures and those caused by man-made stress changes (hereafter, *stress-induced fractures*) on rock mechanical properties. I also develop techniques for quantifying dynamic rock properties from SEM and CT-scale measurements and decoupling the effects of various lithological micro-structures such as layering and fractures on measured velocity anisotropy. Taking these variables into consideration when developing dynamic-static transforms allows analysts to reduce the uncertainty associated with estimating in-situ stresses and mechanical properties at the wellbore scale.

The Dissertation is divided into eight chapters. This Introduction (Chapter 1) contextualizes the importance of accurately measuring rock mechanical properties of unconventional oil and gas reservoirs, and presents the limitations of previous work, as well as the author's objectives for addressing those limitations.

Chapter 2 details laboratory methods utilized to conduct the doctoral research, including descriptions of the tested rock samples, the triaxial frame setup, ultrasonic velocity measurement system and data acquisition, X-ray Micro-Computed Tomography (CT) imaging, and Scanning Electron Microscopy (SEM) analyses.

Chapter 3 is an account of the theoretical background of the work, including equations for: calculating the linear and nonlinear elastic stiffness coefficients for rocks with vertical transverse isotropy (VTI), calculating the static and dynamic Bulk modulus, Young's moduli, and Poisson's ratios for isotropic and VTI rocks, and calculating Thomsen's (1986) anisotropy parameters.

Chapters 4 through 7 are based on previously published or submitted manuscripts authored by Matthew John Ramos. Co-authors who provided mentoring, guidance, writing feedback and edits, technical expertise, and assisted in data analysis for the paper are listed at the beginning of each chapter.

Chapter 4 is titled "The Use of Shear-Wave Anisotropy to Quantify the Onset of Stress-Induced Microfracturing" and is a peer-reviewed journal paper published in *Geophysics*. The chapter focuses on static and dynamic measurements in relatively isotropic rocks (Berea Sandstone and Silurian Dolomite), and results and analyses detail the utility of a novel approach using dynamic shear-wave measurements to detect damage during triaxial stress testing.

Chapter 5 is titled "Stress-Dependent Dynamic-Static Transforms of Anisotropic Mancos Shale" and is a conference published by the American Rock Mechanics Association, presented at their 2017 Symposium in San Francisco, CA and accessible through SPE's portal OnePetro. Chapter 5 presents experimental work relating to static and dynamic stiffness anisotropy in intact and fractured rocks. Two case studies are presented to highlight the impacts of (1) confining stress, and (2) fractures on the anisotropic dynamic-static transforms.

Chapter 6 is titled “Quantifying Static and Dynamic Stiffness Anisotropy and Nonlinearity in Finely Laminated Shales: Experimental Measurement and Modeling” and is a submitted manuscript to the journal Geophysics and has undergone the first round of reviews. Chapter 6 presents experimentally measured static and dynamic mechanical properties of a set of Mancos Shale core plugs subjected to isotropic and deviatoric loading. We utilize nonlinear elastic theory to model the stress-dependent behavior of these rocks and develop dynamic-static transforms which take into account both the anisotropic and nonlinear behavior.

Chapter 7 is titled “Microstructural Controls on Elastic Anisotropy of Finely Laminated Mancos Shale” and represents a soon to be submitted journal paper. Chapter 7 presents modeling results at several scales, which utilize SEM and CT imaging to investigate the various microstructural controls on ultrasonic velocity anisotropy measured in the laboratory.

Chapter 8 connects the major findings of each chapter and provides overarching conclusions of the doctoral research.

2. Experimental Methods

2.1 ROCK TYPES

The rock samples tested for this study are Berea Sandstone, Silurian Dolomite, and Mancos Shale. Tests on relatively isotropic non-shale lithologies are useful for validating experimental methods and gaining insight into complex processes in less variable materials, which could then be extended to anisotropic rocks. Therefore, Berea Sandstone and Silurian Dolomite were chosen to provide a broad range of rock fabric. Berea samples come from the Upper Devonian Berea Formation, a relatively fine-grained and well-sorted sandstone, which appears relatively homogeneous at laboratory scales. Berea samples were taken from two blocks, each exhibiting fairly uniform sample porosities: block 1 = $21\% \pm 0.5\%$, and block 2 = $24.3\% \pm 0.3\%$ (Table 4-1). Silurian carbonate rock samples from the Thornton Formation on the other hand, exhibit significant variability in terms of pore geometries and spatial distribution; they had an average porosity of $15.2\% \pm 5.2\%$, ranging between 10% and 18.3% (Table 4-1). Mineral dissolution and precipitation during the dolomitization of Silurian reefs likely played an appreciable role in reshaping pore networks, causing the large range of sample porosities.

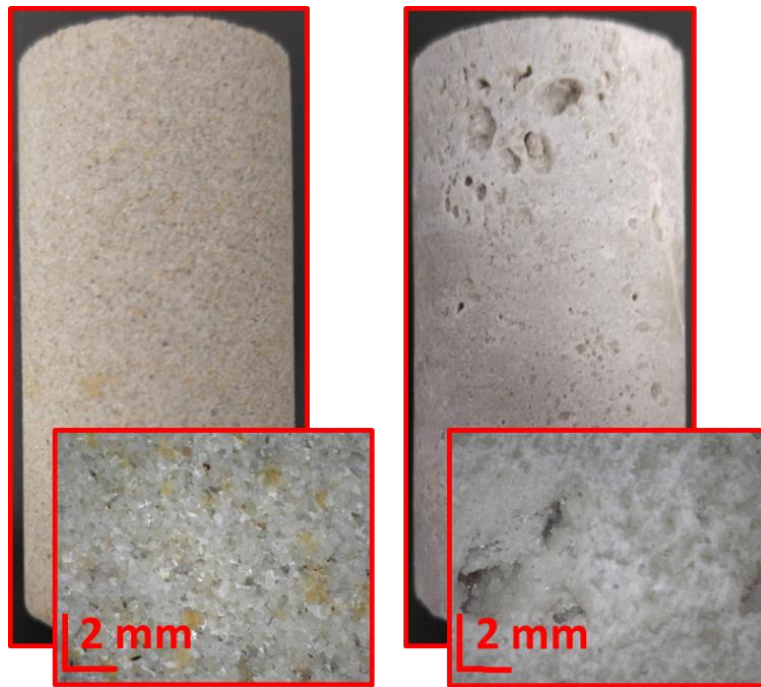


Figure 2-1 Core and microscope images of the tested rock types. Berea Sandstone (left) and Silurian Dolomite (right). Cores are 50 mm length by 25 mm diameter.

Cretaceous Mancos Shale was chosen based on the availability of core plugs, as well as its pertinence to hydrocarbon exploration. Mancos Shale is a known source rock and gas producing interval within the Uinta Basin, which stretches from eastern Utah into Colorado and Wyoming. Mancos Shale represents the transition between shallow marine sandstones in Utah into chalks and marls in the east. Stratigraphic and sedimentological work indicate that our tested Mancos samples likely derive from depositional environments similar to a mudbelt or sediment starved shelf (Birgenheier et al. 2017). Our SEM-derived mineralogical compositions and the visible scouring/cross bedding are consistent with previous descriptions of these depositional settings. Mancos samples exhibit two major facies in their layering (Figure 2-2-A). Scanning electron microscope (SEM) Back-scattered Electron Detection (BSE) and Energy Dispersive X-ray Spectroscopy (EDS)

measurements show that both facies contain the same major mineral constituents but in different quantities. The light facies consists of roughly 52% quartz, 13% clays, 16% calcite, and 11.4% dolomite, whereas the dark facies is comprised of roughly 15% quartz, 46% clays, 5% calcite, and 19% dolomite. Minor minerals make up the remainder of each facies. These represent endmember compositions for the two facies, whereas mixing of the two is commonly seen.

Despite their hydrocarbon potential, our tested shale samples were commercially quarried, and core plugs were taken at various orientations with respect to bedding (0°, 45°, and 90°) (Figure 2-2-B). A 60 µm thin section was prepared from a 90° sample (perpendicular to bedding), which allowed for Scanning Electron Microscopic (SEM) imaging and analysis of the distinctly light and dark colored layers within Mancos samples. An additional 25 mm diameter x 6.25 mm thick slice was cut from the rock adjacent to the thin section location for comparison with X-ray CT results. Although Mancos samples on average are oriented 0°, 45°, and 90° with respect to bedding, individual layers deviate from these orientations due to the considerable heterogeneity and cross-bedding within our samples. Purchasing quarried samples allowed for many tests under varying conditions and the most robust characterization. Mancos Shale sample mass densities and testing results are shown in Table 5-1. All tested samples were cut to approximately 2:1 length to diameter ratio (50 mm x 25 mm) and endface-ground to ensure parallelism. Tests were conducted on air-dry samples, so pore pressure was assumed to be negligible.

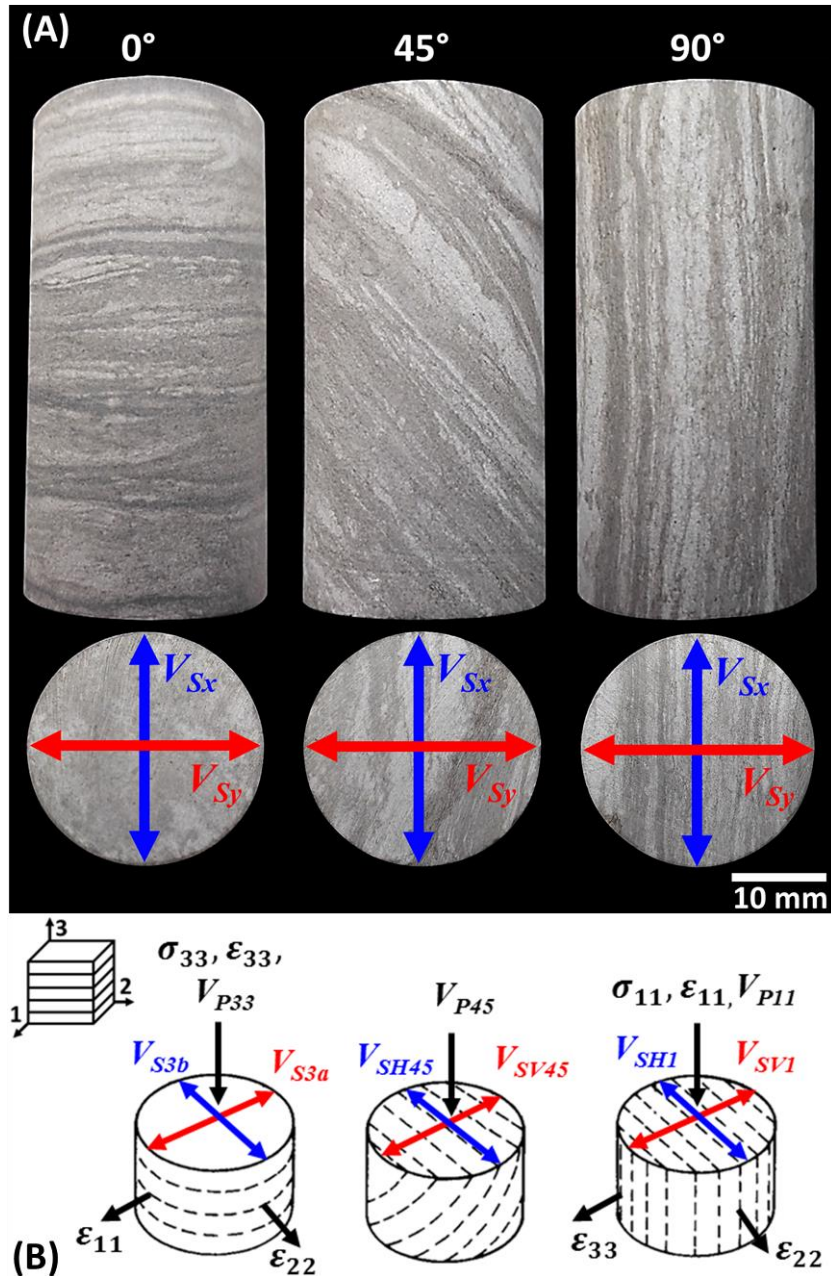


Figure 2-2 Mancos core samples with bedding at 0° (left), 45° (middle), and 90° (right) (A). Top view of cores show relative orientations of S_x (blue) and S_y (red) shear wave components during testing. Cores are approximately 50 mm length x 25 mm diameter. (B) The stress, strain and velocity measurement orientations on cores taken perpendicular (left), parallel (middle), and at 45° (right) to bedding. Measurement orientations for static properties and P -wave velocities are shown in black font, and S -wave velocity measurements are in colored font, where the arrows point to the direction of particle motion for waves propagating axially through the sample.

2.2 TRIAXIAL LOAD FRAME, ULTRASONIC MONITORING

Simultaneous triaxial testing and ultrasonic measurements were conducted using a triaxial frame capable of applying up to 225,000 kg axial loads and total radial stresses up to 138 MPa (manufactured by TerraTek). High stiffness of the load frame provides strain-control close to and after failure in strain-softening materials. Samples were loaded axially between two endcaps, each equipped with three piezoelectric transducers for measuring propagation of compressional P -waves and polarized shear S -waves at 90° , S_x and S_y every 30 seconds throughout testing (Figure 2-3). P -wave and S -wave propagation was observed at a central frequency of 1 MHz with a frequency bandwidth of 0.2 - 1.4 MHz in air-dry samples. First arrivals were picked using a multi-window time averaging algorithm, which detects amplitude spikes above a predetermined threshold. Wave velocities were calculated from arrival times after being corrected for endcap travel, determined from calibration using aluminum samples. We estimate a maximum of 5% error in our stiffness calculations, most likely associated with the picking of first arrivals. However, because the same picking methods are used for all arrivals, we believe the error is likely consistent for all times picked. Local strains were calculated from axial and radial displacements measured through sets of sample-mounted cantilever arms. Axial displacements are an average from four independent arms, and total radial displacements are an average from two perpendicularly measured radial displacements each measured with two independent arms. Strain gauges have a precision of roughly $\pm 0.5 \cdot 10^{-7}$ and were calibrated previously with a Mitutoyo sub-micron micrometer. Ultrasonic and displacement sensors were manufactured by TerraTek. Measurement orientations can be described by a Cartesian coordinate system.

However, because stresses and strains are measured in the principal directions and the confining stress is radially symmetric ($\sigma_x = \sigma_y$), the relative orientations of stresses and strains are denoted in the axial (σ_1, ϵ_1) or radial (σ_3, ϵ_3) directions (Figure 2-1). Therefore, we refer to σ_1 and σ_3 , respectively, as the maximum and minimum (compressive) principal stresses, different from σ_{11} and σ_{33} , the normal stress perpendicular to faces 1 and 3 (Figure 2-2). Recommendations for best practices regarding sample preparation and laboratory measurements are provided in Appendix A.

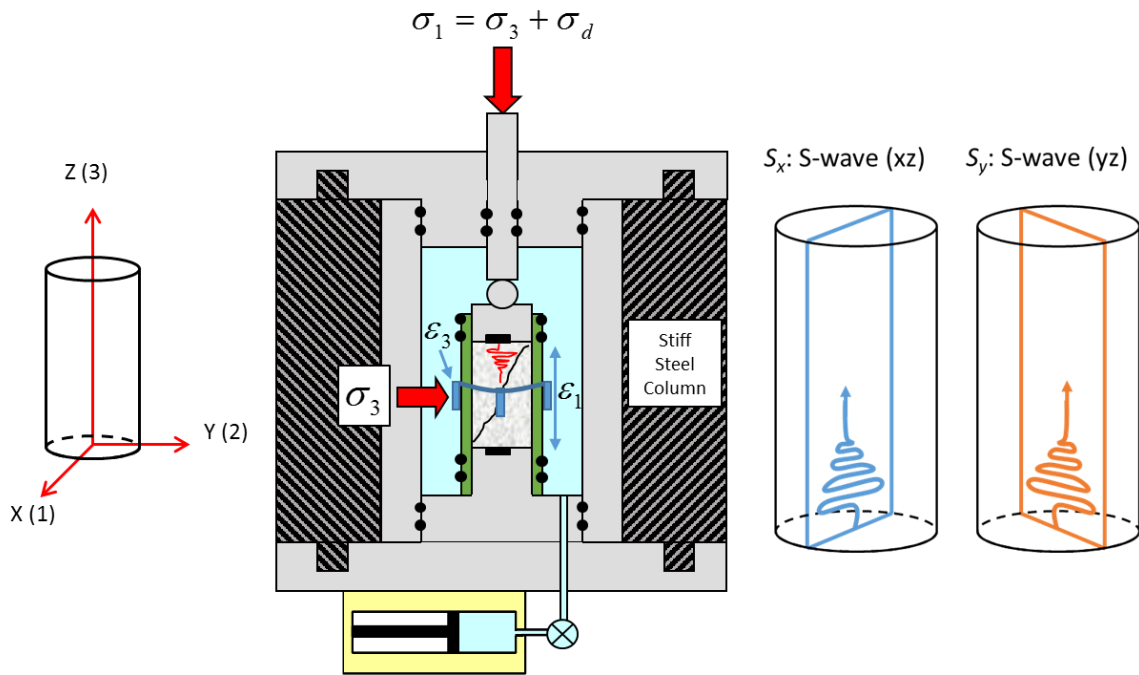


Figure 2-3 Cartesian coordinate system and associated principle directions (left), schematic of triaxial cell (middle left), and the relative orientations of the perpendicular shear-wave components S_x (middle right) and S_y (right).

2.3 STRESS PATHS AND TESTING CONDITIONS

All samples were subjected to a constant radial confining stress $\sigma_2 = \sigma_3$, and subsequently loaded axially (axial stress σ_1) at an axial strain rate of $\dot{\epsilon}_1 = 4 \times 10^{-6} \text{ s}^{-1}$ until

failure. We use the term deviatoric stress to represent the difference between the axial and radial stresses ($\sigma_D = \sigma_1 - \sigma_3$). Tests were performed at various radial stresses in order to evaluate the impact of confining stress on damage evolution and dilatancy in Berea and Silurian samples (Chapter 4), as well as static and dynamic stiffness anisotropy and nonlinearity in Mancos samples (Chapters 5 and 6). The confining stresses used were (0.69 MPa, 3.45 MPa, 6.9 MPa, 10.3 MPa, 13.8 MPa, and 20.8 MPa) for Chapter 4, (0.69 MPa, 3.45 MPa, 6.9 MPa) for Chapter 5, and 20.7 MPa for Chapter 6. However, prior to deviatoric loading, samples in Chapter 6 were first subjected to isotropic stress loading up to 82.7 MPa at a loading rate of 69 kPa/s, then subsequently unloaded at the same rate to 20.7 MPa. Figure 2-4 shows the mean-deviatoric stress path for tested samples in Chapter 6 and the experimentally determined shear-failure lines for the three core orientations analyzed for all intact (not fractured), Mancos samples in Chapters 5 and 6.

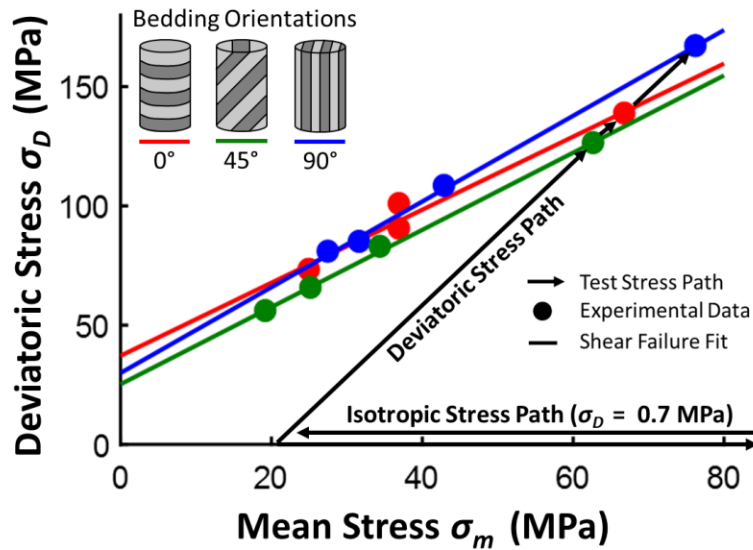


Figure 2-4 Sample stress loading path in a mean stress-deviatoric stress plot. Example of samples from Chapter 6, which underwent isotropic loading to 82.7 MPa, then unloading to 20.7 MPa. After the isotropic cycle, samples were loaded deviatorically until shear failure. Colored lines represent the shear failure lines for 0° (red), 45° (green), and 90° (blue) samples, determined from experimentally measured peak stresses of oriented samples at various confining stresses (colored circles). Samples from Chapters 3 and 4 were only loaded isotropically to the final confining stress used for deviatoric loading.

2.4 X-RAY MICRO-COMPUTED TOMOGRAPHY

X-ray micro-computed tomography (CT) imaging was performed with a Nikon XTH-225 scanner (225kV micro-focus X-ray source with 3 μ m focal spot size). Mancos samples were scanned both prior to and post testing. Pre-test imaging provides both a quality check to identify any defects or pre-existing fractures, as well as a means for documenting the rock microstructure before stress-induced failure. Post-testing imaging was used to evaluate stress-induced fracture development in terms of orientation and potential interaction with bedding planes and pre-existing fractures. Because the rock changes significantly during testing, 1:1 superposition of pre- and post-test images is

difficult. However, samples were marked in order to ensure the pre- and post-test imaging was performed at the same orientation, which allowed us to evaluate the potential impact of bedding planes, pre-existing fractures, and aligned heterogeneities on the orientation, turning, branching, and containment of stress-induced fractures during testing (Shen et al. 1995, Germanovich and Astakhov 2004, Suarez-Rivera et al. 2013, Ramos et al. 2017). Due to the relative timing of sample testing and acquisition of our CT setup, only post-test imaging was performed on Berea and Silurian samples.

2.5 SCANNING ELECTRON MICROSCOPY

A Zeiss Sigma Field Emission SEM with Back-scattered Electron detection (BSE) and Energy Dispersive X-ray Spectroscopy (EDS) was used to image and map the elemental composition within the thin section. The BSE and EDS analyses were performed at 10 kV and a 120 μm aperture was used for EDS mapping. Images were acquired using a 50 μs dwell time for BSE and 2 minutes for EDS. Simultaneous BSE and EDS scanlines were collected through the center of the thin section. Scanlines were roughly 0.87 mm wide and spanned the entire 25 mm length in the direction perpendicular to bedding.

3. Theoretical Background

3.1 CALCULATION OF STATIC AND DYNAMIC MECHANICAL PROPERTIES

Because tested samples span a wide range of lithologies, their relative degrees of anisotropy also vary considerably. For this study, Berea and Silurian samples are deemed isotropic, whereas the Mancos Shales exhibit distinct layering and are thus considered to have vertical transverse isotropy (VTI) (Sarker et al. 2010). With our experimental setup, the three independent elastic parameters required to characterize isotropic rocks were calculated from velocities measured on a single plug (Timoshenko and Goodier 1934):

$$G = V_s^2 \rho , \quad (1)$$

$$\nu = \frac{V_p^2 - 2V_s^2}{2(V_p^2 - V_s^2)} , \text{ and} \quad (2)$$

$$E = 2G(1 + \nu) , \quad (3)$$

where G is the shear modulus, ν is the Poisson's ratio, E is the Young's modulus, ρ is the bulk density, and V_p and V_s are, respectively, the compressional and shear wave velocities.

Mancos shale and other VTI rocks assume rotational symmetry about the 3 axis and can be described by 5 independent elastic stiffness parameters (Figure 2-3). The elastic stiffness tensor for VTI rocks relates the stress tensor $\underline{\sigma}$ and the strain tensor $\underline{\epsilon}$ through a set of second order stiffness coefficients c_{ij}^0 (at the reference stress state - Voigt notation):

$$\begin{pmatrix} \sigma_{11} \\ \sigma_{22} \\ \sigma_{33} \\ \tau_{23} \\ \tau_{13} \\ \tau_{12} \end{pmatrix} = \begin{pmatrix} c_{11}^0 & c_{12}^0 & c_{13}^0 & 0 & 0 & 0 \\ c_{12}^0 & c_{11}^0 & c_{13}^0 & 0 & 0 & 0 \\ c_{13}^0 & c_{13}^0 & c_{33}^0 & 0 & 0 & 0 \\ 0 & 0 & 0 & c_{44}^0 & 0 & 0 \\ 0 & 0 & 0 & 0 & c_{55}^0 & 0 \\ 0 & 0 & 0 & 0 & 0 & c_{66}^0 \end{pmatrix} \begin{pmatrix} \varepsilon_{11} \\ \varepsilon_{22} \\ \varepsilon_{33} \\ 2\varepsilon_{23} \\ 2\varepsilon_{13} \\ 2\varepsilon_{12} \end{pmatrix}, \quad (4)$$

This relationship describes rock stiffness at a reference stress and strain. However, in order to model changes in stiffness with applied stress or strain, elastic nonlinearity must be considered (Sinha and Kostek, 1996, Prioul et al. 2004). Approximations for describing nonlinear elasticity can be used to modify the stress-strain relationship by incorporating third-order stiffness coefficients c_{ijk} to relate the new and reference stress states (Sayers and Allen 1984, Sayers 2010):

$$c_{11} \approx c_{11}^0(1 + 3\varepsilon_{11} - \varepsilon_{22} - \varepsilon_{33}) + (c_{111}\varepsilon_{11} + c_{112}\varepsilon_{22} + c_{113}\varepsilon_{33}), \quad (5)$$

$$c_{33} \approx c_{33}^0(1 - \varepsilon_{11} - \varepsilon_{22} + 3\varepsilon_{33}) + (c_{133}\varepsilon_{11} + c_{233}\varepsilon_{22} + c_{333}\varepsilon_{33}), \quad (6)$$

$$c_{44} \approx c_{44}^0(1 - \varepsilon_{11} + \varepsilon_{22} + \varepsilon_{33}) + (c_{144}\varepsilon_{11} + c_{244}\varepsilon_{22} + c_{344}\varepsilon_{33}), \quad (7)$$

$$c_{55} \approx c_{55}^0(1 + \varepsilon_{11} - \varepsilon_{22} + \varepsilon_{33}) + (c_{155}\varepsilon_{11} + c_{255}\varepsilon_{22} + c_{355}\varepsilon_{33}), \quad (8)$$

$$c_{66} \approx c_{66}^0(1 + \varepsilon_{11} + \varepsilon_{22} - \varepsilon_{33}) + (c_{166}\varepsilon_{11} + c_{266}\varepsilon_{22} + c_{366}\varepsilon_{33}), \quad (9)$$

$$c_{12} \approx c_{12}^0(1 + \varepsilon_{11} + \varepsilon_{22} - \varepsilon_{33}) + (c_{112}\varepsilon_{11} + c_{122}\varepsilon_{22} + c_{123}\varepsilon_{33}) \quad (10)$$

$$c_{13} \approx c_{13}^0(1 + \varepsilon_{11} - \varepsilon_{22} + \varepsilon_{33}) + (c_{113}\varepsilon_{11} + c_{123}\varepsilon_{22} + c_{133}\varepsilon_{33}), \quad (11)$$

Where c_{ij} are the effective stiffness coefficients of a stressed media, which are related to the stiffness terms at the reference stress state c_{ij}^0 and the principal static strains incurred due to the applied stress. Sayers and Allen 1984 presented these (and additional) equations

assuming that the third-order stiffness tensor represented by Equations 5-11 is orthorhombic. However, our experimental setup is limited, and we can only fully describe the VTI stiffness tensor and measure static strains in the principal directions ε_{11} , ε_{22} , and ε_{33} . Therefore, we used a subset of the orthorhombic equations to represent the stress dependence of our VTI rocks using the third order stiffness terms $c_{111}, c_{333}, c_{112}, c_{113}, c_{122}, c_{133}, c_{233}, c_{144}, c_{244}, c_{344}, c_{155}, c_{255}, c_{355}, c_{166}, c_{266}, c_{366}$, and c_{123} . The independent third-order terms c_{ijk} can be estimated by fitting Equations 5-11 to experimentally derived VTI stiffness coefficients and static strains with changing stress (Sayers 2010). We calculated the VTI stiffness parameters from velocity measurements on plugs with bedding oriented at 0° , 45° , and 90° such that (Figure 2-2),

$$c_{11}(\underline{\underline{\sigma}}) = \rho V_{P11}^2, \quad (12)$$

$$c_{12}(\underline{\underline{\sigma}}) = C_{11} - 2\rho V_{SH11}^2, \quad (13)$$

$$c_{33}(\underline{\underline{\sigma}}) = \rho V_{P33}^2, \quad (14)$$

$$c_{44}(\underline{\underline{\sigma}}) = \rho V_{S3b}^2, \quad (15)$$

$$c_{55}(\underline{\underline{\sigma}}) = \rho V_{S3a}^2, \quad (16)$$

$$2c_{66}(\underline{\underline{\sigma}}) = c_{11} - c_{12}, \text{ and} \quad (17)$$

$$c_{13}(\underline{\underline{\sigma}}) = -\left(\frac{c_{44} + c_{55}}{2}\right) + \left(4\rho^2 V_{P45} - 2\rho V_{P45} (c_{11} + c_{33} + c_{44} + c_{55})\right)^{1/2} \left(c_{33} + \frac{c_{44} + c_{55}}{2}\right), \quad (18)$$

where ρ is the bulk density of the rock sample, and V 's are the P and S wave velocities in different directions as shown in Figure 2-2. For a VTI medium, $c_{44} = c_{55}$, however, in order to account for potential deviation from a true VTI medium, these values are calculated individually, and their average used to calculate c_{13} , and the Thomsen anisotropy parameters γ , and δ presented below.

The calculation of c_{13} is also complicated by the need to accurately measure V_{P45} , which is not only made difficult by the tendency for shales to fracture during the coring process, but also because anisotropic rocks exhibit different group and phase velocities when measured at an oblique direction with respect to bedding (Wang 2002, Mavko et al. 2009). The group velocity $V_P(\phi)$ is a function of the ray angle ϕ , and the phase velocity $V_P(\theta)$ is a function of the phase angle θ . Phase and group velocities can be calculated by (Byun 1984, Melaku 2007):

$$V(\theta) = V(\phi) \cos(\phi - \theta) \quad \text{for } \theta = 45^\circ \quad (19)$$

$$V(\phi) = \sqrt{\frac{V(90^\circ)^4 + V(0^\circ)^4}{V(90^\circ)^2 + V(0^\circ)^2}}, \quad \text{where } \phi = \tan^{-1}\left(\frac{V(90^\circ)}{V(0^\circ)}\right) \quad (20)$$

where $V(90^\circ)$ and $V(0^\circ)$ represent our velocity measurements on the 90° and 0° plugs V_{P11} , and V_{P33} , respectively. Therefore, in order to ensure the phase velocities were used to calculate c_{13} , ultrasonic measurements of V_{P45} were compared with the calculated phase velocity at a phase angle of $\theta = 45^\circ$. Because all V_{P45} measurements were within 2% of the calculated phase velocities (and within the margin of error for arrival picking), the measured velocities were used for calculation of stiffness parameters.

The calculated stiffness parameters are then used to calculate one dynamic bulk modulus, two dynamic Young's moduli, and three dynamic Poisson's ratios. To more easily represent these calculations, let D be the determinant of the stiffness matrix (Lo et al. 1986):

$$\underline{D} = \det \begin{bmatrix} c_{11} & c_{12} & c_{13} \\ c_{12} & c_{11} & c_{13} \\ c_{13} & c_{13} & c_{33} \end{bmatrix}, \quad (21)$$

then

$$E_{vDYN}(\underline{\sigma}) = \frac{\underline{D}}{c_{11}^2 - c_{12}^2}, \quad (22)$$

$$E_{hDYN}(\underline{\sigma}) = \frac{\underline{D}}{c_{11}c_{33} - c_{13}^2}, \quad (23)$$

$$\nu_{12DYN}(\underline{\sigma}) = \frac{c_{12}c_{33} - c_{13}^2}{c_{11}c_{33} - c_{13}^2}, \quad (24)$$

$$\nu_{13DYN}(\underline{\sigma}) = \frac{c_{13}(c_{11} - c_{12})}{c_{11}c_{33} - c_{13}^2}, \quad (25)$$

$$\nu_{31DYN}(\underline{\sigma}) = \frac{c_{13}}{c_{11} + c_{12}}, \quad (26)$$

and

$$K_{DYN}(\underline{\sigma}) = \frac{c_{33}(c_{11} + c_{12}) - 2c_{13}^2}{c_{11} + 2c_{33} + c_{12} - 4c_{13}}, \quad (27)$$

where K_{DYN} is the stress-dependent dynamic bulk modulus, E_{vDYN} and E_{hDYN} are the stress-dependent dynamic Young's moduli in the directions perpendicular and parallel to

bedding, respectively, whereas v_{12DYN} , v_{13DYN} , and v_{31DYN} are the stress-dependent dynamic Poisson's ratios.

In order to evaluate effective anisotropy and the evolution of sample anisotropy with increasing stress, Thomsen parameters are also calculated from stiffness parameters such that (Thomsen 1986):

$$\varepsilon(\underline{\underline{\sigma}}) = \frac{c_{11} - c_{33}}{2c_{33}}, \quad (28)$$

$$\gamma(\underline{\underline{\sigma}}) = \frac{c_{66} - \left(\frac{c_{44} + c_{55}}{2}\right)}{c_{44} + c_{55}}, \text{ and} \quad (29)$$

$$\delta(\underline{\underline{\sigma}}) = \frac{\left(c_{13} - \frac{c_{44} + c_{55}}{2}\right)^2 - \left(c_{33} - \frac{c_{44} + c_{55}}{2}\right)^2}{c_{33}(2c_{33} - c_{44} + c_{55})}. \quad (30)$$

where ε represents the P -wave velocity anisotropy, γ represents the shear wave velocity anisotropy, and δ represents the variation in velocity between measurements made at a finite offset and those at zero offset.

In addition to anisotropic dynamic moduli, one quasi-static bulk modulus is calculated during the isotropic cycle, while two Young's moduli and three Poisson's ratios are calculated during deviatoric loading. Static loading moduli are calculated as follows (assuming VTI):

$$K_{ST}(\underline{\underline{\sigma}}) = \frac{\Delta\sigma_{mean}}{\Delta\varepsilon_{vol}} \quad (31)$$

$$E_{vST}(\underline{\underline{\sigma}}) = \left. \frac{\Delta\sigma_{33}}{\Delta\varepsilon_{33}} \right|_{\sigma_{11}, \sigma_{22}}, \quad (32)$$

$$E_{hST}(\underline{\underline{\sigma}}) = \left. \frac{\Delta\sigma_{11}}{\Delta\varepsilon_{11}} \right|_{\sigma_{22}, \sigma_{33}} = \left. \frac{\Delta\sigma_{22}}{\Delta\varepsilon_{22}} \right|_{\sigma_{11}, \sigma_{33}}, \quad (33)$$

$$v_{12ST}(\underline{\underline{\sigma}}) = - \left. \frac{\Delta\varepsilon_{22}}{\Delta\varepsilon_{11}} \right|_{\sigma_{22}, \sigma_{33}}, \quad (34)$$

$$v_{13ST}(\underline{\underline{\sigma}}) = - \left. \frac{\Delta\varepsilon_{33}}{\Delta\varepsilon_{11}} \right|_{\sigma_{22}, \sigma_{33}}, \quad (35)$$

and

$$v_{31ST}(\underline{\underline{\sigma}}) = - \left. \frac{\Delta\varepsilon_{11}}{\Delta\varepsilon_{33}} \right|_{\sigma_{11}, \sigma_{22}} = - \left. \frac{\Delta\varepsilon_{22}}{\Delta\varepsilon_{33}} \right|_{\sigma_{11}, \sigma_{22}}, \quad (36)$$

where K_{ST} , E_{ST} , and v_{ST} are the stress-dependent quasi-static bulk modulus, Young's moduli, and Poisson's ratios. K_{ST} is calculated under isotropic stress conditions by measuring the change in volumetric strain $\Delta\varepsilon_{vol}$ due to a change in mean stress $\Delta\sigma_m$. E_{hST} , v_{12ST} , and v_{13ST} are measured on 90° plugs when deviatoric loading is in the direction parallel to bedding, whereas E_{vST} and v_{31ST} are measured on 0° plugs when loading is perpendicular to bedding (Figure 2-2).

The static moduli calculated from Equations 31-36 are large-strain moduli, which include plastic strains and creep that at some point during deviatoric loading make the assumption of elasticity invalid. Ramos et al. (2017) showed that the onset of appreciable plastic deformation and damage can be identified by an increase in stress-induced anisotropy between the independent dynamic measurements of c_{44} and c_{55} . Therefore, we

applied this method to limit our modeling efforts to the elastic portion of deviatoric loading in Chapter 6.

3.2 COMBINING MEASUREMENTS FROM MULTIPLE CORES TO EVALUATE DEVIATORIC STRESS DEPENDENCE

Calculation of the VTI stiffness terms requires measurements from three independent samples. However, layering orientation and sample heterogeneity cause strength variability among plugs, which complicates the comparisons of their deformational behaviors during deviatoric loading. For example, when subjected to the same confining stress, Mancos plugs at 90° generally fail at a higher deviatoric stress than 45° plugs (Figure 2-4). Because peak stress differs between plugs, the transition from primarily elastic to inelastic deformation likely occurs at different deviatoric stress magnitudes. Therefore, using a common magnitude of deviatoric stress at which to compare measurements from several plugs is inadequate. Instead, measurements should be normalized with respect to each sample's peak failure stress, then combined to calculate mechanical properties as a function of each sample's peak stress.

Normalizing measurements with respect to peak stress assumes that the magnitude of deviatoric stress does not dictate changes in elastic properties; instead, properties should depend on the fraction of peak stress at which they are measured. This assumption is similar to the testing standard ASTM-D7012-14, which outlines the measurement of isotropic tangent Young's moduli and Poisson's ratios at a fixed percentage of peak stress to compare properties among multiple samples. In Chapter 4, we provide evidence for the

validity of this assumption, where static and dynamic indicators for the onset of inelastic deformation are directly proportional to the peak stress at which the sample fails. Our method extends these principals to anisotropic rocks. Therefore, static and dynamic properties measured during deviatoric loading are shown at the i -th percent of peak failure stress for each core $\sigma_1 = \left(\frac{i}{100}\right) \sigma_{1F}$.

4. The Use of Shear-Wave Anisotropy to Quantify the Onset of Stress-Induced Microfracturing

Matthew J. Ramos, D. Nicolas Espinoza, Carlos Torres-Verdín, and Tarun Grover

4.1 CHAPTER ABSTRACT

Microfracturing and induced elastic anisotropy impart changes on body wave velocities with implications to seismic and wellbore testing methods and interpretation. We conduct simultaneous triaxial stress tests and ultrasonic wave propagation monitoring to quantify shear-wave anisotropy and microfracture development in Berea Sandstone and Silurian Dolomite. The onset of stress-induced microfracturing is detected at the beginning of appreciable shear-wave anisotropy called the “shear-wave crossover” (*SWX*). The *SWX* and subsequent increases in shear-wave anisotropy evidence microstructural damage development well before quasi-static indicators such as the volumetric strain point of positive dilatancy (*PPD*) and yield/failure in all samples. X-ray microtomography confirmed fracture development and allowed for geometric assessment of fracture orientation. Stresses at the *SWX* and *PPD* were compared to peak axial stress to understand linkages between damage and ultimate rock strength. In Berea Sandstone, the *SWX* occurs at 40% to 60% of the peak axial stress, while in Silurian Dolomite, *SWX* occurs at about 60% to 80% of the peak axial stress. Results indicate that rock samples undergo irreversible microstructural changes before dilatancy manifests, and earlier than previously thought. Analysis of tangent elastic coefficients show that the ratio between dynamic and static Young’s moduli can change significantly prior to *SWX* due to elastic and inelastic processes induced by deviatoric loading and ranges from approximately 2:1 to 4:1 for Berea and 2:1

to 7:1 for Silurian. Understanding damage development and the relationship between the dynamic and static responses of rocks provides opportunities to upscale stress-strain behavior to the wellbore environment and improved geomechanical interpretation from dipole sonic and time-lapse well log analyses.

4.2 INTRODUCTION

Rocks exhibit elastic and inelastic behavior in response to stress loading. Both of these processes can transform an isotropic rock into a material that exhibits anisotropic properties, usually through different physical mechanisms. Identifying and detecting the transition between elastic behavior and irreversible inelastic processes remains a challenge and is vital for accurately estimating rock stress-strain behavior and links between damage and permeability (Scholz 1968, Gueguen and Schubnel 2003, De Paola et al. 2009).

Nonlinear elastic deformation is a reversible process often linked to pore/grain contact compliance and the closure of pre-existing micro-fractures (Walsh 1965, Batzle et al. 1980, Shapiro 2003). The relative contribution of these mechanisms to rock elastic anisotropy and nonlinearity depends on the orientation of stresses with respect to compliant microstructural components, stress loading path, and rock type (Eberhart-Phillips et al. 1989, Schwartz et al. 1994, Johnson and Rasolofosaon 1996). For example, loading in a preferential direction can cause an isotropic rock to behave anisotropically (Nur and Simmons 1969, Dillen et al. 1999, Sarkar et al. 2003, Scott and Abousleiman 2005). Anisotropic nonlinear elastic behavior has also been validated through modeling, where accounting for actual physical mechanisms such as micro-fracture closure and pore/grain

compliance helps explain the stress-dependence of rock stiffness (Mavko et al. 1995, Winkler and Liu 1996, Prioul et al. 2001, Prioul et al. 2004). By incorporating nonlinearity, numerical models can more accurately estimate in-situ rock mechanical properties from laboratory and field data (Sinha and Kostek 1996, Sinha and Winkler 1999, Shapiro and Kaselow 2005).

With increasing stress, rocks may exhibit irreversible inelastic processes, which also depend on rock type, length scale, and stress path (Lockner 1993). For example, laboratory studies show that rocks subjected to large mean stresses typically exhibit inelastic compaction associated with pore collapse and grain crushing, whereas deviatoric stress loading often results in shear localization and the formation of new micro- and macro-scale fractures (Scholz 1968, Zhang et al. 1990, Hazzard et al. 2000, Jaeger et al. 2009). Failure in a strain softening material subjected to deviatoric loading causes strains to localize into microfractures and shear bands (Horii and Nemat-Nasser 1985, Lenoir et al. 2007, Fjaer 2008, Jaeger et al. 2009). Damage and failure may be accompanied by dilatancy, during which microfractures open perpendicularly to the shear plane. Ultimately, the rock fails as microfractures coalesce into macro-scale discontinuities (Lockner 1995, Bésuelle et al. 2000).

Elastic wave propagation is commonly utilized to evaluate rock mechanical properties and their dependence on stress and damage on several scales (Donald and Bratton 2006, Fortin et al. 2007, Prioul and Jocker 2009, Gurevich et al. 2011, Liu and Martinez 2013, Madadi et al. 2013, Collet et al. 2014). Shear waves are more sensitive to changes in structural material properties than compressional waves, and when a shear wave

interacts with a discontinuity, shear wave splitting occurs, causing a single wave to split into polarized fast and slow components (Ass'ad et al. 1992, Armstrong et al. 1994, Brie et al. 1998, Sayers 2002, de Almeida et al. 2008). Shear-wave splitting and shear-wave anisotropy calculated from two shear waves with perpendicular particle motion directions have been observed at the core, wellbore, and seismic scales and may reveal information about stress anisotropy, fabric anisotropy, and alignment of pre-existing microfractures (Nur and Simmons 1969, Crampin 1981, Sayers et al. 1990, Winkler et al. 1998, Prioul et al. 2007, de Figueiredo et al. 2012, Lei et al. 2012). A number of numerical models have been used to relate these measurements at different length scales (Pyrak Nolte et al. 1990, Sayers 2002, Prioul et al. 2004, Grechka and Kachanov 2006). For example, at the wellbore scale, models can be used to estimate nonlinear elastic properties from dipole sonic measurements of shear wave anisotropy due to changes in borehole pressure (Sinha and Kostek 1996, Sinha and Winkler 1999).

Several laboratory methods are useful for monitoring damage evolution in rocks upon deviatoric loading and inelastic processes and damage (Scholz 1968, Fortin et al. 2009, Bornert 2010). Common methods include evaluation of changes in static and dynamic elastic properties, acoustic emissions, time-lapse photography, and use of X-ray tomography (Horii and Nemat-Nasser 1985, Lockner 1993 and 1995, Stanchits et al. 2006 and 2012, Fjaer 2009, Alsalman et al. 2015). Although each method provides insight into micro and macro scale deformation, many are limited in their ability to pinpoint the onset of inelastic processes, such as microfracture development (Ayling et al. 1995).

Volumetric strain is the simplest method to monitor damage-induced dilatancy (Nemat-Nasser and Obata 1988, Rawling et al. 2002, Wassermann et al. 2009). Multistage triaxial testing estimates rock failure properties by subjecting a single rock specimen to several cycles of deviatoric axial loading, each at a different confining stress. Each cycle is stopped as rock volumetric deformation becomes dilatant, at the point of positive dilatancy (*PPD*). However, the relatively high stresses and strains incurred by the sample during multistage testing often seem to surpass the limits of allowable damage before irreversible mechanical degradation occurs, such that samples are deemed unfit for subsequent testing (Caia et al. 2004, Alsalman et al. 2015, Ramos et al. 2017). Not all rocks may exhibit dilatant behavior upon deviatoric loading. Other robust damage characterization methods, such as acoustic emissions and time-lapse X-ray microtomography, require extremely specialized testing equipment, as well as time and expertise for processing the large quantities of collected data.

The objective of this study is to detect the onset of inelastic processes, such as stress-induced rock damage and development of microfractures, by investigating the influence of varying deviatoric stress on ultrasonic shear wave propagation. We monitor the evolution of shear-wave anisotropy during axi-symmetric deviatoric loading and compare it to quasi-static indicators such as the point of positive dilatancy (*PPD*) and peak failure stresses. Contrary to most studies regarding elastic wave anisotropy and shear-wave splitting (Zheng 2000, Gao and Crampin 2003), in this study we refer to shear wave anisotropy as measured in pre-established perpendicular planes of particle motion but subjected to a symmetric stress field. Therefore, shear waves are influenced only by

changing material properties, e.g., damage and microfracture development and, during deviatoric stress loading. Experimental results for Berea Sandstone and Silurian Dolomite highlight the versatility of shear-wave anisotropy to (1) identify the onset of microfracture growth and damage development at lower stresses and strains than other techniques, (2) provide estimates of rock failure properties from dynamic measurements, and (3) define limits for utilizing elastic parameters, such Young’s modulus, to relate static and dynamic rock deformational behaviors.

4.3 CALCULATION OF SHEAR-WAVE ANISOTROPY

Shear stiffness in the planes 1-3 c_{55} and 2-3 c_{44} can be calculated through shear-wave velocities S_x and S_y with parallel propagation directions and perpendicular particle motion, from Equations 7 and 8. Changes in c_{55} and c_{44} group both elastic and inelastic processes. We define shear-wave crossover (SWX) point at a threshold of 1% anisotropy to account for minor intrinsic anisotropy due to rock fabric. Hence, SWX occurs at

$$\frac{\frac{c_{44} - c_{55}}{c_{44} + c_{55}}}{2} \geq 1\% \quad . \quad (37)$$

4.4 RESULTS

Figure 4-1-A shows stress-strain curves from a typical deviatoric loading test exemplified by a Berea sample under 10.3 MPa radial stress. The sample was briefly unloaded at $\sigma_1 = 27.5$ and 41 MPa to evaluate unloading elastic moduli. Figure 4-1-B shows

shear waveforms S_x and S_y collected for the test in Figure 4-1-A as a function of deviatoric stress, from which shear-wave velocities V_{sx} and V_{sy} are calculated from the respective corrected travel times. As deviatoric stress increases, samples undergo changes in mechanical properties, detected by increases in shear-wave anisotropy as evidenced in Figure 4-1-B. Shear-wave anisotropy increases with further deviatoric loading, and volumetric strain transitions from contraction to dilation (point of positive dilatancy – *PPD*). Continued deviatoric loading causes the rock sample to reach a peak stress and eventually fail.

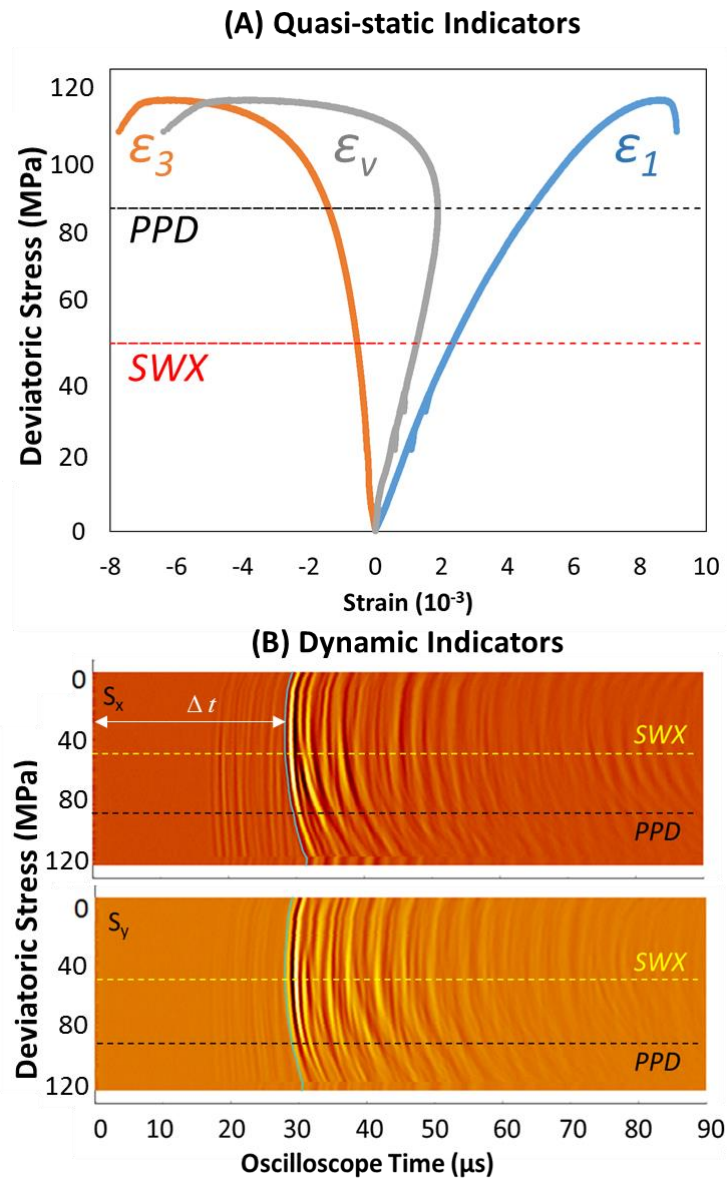


Figure 4-1 Berea Sandstone deviatoric loading experiment at effective confining stress $\sigma_3 = 10.3$ MPa (1,500 psi). (A) Stress vs strain plots for radial (ϵ_3), volumetric (ϵ_v), and axial (ϵ_1) strains. The black dashed line indicates the point of positive dilatancy (*PPD*) and the red line is the shear-wave crossover (*SWX*). (B) Shear waveforms S_x and S_y as a function of deviatoric stress. The blue line represents the picked first arrival for each recorded waveform, while the white arrow shows the time elapsed Δt between the triggered pulser and first arrival. The yellow and black dashed lines represent the *SWX* and *PPD*, respectively. Note the shear-wave anisotropy increases as the S_x wave arrival times increase.

4.4.1 Shear-Wave Crossover (SWX)

Figure 4-2-A shows dynamic stiffness coefficients c_{44} and c_{55} for the Berea Sandstone (block 1) test in Figure 4-1-A and 4-1-B, where *SWX* occurs at $\sigma_1 = 60.9$ MPa, and the *PPD* at $\sigma_1 = 97.6$ MPa. Between *SWX* and *PPD*, the sample undergoes almost twice as much volumetric deformation, which is concurrent with an increase of shear-wave anisotropy of c_{44} and c_{55} of 3%. As stresses exceed the *PPD*, volumetric strain becomes dilatant, dynamic shear moduli decrease, and shear-wave anisotropy increases to 6.5%. Most Berea tests exhibit similar behavior to Figure 4-2-A, with increasing shear-wave anisotropy prior to the *PPD*, and decreasing dynamic shear moduli as samples transition to dilatant volumetric deformation. Figure 4-2-B shows an example for Silurian Dolomite which is revisited in Section 4.3.

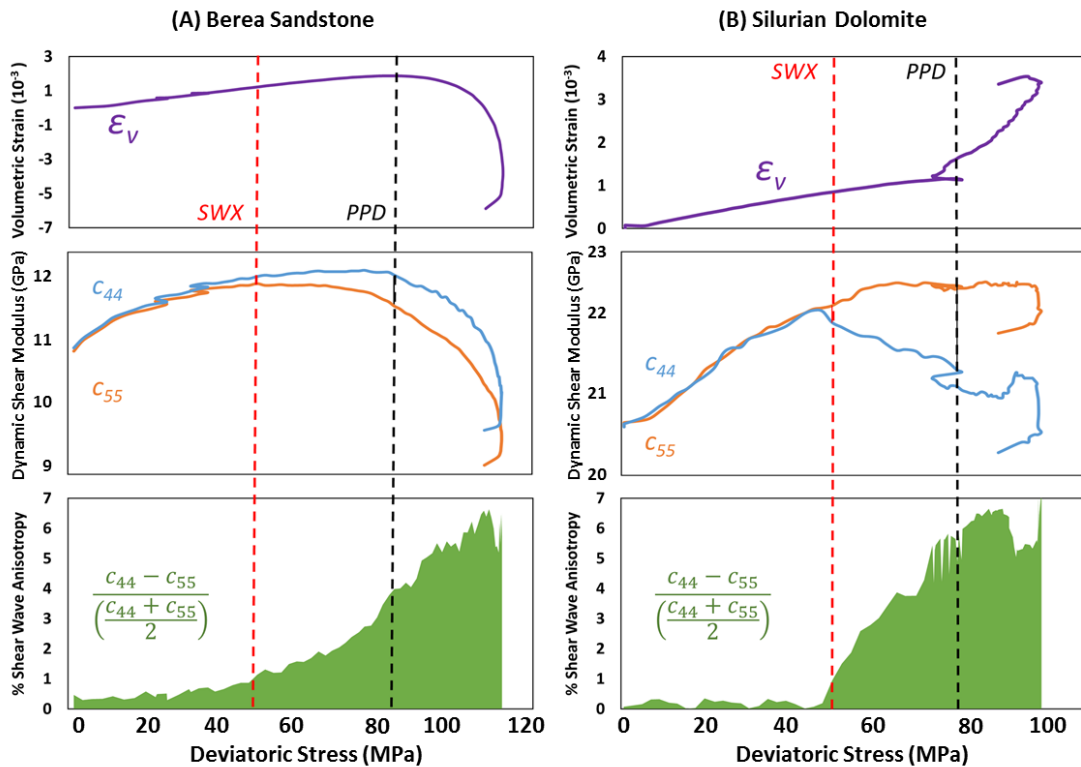


Figure 4-2 Comparison of volumetric strain ϵ_v (top), dynamic shear moduli c_{44} and c_{55} (middle), and the resulting shear-wave anisotropy (bottom) for (A) Berea Sandstone (block 1) and (B) Silurian Dolomite, both confined at $\sigma_3 = 10.3$ MPa (1,500 psi). The shear-wave crossover SWX and the point of positive dilatancy PPD are shown with red and black dashed lines, respectively.

4.4.2 Berea Sandstone: SWX, PPD and peak strength

Table 4-1 summarizes all experimental results for Berea Sandstone. Figure 4-3-A compares the effective axial stresses at SWX, PPD, and peak as a function of confining radial stress. The scatter in the data is due to mixing results from two different Berea Sandstone blocks. When analyzed separately, data from each block aligns with well-defined trends, indicating that SWX is followed by PPD, and then by peak strength. For example, rocks from block 1 have a cohesive strength of 12.78 MPa and friction angle

43.4°, whereas rocks from block 2 have cohesive strength of 10.63 MPa and friction angle of 41.8°. For each block, peak stress and *PPD* increase with confining stress with a similar slope (directly proportional to friction angle), whereas *SWX* increases less steeply with confining stress.

Table 4-1 Tested rock samples, bulk mass density (dry), porosity, confining stresses, and axial stress at *SWX*, *PPD*, and peak. (*) Porosity calculated assuming mineral densities of quartz = 2.65 g/cm³ and dolomite = 2.87 g/cm³. (**) Denotes sample that did not exhibit a *PPD*.

Rock Type	Bulk mass density ρ (g/cm ³)	Porosity* (v/v)	Effective confining (radial) stress σ_3 (MPa) (psi)	Effective Axial Stress		
				σ_1 at <i>SWX</i> (MPa)	σ_1 at <i>PPD</i> (MPa)	σ_1 at Peak (MPa)
Berea Sandstone Block 1	2.09	0.212	0.69 (100)	18.5	23.9	54.5
	2.09	0.212	3.4 (500)	39.1	60.0	89.5
	2.09	0.211	6.9 (1000)	48.8	74.2	98.0
	2.11	0.205	6.9 (1000)	52.6	56.9	80.0
	2.09	0.210	10.3 (1500)	60.9	97.6	126.3
	2.11	0.205	20.7 (3000)	92.1	143.5	168.9
Berea Sandstone Block 2	2.00	0.245	0.69 (100)	23.2	28.4	41.0
	2.01	0.240	3.4 (500)	33.5	40.5	63.6
	2.01	0.243	6.9 (1000)	38.0	62.2	81.8
	2.00	0.247	10.3 (1500)	45.4	81.7	99.1
	2.01	0.242	13.8 (2000)	60.1	97.7	117.6
Silurian Dolomite	2.42	0.158	0.69 (100)	28.2	48.1	48.1
	2.37	0.175	0.69 (100)	44.2	58.0	62.3
	2.37	0.174	3.4 (500)	47.6	59.0	60.4
	2.42	0.156	3.4 (500)	42.6	53.0	53.3
	2.58	0.101	6.9 (1000)	35.4	**	41.0
	2.49	0.132	6.9 (1000)	79.0	103.2	106.5
	2.44	0.151	6.9 (1000)	54.3	69.0	96.8
	2.34	0.184	10.3 (1500)	60.7	90.6	111.4
	2.47	0.140	10.3 (1500)	43.5	59.8	61.7

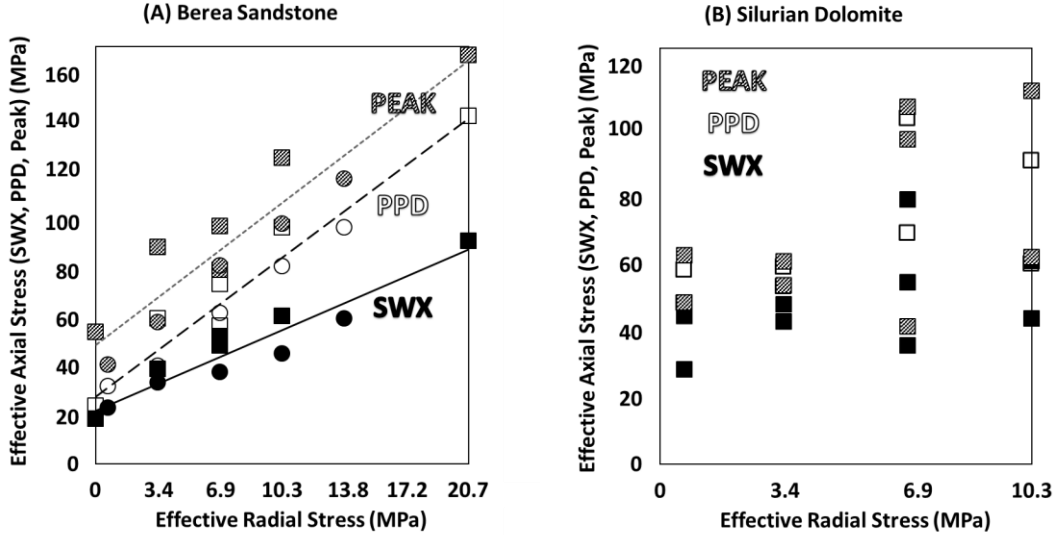


Figure 4-3 Effective axial stress at SWX (filled), PPD (empty), and Peak (hashed) as a function of radial confining stress for (A) Berea Sandstone: block 1 (■) and block 2 (●), and (B) Silurian Dolomite. Straight lines show linear fits for Berea Sandstone.

4.4.3 Silurian Dolomite: SWX, PPD and peak strength

Figure 4-2-B shows the volumetric strain and shear wave anisotropy as a function of deviatoric stress for a Silurian Dolomite sample at $\sigma_3 = 10.3$ MPa. Sample deformation occurs primarily in the axial direction up to the *PPD* at $\sigma_1 = 90.6$ MPa, where the sample appears to dilate briefly, followed by rapid axial contraction, and steady axial shortening for the remainder of the test. The sample undergoes large changes in stress and strain between the *SWX* ($\sigma_1 = 60.7$ MPa) and *PPD* (90.6 MPa). Between these two characteristic stresses, dynamic shear moduli diverge, where c_{44} decreases after the *SWX*, and c_{55} increases slightly until shear failure. Shear-wave anisotropy increases to roughly 5% between the *SWX* and *PPD*. Similar to Figure 4-2-B, several Silurian samples exhibit axial contraction as the sample enters dilatancy, where stress drops instantaneously and axial

shortening is observed with little to no change in radial strain. Dilatancy did not occur in one Silurian Dolomite test (see Table 4-1).

Experimental results for Silurian Dolomite samples are compiled in Table 4-1. Figure 4-3-B shows the dependences of effective axial stress at *SWX*, *PPD*, and Peak on radial confining stress. Results exhibit no visible relation with confining stress, likely as a result of natural carbonate heterogeneity, where porosity is $15.2 \pm 4.1\%$ within the sample set and pore geometries vary considerably within a single sample. Overall, there is no clear trend that permits identifying statistically meaningful cohesive strength, friction angle, and respective line fitting constants for *PPD* and *SWX* as a function of confining stress σ_3 .

4.5 ANALYSIS AND DISCUSSION

4.5.1 Onset of damage from shear-wave anisotropy and dilatancy

An increase in confining stress is known to increase rock shear strength (Hoek et al. 2002). Therefore, an increase in confining stress would also require increased deviatoric stress to induce dilatant behavior (*PPD*) and possibly also induce appreciable shear-wave anisotropy (*SWX*). In order to visualize *SWX*, *PPD*, and peak stress data independently of confining stress, Figure 4-4-A and 4-4-B show the relationship between effective axial stresses at *SWX* and *PPD* relative to peak stress. Results from Berea samples in Figure 4-4-A indicate that *SWX* and *PPD* are approximately 0.5 and 0.75 of the peak stress, respectively. These ratios are consistent regardless of the original Berea block or confining stress, making them unique for this type of sandstone. Results from Silurian samples in

Figure 4-4-B show that *SWX* occurs at approximately 0.75 of the peak stress and often the stress at *PPD* is approximately of the same magnitude of the peak stress. Consistent data trends between *SWX* and peak stresses suggest a unique relationship between stress-induced shear-wave anisotropy and rock failure for a given rock type. Therefore, shear-wave anisotropy is likely affected by the same mechanisms that cause dilatancy and ultimate failure, and a proper selection of a *SWX* threshold could pinpoint the onset of damage.

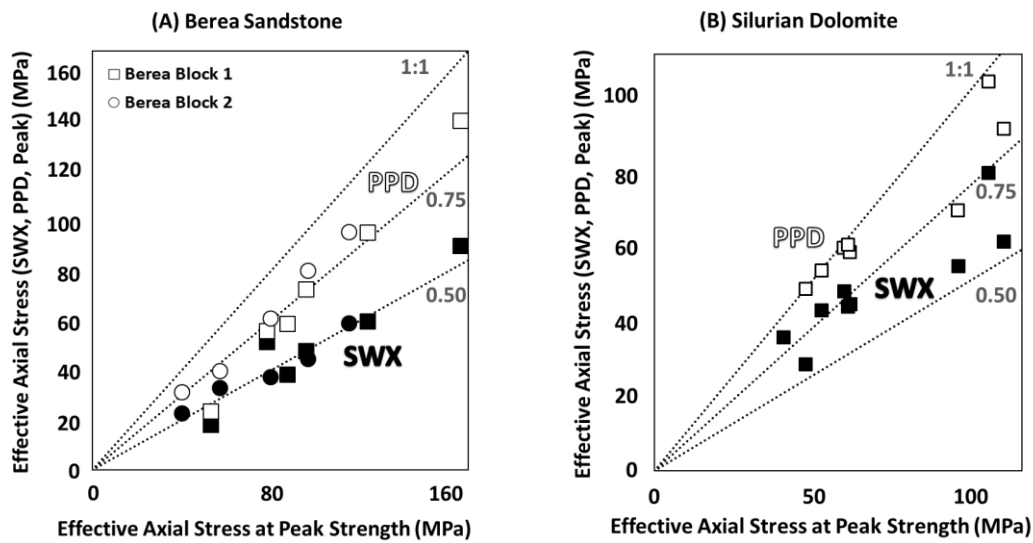


Figure 4-4 Relationship between the effective axial stress at the *PPD* (empty) and *SWX* (filled) and effective axial stress at peak strength for (A) Berea Sandstone: block 1 (■) and block 2 (●), and (B) Silurian Dolomite. Dashed lines represent 1:1, 0.75, and 0.5 ratio of effective axial stress at the *PPD* and *SWX* to effective axial stress at peak strength.

The *PPD* is used in multistage testing as a “pseudo-nondestructive” method for estimating shear strength properties using a single rock sample (that exhibits dilation) at several radial stresses (Gatelier et al. 2002, Wassermann et al. 2009, Alsalman et al. 2015). However, our results indicate that significant shear-wave anisotropy develops well before

the *PPD*, suggesting enough damage to alter wave propagation as well as quasi-static elastic and strength properties. Because *SWX* occurs before *PPD*, stopping deviatoric loading at *SWX* for multistage testing may not only allow for estimation of rock failure properties, but also help to preserve sample competence for subsequent loading cycles. Figures 4-5-A and 4-5-B compare the degree of shear-wave anisotropy as a function of stress at *SWX*, *PPD*, and peak. Both rock types almost always exhibit a shear-wave anisotropy of 2% or greater at the *PPD*. Most Berea samples show almost monotonic increase in shear-wave anisotropy between *SWX*, *PPD*, and peak, likely due an increase in microfractures of similar orientation. *PPD* and peak stress are relatively close in Silurian samples and therefore exhibit comparable degrees of shear-wave anisotropy at these two points.

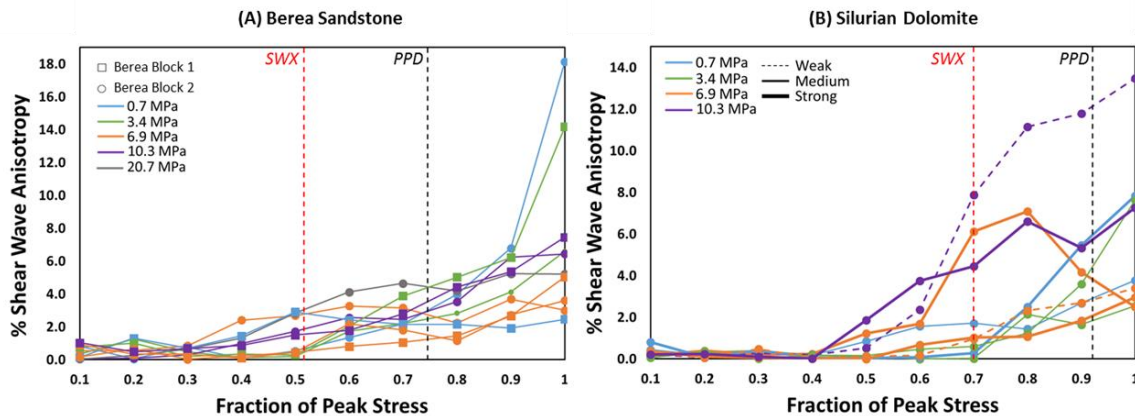


Figure 4-5 Shear-wave anisotropy as a function of the fraction of peak stress at which they occur for (A) Berea Sandstone: block 1 (■) and block 2 (●), and (B) Silurian Dolomite samples (separated by strength: weak, medium, and strong based in shear strength). The average shear-wave crossover *SWX* and point of positive dilatancy *PPD* are shown for each rock type with the red and black dashed lines, respectively.

Acoustic emission monitoring also supports the utility of dynamic measurements for assessing changing rock microstructure. The onset of significant acoustic emission events in basalt and granite occurs before or coincident with dilatancy, and increases in horizontal shear-wave anisotropy are detected well before dilatancy (Stanchits et al. 2006). Scholz (1968) also shows microfracture-related acoustic emission events prior to dilatancy and at roughly 50% of peak stress for several rock types. Analogous acoustic emissions analyses from hydraulic fracturing experiments help anticipate and track hydraulic fracturing propagation (Stanchits et al. 2012). Our experiments did not involve pore fluids. However, variations in wave propagation velocity earlier than dilatancy has also been documented in experiments involving acoustic emission from fluid saturated rocks (Baud et al. 2004, Stanchits et al. 2009, Fortin et al. 2009). Yet, deviatoric loading of saturated samples at relatively high strain rates could induce undrained loading conditions and excess pore pressure and therefore change total stress onsets for damage.

Understanding mechanisms and timing of induced damage is important to interpret deviatoric loading tests. Utilizing shear wave crossover for estimating damage and failure stresses may provide a dynamic means for defining the onset of inelasticity. Section 5.2 utilizes both static and dynamic measurements to explore the effect of damage on variation of elastic moduli.

4.5.2 Evolution of dynamic and static moduli with deviatoric loading and induced damage

Figures 4-6-A and 4-6-B (top-middle) show the evolution of quasi-static axial stiffness $\Delta\sigma_1/\Delta\varepsilon_1$ and relative radial expansion to axial shortening $-\varepsilon_3/\varepsilon_1$, measured at 10% increments of peak stress. For visual simplicity, Figure 4-6-A includes only Berea Block 2 samples. These two quantities can be interpreted as the quasi-static Young's modulus and Poisson's ratio assuming isotropic linear elasticity (Equations 1 and 2).

In general, stiffness decreases after reaching a local peak (if any) and radial expansion increases with increasing deviatoric stress. As expected, samples under higher confining stresses exhibit higher stiffness than those under low confinement. Dashed lines mark the average *SWX* and *PPD* for each type of rock and highlight the effect of damage in (1) lowering axial stiffness (lower static Young's modulus) and (2) giving unreasonably high Poisson's ratios beyond *SWX* if one were to assume isotropy.

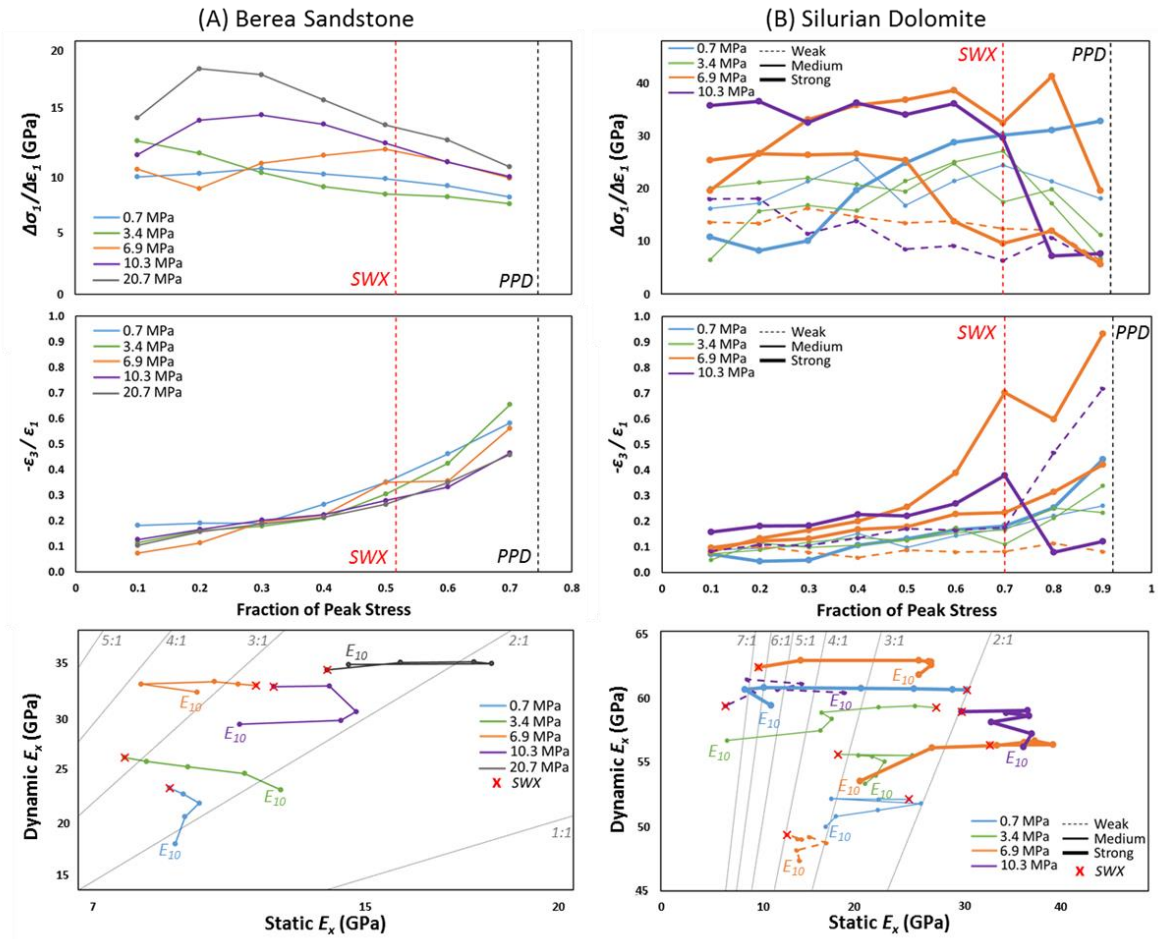


Figure 4-6 Comparison of static axial stiffness $\Delta\sigma_1/\Delta\varepsilon_1$ (top) and ratio of radial expansion to axial shortening $-\varepsilon_3/\varepsilon_1$ (middle) as a function of the fraction of peak stress at which they were measured, and the corresponding dynamic-to-static transforms of Young's modulus assuming isotropy (bottom) for (A) Berea Sandstone block 2 and (B) Silurian samples (separated by strength: weak, medium, and strong). Red and black vertical dashed lines represent the average fraction of peak stress at which the SWX and PPD occur for each rock. Dynamic-static transforms are marked with E^{10} to delineate starting points of each test and (x) to show the SWX. Thin gray lines are marked with their slope as reference for changing dynamic to static ratios during each test.

Figures 4-6-A and 4-6-B (bottom) show the evolution of quasi-static Young's modulus E_{st}^i and dynamic Young's modulus E_{dyn}^i during loading, both calculated assuming isotropy (Equations 1 to 4). The results highlight the variability of both E_{st}^i and E_{dyn}^i

depending on the stress level chosen. E_{st}^i changes up to 100%, whereas E_{dyn}^i only changes by up to 50% in Berea Sandstone, causing the dynamic-to-static ratio E_{dyn}^i / E_{st}^i to vary between 2:1 to 4:1. Two cases are observed in Silurian samples. In the first case, samples exhibit fairly constant stiffness and radial expansion until roughly 60-70% of peak stress, whereas in the second case samples exhibit strain hardening behavior until roughly 70% of the peak stress, both are followed by strain softening until *PPD*. Strain softening samples exhibit increasing dynamic-to-static ratio E_{dyn}^i / E_{st}^i , whereas, strain hardening samples show decreasing ratios. Comparisons of dynamic and static Young's moduli show that Silurian samples change up to 300% in E_{st}^i as opposed to only 20% change in E_{dyn}^i .

The appreciable changes of stiffness and radial expansion between *SWX* and *PPD*, in addition to the proximity of *PPD* to failure, provide additional evidence for irreversible damage prior to dilatancy in both types of rock. The variability in static stiffness shows that a single tangent modulus or a value picked at 50% of peak stress (ASTM D7012-14) will not adequately describe their stress-strain behavior. Instead, considering a range of values could more accurately describe rock nonlinearity. The reader can find rigorous nonlinear elastic models elsewhere (Walsh 1965, Batzle et al. 1980, Shapiro 2003, Prioul et al. 2004).

4.5.3 Effect of micro and macro fractures on shear-wave anisotropy

Experimental results provide evidence for fractures slowing wave velocities and damage-induced shear wave anisotropy. The pre-established propagation direction of the

S_x and S_y make waves susceptible to interference from planar features such as stress-induced fractures. Fracture orientation, however, is not predetermined in our tests because of the radially symmetric stress conditions. We used X-ray micro-tomography images to map fracture orientation after failure (confining jacket kept sample together). Cross-sections in Figures 4-7-A and 4-7-B show Berea and Silurian samples after deviatoric loading to failure. In both samples, the directions of shear wave components are offset from the failure plane, but more closely oriented with the S_x component. Both tests show $V_{sx} > V_{sy}$ at the end of the test, which is expected given their orientation with respect to fracture strike. Fracture dip also influences the relative interaction between shear waves and the failure plane, where the symmetry of elastic anisotropy, and thus shear-wave anisotropy, will differ between diagonal (Figure 4-7-A) and more vertically oriented (Figure 4-7-B) failure planes.

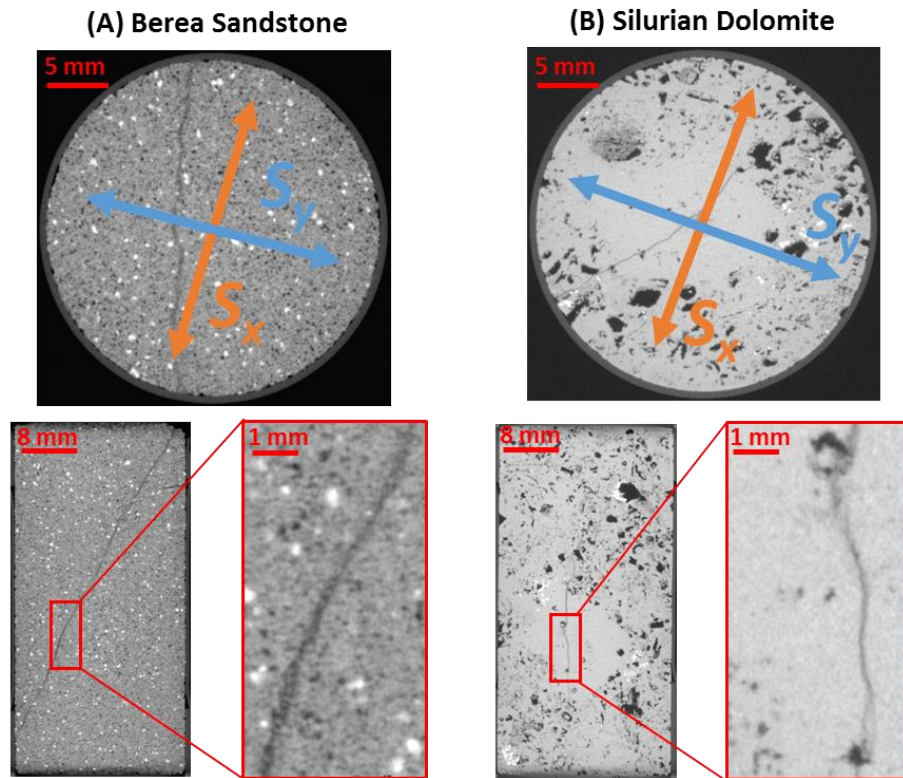


Figure 4-7 X-ray microtomography images of (A) Berea Sandstone ($\sigma_3 = 0.7$ MPa (100 psi) and $\sigma_{1Peak} = 41$ MPa (5,946 psi)) and (B) Silurian Dolomite ($\sigma_3 = 0.7$ MPa (100 psi) and $\sigma_{1Peak} = 48.1$ MPa (6,980 psi)). Horizontal cross section (Top) and vertical cross section through each core (Bottom Left) and zoomed-in image of the major failure plane for each (Bottom Right). Top images show the pre-established S_x and S_y shear waves with respect to the failure plane.

X-ray micro-tomography imaging of rock samples provides evidence for failure mechanisms, where the orientation and location of fractures and failure planes can be used to better understand static and dynamic results. In Berea Sandstone, the fracture clearly corresponds to shear failure (Figure 4-7-A). In Silurian Dolomite, the fracture plane is nearly vertical, an indication of tensile splitting (Figure 4-7-B), where large pores likely alter the local stress state and cause tension cracks during compressive testing (Nemat-Nasser and Obata 1988). All Berea samples showed clear shear failure planes, while

Silurian samples showed mixed shear failure and tensile splitting. Tensile splitting would explain the sudden decrease in stress as soon as Silurian samples exhibit dilatant behavior, with failure occurring soon after in most samples. Furthermore, Silurian samples exhibited instances of complex fracture networks as opposed to a single fracture observed in sandstones.

Effective medium theories are often used to model wave propagation through fractured rock, where fractures are assumed to be low stiffness inclusions or discontinuities of a defined geometry, orientation, and aperture within otherwise stiff rock (Hudson 1981, Schoenberg and Helbig 1994, Sayers 2004, de Figueiredo et al. 2012, Santos et al. 2015). The orientation and spatial distribution of modeled fractures largely controls their impact on wave velocities and velocity anisotropy (Crampin and McGonigle 1981, Sayers and Kachanov 1995). In addition to damage-induced shear-wave anisotropy, we generally measure decreases in wave velocity with increasing damage. This is expected because fractures tend to attenuate waves through dispersion, scattering, and mode conversion at interfaces and discontinuities, causing velocity decreases (Mavko et al. 2009). Moreover, attenuation phenomena are often amplified when fractured rocks are saturated due to wave-induced fluid flow (Gurevich et al. 2009).

4.6 CONCLUSIONS

The following conclusions hold for relatively isotropic rock samples, where effective sample anisotropy is deemed negligible compared to stress-induced anisotropy.

- Simultaneous and collocated triaxial stress testing and ultrasonic wave propagation provide an effective means for assessing stress-induced damage and microfracturing.
- Damage induced by increases of deviatoric stress in Berea Sandstone and Silurian Dolomite cause dilatancy, variations of static and dynamic elastic moduli, and divergence of perpendicularly oriented shear-wave velocities from one another, all before peak stress.
- Experimental evidence highlights nonlinear stress and strain dependence of dynamic-static transforms in tested rocks. For Berea Sandstone and Silurian Dolomite static stiffness changes by up to 100% and 300%, and dynamic moduli change by 50% and 20%, respectively, suggesting a single tangent modulus is not adequate for describing the nonlinear stress and strain dependence of rock mechanical properties.
- Changes in shear-wave anisotropy, and specifically the *SWX* (threshold set at 1% anisotropy) can be utilized for evaluating the onset of microfracturing and associated degradation of sample mechanical competence. Shear-wave anisotropy increases by as much as 6% and 12% prior to peak stress in Berea Sandstone and Silurian Dolomite.
- The *SWX* and *PPD* occur at roughly 50% and 75% of peak stress in Berea Sandstone, respectively, and occur around 75% and almost coincident with peak stress in Silurian

Dolomite. The relationship between the stresses at the *SWX*, the *PPD*, and peak suggest linkages between these points and the evolution of damage, and provide reliable estimates of peak failure stress. Although samples were tested without pore fluids, we expect the presence of fluids and pore pressures to impact the magnitude of stress at which these events occur if undrained loading develops.

- Multistage testing based on the *PPD* is not sufficient for estimation of rock failure properties without compromising sample competence. Instead, results suggest that *SWX* can be utilized in place of *PPD* to minimize stresses and strains, and therefore maintain mechanical competence for subsequent stages.
- Laboratory derived dynamic-static elastic transforms are stress-dependent and may yield erroneous results beyond the *SWX* point.

We performed laboratory tests on relatively homogeneous and isotropic rocks. These results are useful for exploring similar phenomena in laminated transversely isotropic rocks.

5. Stress-Dependent Dynamic-Static Transforms of Anisotropic Mancos Shale

Matthew J. Ramos, D. Nicolas Espinoza, Carlos Torres-Verdín, Kyle T. Spikes, and Stephen E. Laubach

5.1 CHAPTER ABSTRACT

Layering-induced anisotropy of shale formations increases uncertainty in determining in-situ mechanical properties and stresses, thus increasing the risk associated with implementing advanced drilling and hydraulic stimulation in shales. We conduct simultaneous triaxial stress tests and ultrasonic wave propagation monitoring to quantify static and dynamic stiffness anisotropy in Mancos Shale. Two case studies evidence the impacts of (1) confining stress and (2) presence of pre-existing fractures, on dynamic-static transforms of Young's moduli and Poisson's ratios with increasing deviatoric stress. The first case shows that confining stress more heavily impacts dynamic mechanical properties than static. The effect is most prominent at high deviatoric stresses, where stress-induced damage increases the difference between dynamic and static Young's moduli. The second case shows that samples with pre-existing fractures exhibit even higher differences between dynamic and static Young's moduli than non-fractured (intact) and damaged rocks. Fractured samples exhibit ratios of E_{dyn}/E_{st} between 5:1 and 7:1, whereas intact samples generally remain near the 3:1 ratio. Pre- and post-test X-ray microtomography imaging confirm that bedding planes and pre-existing fractures act as planes of weakness, while sample layering causes mechanical stratigraphy, where changes in lithology may cause fractures to reorient. Results highlight the limitations of tangent linear elasticity

moduli to explain complex deformational behavior in shales and the need for better models that address the strain-magnitude dependence of rock properties.

5.2 INTRODUCTION

Shale layering causes bed-parallel differences in rock properties, a component of mechanical stratigraphy (Laubach et al. 2009). Stratigraphic variations in mechanical properties are known to influence the growth of engineered fractures (Bodziak et al. 2014). A further element of bed-perpendicular anisotropy can be introduced by pre-existing fractures, which can impact rock stress-strain response (Bergbauer and Pollard 2004). Over geologic time, subsurface stresses may vary, which can cause natural fracturing. Chemical alteration (diagenesis) might stiffen natural fractures; therefore, their orientations might not be aligned with current stresses or layering (Laubach et al. 2004). Consequently, the attributes and orientation of layering and diagenetically altered open fractures can impact rock mechanical behavior, engineered fracture growth, and rock failure under a range of loading paths. Layering and pre-existing fractures are suspected to influence the behavior of shales undergoing hydraulic fracture treatment (Suarez-Rivera et al. 2013, Gale et al. 2014).

Mechanical properties are measured on several scales, including: millimeter to centimeter scale static and ultrasonic measurements on core plugs, meter scale acoustic well-logging of the near-wellbore region, and significantly larger scale (10's of meters to km) surface seismic surveying (Eberhardt et al. 1998, De Almeida et al. 2008). Each measurement bears important information about subsurface mechanical properties.

However, upscaling between core and seismic scales is commonly limited by measurement resolution with respect to the scale of internal rock heterogeneity (Holt et al. 2012). Furthermore, relating the purely elastic dynamic measurements (ultrasonic, borehole sonic, seismic) to static measurements (core scale stress-strain testing) provides an additional challenge. Static measurements are representative of both elastic and plastic deformation, thus they likely more closely represent the rock behavior in response to large strains imposed during drilling and hydraulic fracturing (Zoback 2007).

Although static measurements more accurately represent subsurface rock behavior, they typically can only be obtained in the laboratory and vary considerably from dynamically measured rock properties at the same scale. For example, the small elastic strains imparted through dynamic testing ($\varepsilon \approx 10^{-7}$) frequently yield several times higher dynamic moduli than static measurements that require higher strains ($\varepsilon \approx 10^{-2}$ - 10^{-3}) and exhibit plastic strains and creep (Ciccotti and Mulargia 2004, Mavko et al. 2009, Frydman et al. 2016, Ramos et al. 2017). Therefore, simultaneous dynamic and static measurements are required for the development of dynamic-static transforms $(E_{st}, \nu_{st}) = f(E_{dyn}, \nu_{dyn})$, which can be applied to dynamic measurements (such as acoustic well logs) to estimate the in-situ static moduli and subsurface stresses (Yale et al. 1994, Fjaer 1999).

Dynamic-static transforms have been attempted in Mancos and other shales (Fjaer and Nes 2013, Mikhaltsevitch et al. 2016). For example, previous studies of Mancos Shale show dynamic Young's moduli being more than double those measured statically (Holt et al. 2013). However, to the best of our knowledge, no attempts have been made to utilize

anisotropic moduli to evaluate layering-induced stiffness anisotropy and the effect of pre-existing fractures on these rock properties. Furthermore, previous work did not attempt to investigate the impact of stress-induced damage during deviatoric loading to failure (Liming and Fjaer 2012, Holt et al. 2012, Holt et al. 2013).

The objective of our paper is to develop accurate dynamic-static transforms in Mancos Shale by investigating the influence of varying deviatoric stress on quasi-static strain measurements and ultrasonic compressive P and shear-wave S propagation. Our measurements are based on axi-symmetric deviatoric loading of cores taken perpendicular, parallel, and at 45° to bedding. Stiffness anisotropy is evaluated as a function of confining stress, deviatoric stress and induced damage, and presence (or absence) of pre-existing fractures. X-ray microtomography imaging is performed to visualize rock microstructure and pre-existing fractures prior to testing, as well as to ascertain whether stress-induced fractures interact with those features when samples are loaded deviatorically to failure.

5.3 RESULTS

5.3.1 Case 1: Effects of Confining Stress on Non-Fractured Samples

Figure 5-1 shows that initial ratios of dynamic to static moduli for E_h and E_v are typically between 2:1 and 3:1. In general, E_h exhibits higher static and dynamic moduli than E_v . Dynamic moduli tend to increase monotonically with both confining stress and deviatoric stress. The effect of confining stresses on static moduli is not readily apparent. Static E_h increases until roughly 40-50% of peak stress, whereas static E_v remain relatively

constant. Above roughly 50% of peak stress, static E_h and E_v decrease until failure. Overall, dynamic to static ratios decrease for the first half of deviatoric stress loading, then increase thereafter. The effect of confining stress on loading or unloading (not shown) moduli is unclear and may be hindered by rock heterogeneity and the use of relatively small variations of confining stress.

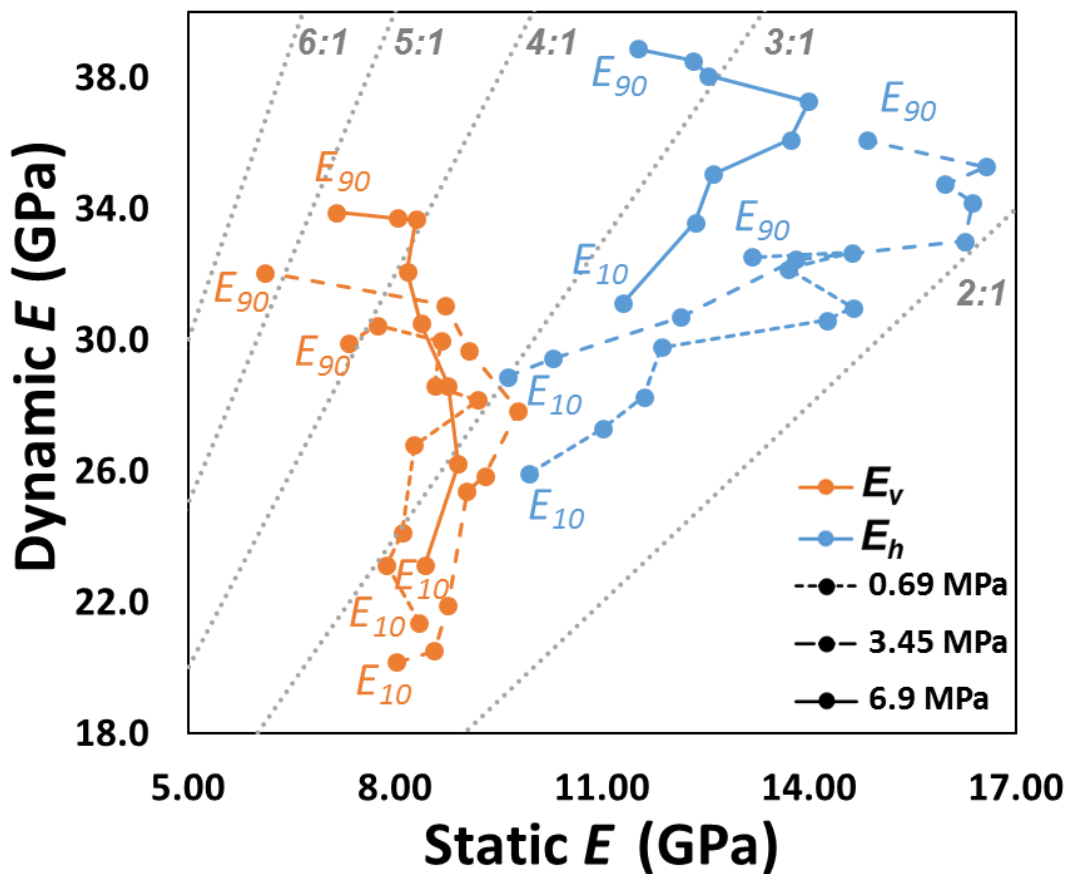


Figure 5-1 Dynamic-static transforms for Young's moduli E_v (orange) and E_h (blue) for 0.69 MPa (short dash), 3.45 MPa (long dash), and 6.9 MPa (solid) confining stresses. Each line is marked with E_{10} and E_{90} to denote the starting and ending points of the test (10% and 90% of peak stress), respectively, whereas thin gray lines are marked with their slope as reference for dynamic to static ratios.

Figure 5-2 shows an insensitivity of Poisson's ratios to confining stress at low deviatoric stresses. Above 50% of peak stress, however, dynamic to static ratios exhibit a hierarchy with respect to confining stress. Dynamic-static ratios of ν_{12} increase, whereas ratios for ν_{13} and ν_{31} decrease with increasing confining stress. Loading ν_{ST} varies from 0 to 0.5, and beyond 0.5 with dilation near failure. It should be noted that ν_{ST} larger than 0.5 is not possible. These values correspond to dilatant rock deformation.

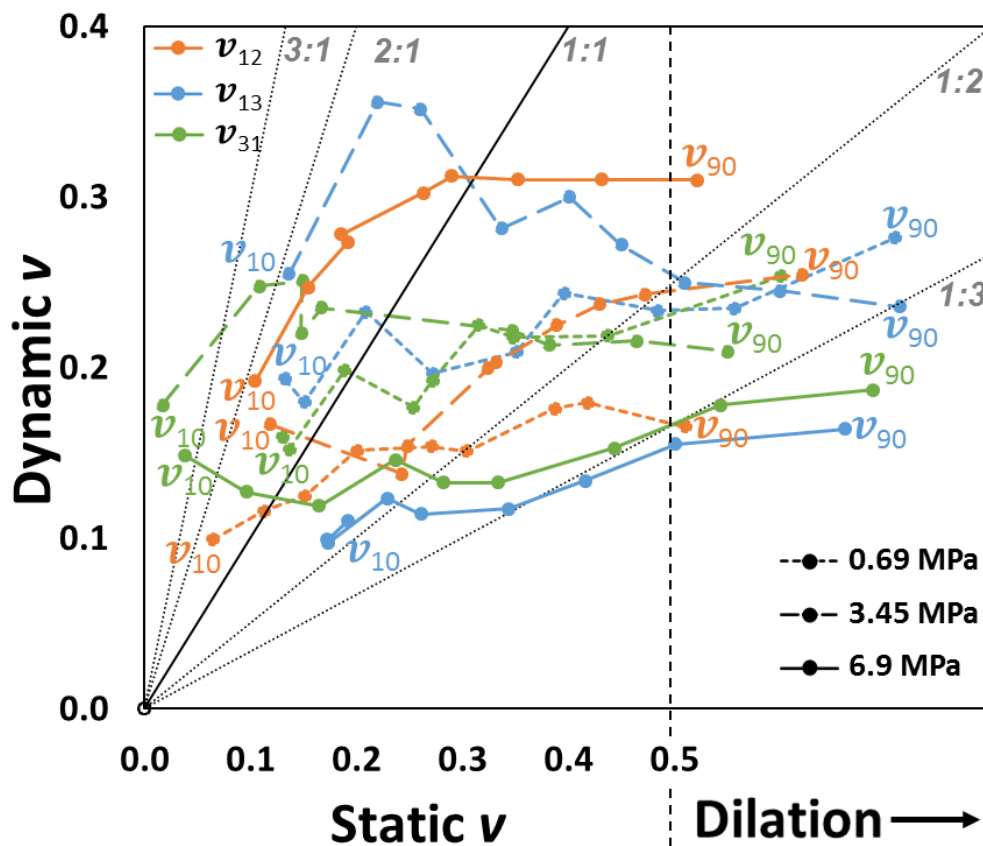


Figure 5-2 Dynamic-static transforms for Poisson's ratios ν_{12} (orange), ν_{13} (blue), and ν_{31} (green) for 0.69 MPa (short dash), 3.45 MPa (long dash), and 6.9 MPa (solid) confining stresses. Each line is marked with ν_{10} and ν_{90} to denote the test starting and ending points (10% and 90% of peak stress), respectively, while thin gray lines are marked with their slope as reference for dynamic to static ratios. The vertical dashed line at 0.5 indicates the transition to dilatant behavior.

5.3.2 Case 2: Effects of Pre-Existing Fractures

Figure 5-3 shows the impact of pre-existing fractures on dynamic-static transforms of Young's moduli. Fractured samples exhibit much higher ratios of dynamic to static moduli, which decrease with deviatoric stress up to roughly 50-60% of peak stress, indicating appreciable stiffening with loading, whereas intact samples tend to remain at a fairly constant ratio. Beyond 60% of peak stress, fractured E_V stiffens to a similar E_{ST} as the intact sample set, whereas fractured E_h exhibits several times lower E_{ST} and E_{DYN} than the intact set. Although both the intact and fractured sample sets were tested at 0.69 MPa confining stress, pre-existing fractures significantly decrease stiffness E_{ST} and E_{DYN} during deviatoric loading, and impact sample failure behavior (Figure 5-3).

Dynamic-static transforms of Poisson's ratios in Figure 5-4 show appreciable differences between the intact and fractured sample sets. At low deviatoric stresses, fractured static ν_{12} and ν_{31} are lower, and ν_{13} is much higher than the intact sample set, likely due to pre-existing fractures facilitating deformation perpendicular to bedding. The ratios of ν_{DYN}/ν_{ST} generally decrease with increasing deviatoric stress; however, the ratio for ν_{13} of the fractured set remains fairly constant throughout the test. Above 40% of peak stress, the intact and fractured ν_{31} tend to parallel each other, whereas dynamic ν_{12} decreases significantly for the fractured set.

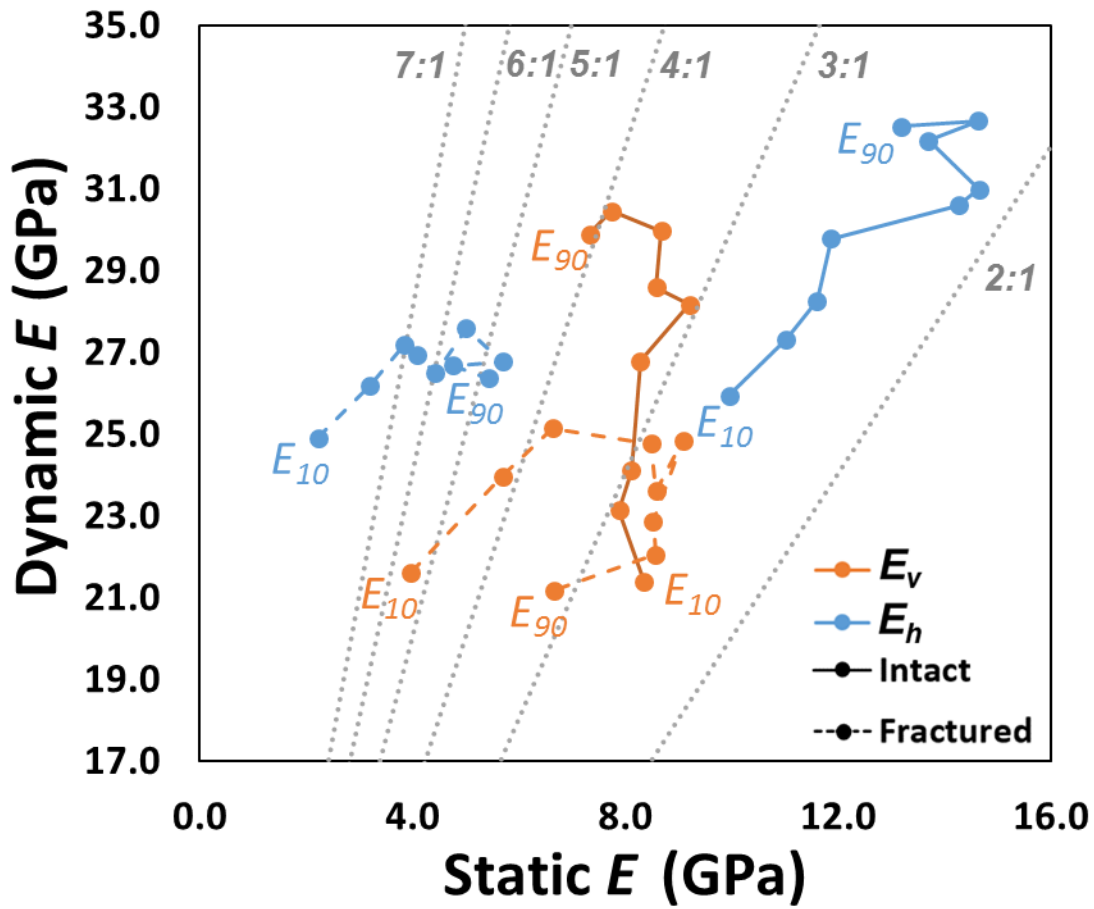


Figure 5-3 Dynamic-static transforms for Young’s moduli E_v (orange) and E_h (blue) for fractured (short dash) and intact (solid) samples both tested at 0.69 MPa confining stress. Each line is marked with E_{10} and E_{90} to denote the starting and ending points of the test (10% and 90% of peak stress), respectively, whereas thin gray lines are marked with their slope as reference for dynamic to static ratios.

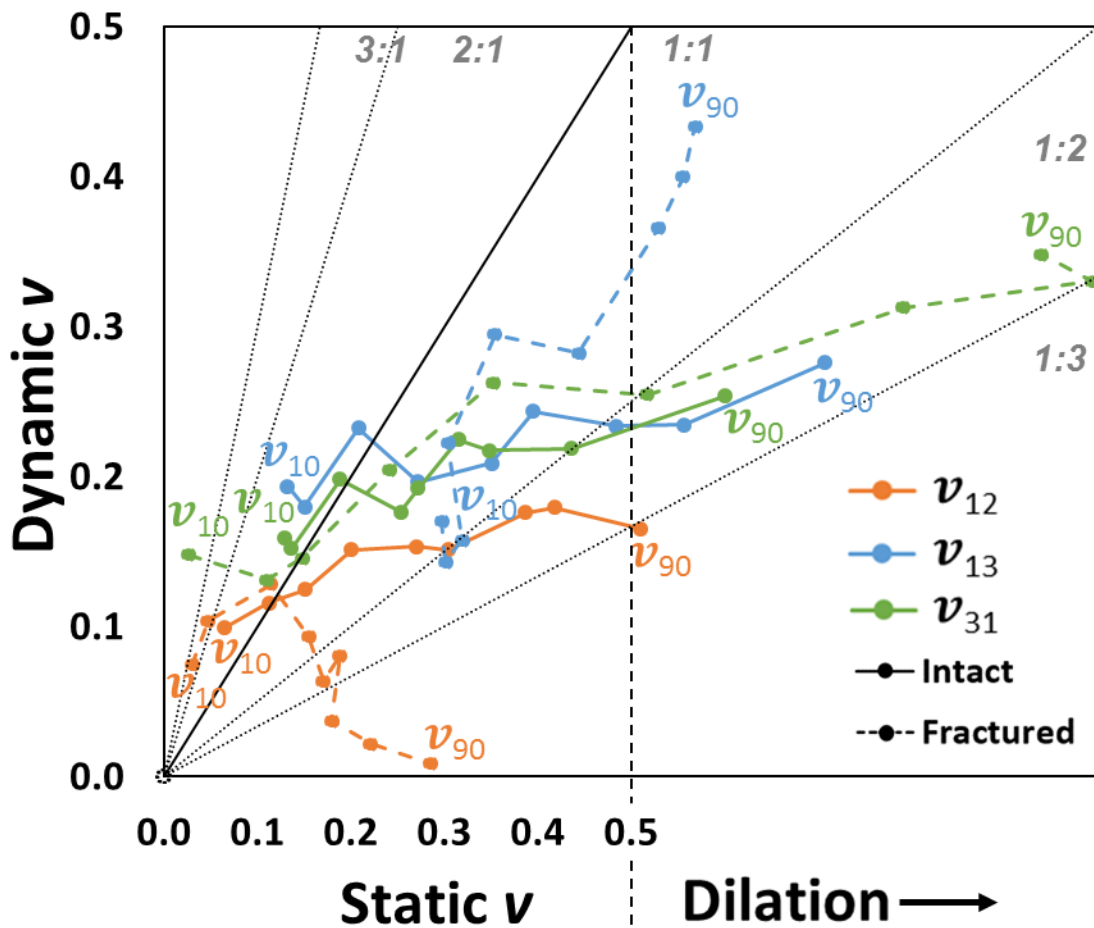


Figure 5-4 Dynamic-static transforms for Poisson's ratios v_{12} (orange), v_{13} (blue), and v_{31} (green) for fractured (short dash) and intact (solid) samples both tested at 0.69 MPa confining stress. Each line is marked with v_{10} and v_{90} to denote the starting and ending points of the test (10% and 90% of peak stress), respectively, whereas thin gray lines are marked with their slope as reference for dynamic to static ratios. The vertical dashed line at 0.5 indicates the transition to dilatant behavior.

5.4 DISCUSSION

5.4.1 Effect of Plastic Strains and Stress-Induced Damage on Dynamic-Static Transforms

Measurements indicate that dynamic-static transforms are impacted by deviatoric stress-induced plastic strains and damage. As expected, damaged rocks exhibit a stronger dependence on confining stress than intact rocks (Figure 5-2). The ratio of E_{DYN}/E_{ST} provides evidence for damage, where increasing ratios indicate (loading) strain-softening and the development of stress-induced fractures. Coalescence of stress-induced microfractures increases mechanical compliance, a response evident in large-strain static measurements. However, fractures commonly localize preferentially to bedding, leaving portions of rock relatively intact, which may provide a path for wave propagation through the sample (Figure 5-5). Therefore, small-strain dynamic measurements are not appreciably impacted (Ass'ad et al. 1992). Additionally, the effects of damage may be hindered due to the use of 3 plugs to make dynamic moduli calculations, and calculations requiring P -wave velocities, which are less affected by stressed fractures (Brie et al. 1998). Static moduli on the other hand, are derived from measurements on a single plug, making them heavily impacted by plug heterogeneity.

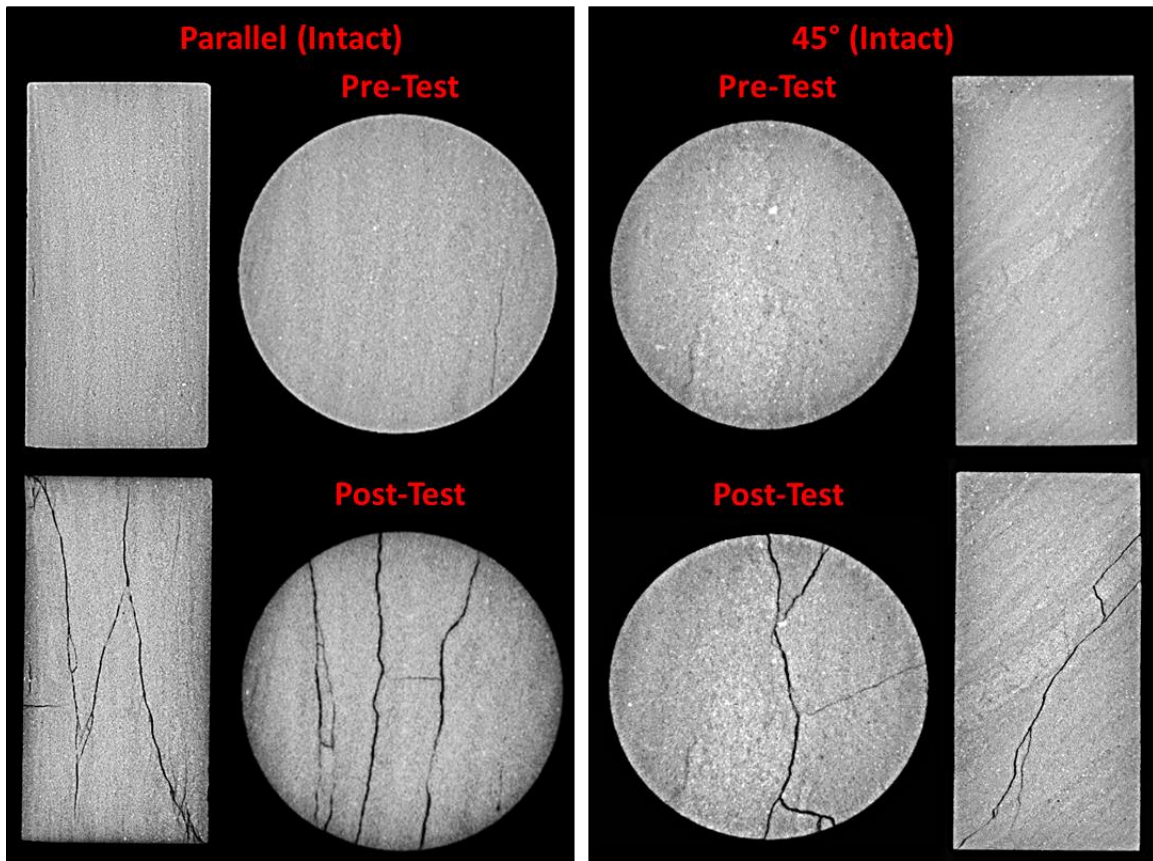


Figure 5-5 X-ray microtomography images of intact plugs parallel (left) and at 45° (right) to bedding. Pre-test slices taken through the center of the sample highlight the bedding orientation (top) while post-test slices at the same point highlight the orientation of stress-induced fracturing. Cores are 1 in diameter by 2 in length.

Increasing deviatoric and confining stresses appear to decrease the anisotropic radial deformation of parallel-to-bedding samples. In these samples, radial expansion is favorable in the direction perpendicular to bedding at low confining stress. As a result, bedding-parallel fractures develop along lamination planes (Figure 5-5). Static Poisson's ratios are a measure of several coincident phenomena, where compliance of endcap-sample interfaces and plastic strains cause low ν_{ST} , and dilation increases ν_{ST} . Therefore, ν_{ST}

exhibits large variability and these phenomena must be decoupled in order to better understand their individual impacts on the static response. Comparison between loading and unloading v_{ST} verify the impact of endcap-sample compliance at low deviatoric stresses (unloading results not shown in Figure 5-4).

5.4.2 Effects of Pre-Existing Fractures on Dynamic-Static Transforms

Pre-existing fractures increase sample compliance and facilitate rock failure. Fractured samples exhibit preferential alignment of failure planes along pre-existing fractures (Figure 5-6). Bedding and pre-existing fractures tend to dictate the location and alignment of new failure planes (Suarez-Rivera et al. 2013). Upon loading and fracture closure, rock stiffness increases, evidenced by the decreasing ratio of E_{DYN}/E_{ST} from 9:1-5:1 for E_h , and 6:1-3:1 for E_v . Similar to Case 1, the relatively high dynamic-static ratios are characteristic of damaged rock. Steady fracture opening during deviatoric loading causes static v_{13} to start and remain around 0.3 until roughly 50% of peak stress, whereas the intact v_{13} starts at 0.1 and does not reach 0.3 until roughly 40-50% of peak stress. By contrast, fracture closure in cores loaded perpendicular to bedding causes lower static v_{31} at low deviatoric stresses. Fracture compliance is also evident when comparing loading and unloading v_{ST} (unloading results not shown in Figure 5-4). Dynamic v_{12} appears to be impacted by the relative timing of stress-induced plastic strains and damage between samples within the fractured set, where the large differences between the orientation and abundance of damage may be causing V_{P45} to approach V_{P11} , thus keeping v_{12} low.

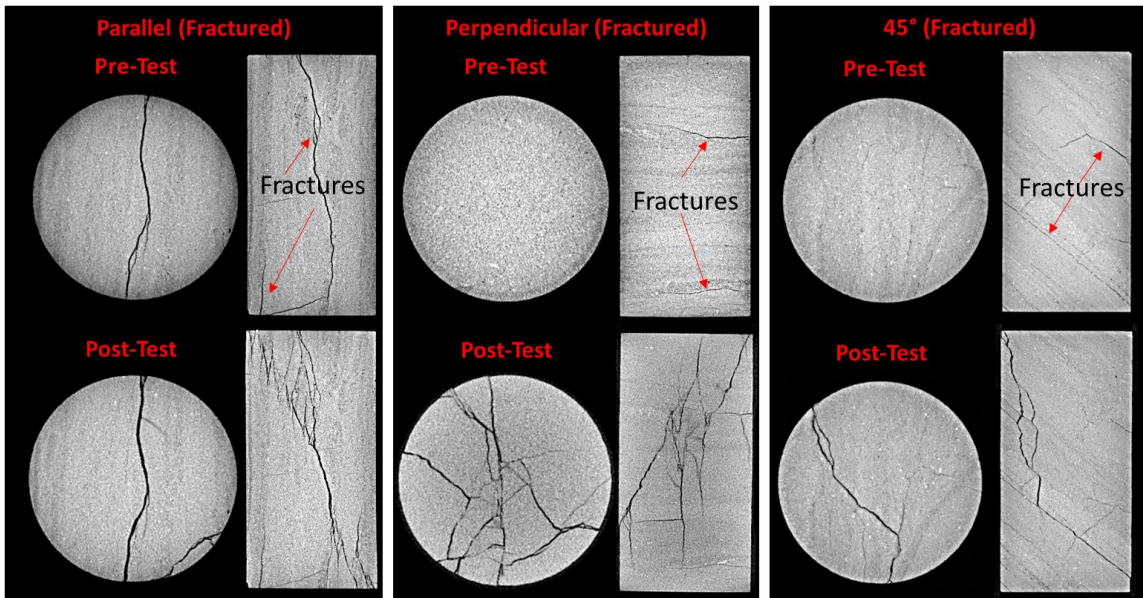


Figure 5-6 X-ray microtomography images of plugs with pre-existing fractures taken parallel (left), perpendicular (middle) and at 45° (right) to bedding. Pre-test slices taken through the center of the sample highlight the pre-existing fracture and bedding orientation (top) while post-test slices at the same point highlight the orientation of stress-induced fracturing. Arrows and annotation show locations of major pre-existing fractures. Cores are 1 in diameter by 2 in length.

The visible branching of stress-induced fractures from pre-existing fractures evidences the complex orientation-specific stress state that develops along pre-existing fractures (Germanovich and Astakhov 2004). The stress state dictates whether a pre-existing fracture provides a path of least resistance through the rock during failure. If not, new fractures branch out to complete the failure plane (Warpinski and Teufel 1987, Shen et al. 1995). Although elasticity may be appropriate for modeling fractured rocks far from failure, a discrete-fracture-network model might be necessary to describe the linkages between pre-existing and stress-induced fractures. Alternatively, an equivalent elastoplastic model may be needed to model bulk strains and stresses.

5.4.3 Accurate Horizontal Stress Determination

Determination of stress-dependent dynamic-static transforms facilitates several applications including decreasing the uncertainty associated with in-situ stress estimation, and identification of fractured rock intervals. Small-scale variations of in-situ effective horizontal stresses σ_{xx} and σ_{yy} can be computed through application of dynamic-static transforms of Young's moduli and Poisson's ratio to sonic logs. A linear-elastic approach for orthorhombic media yields (Far et al. 2016):

$$\sigma_{yy} = \frac{E_y}{E_z} \left(\frac{\nu_{yz} + \nu_{xz}\nu_{xy}}{1 - \nu_{xy}^2} \right) \sigma_z + \frac{E_y}{1 - \nu_{xy}^2} \varepsilon_y + \frac{E_y \nu_{xy}}{1 - \nu_{xy}^2} \varepsilon_x , \quad (38)$$

$$\sigma_{xx} = \frac{E_x}{E_z} \left(\frac{\nu_{xz} + \nu_{yz}\nu_{xy}}{1 - \nu_{xy}^2} \right) \sigma_z + \frac{E_x \nu_{xy}}{1 - \nu_{xy}^2} \varepsilon_y + \frac{E_x}{1 - \nu_{xy}^2} \varepsilon_x , \quad (39)$$

where ε_x and ε_y are the lateral strains, E_x , E_y , and E_z are directional Young's moduli, and ν_{xy} , ν_{xz} , and ν_{yz} are directional Poisson's ratios (Biot coefficient neglected for simplicity). Industry practice typically uses Young's modulus and Poisson's ratio determined at 50% of peak stress from several plugs (ATSM 2014). Experimental results show, however, that rock properties depend on confining stress, deviatoric stress, laminations, presence of fractures, and strain magnitude. Therefore, better constraints of in-situ stress require either an appropriate range of anisotropic Young's moduli and Poisson's ratios, or a more advanced constitutive model to link strain and stresses.

5.5 CONCLUSIONS

Our study documents the influence of confining stress, deviatoric stress and induced damage, and pre-existing fractures on the static-dynamic transforms of Mancos Shale. Using the 3-plug method, layering induced anisotropy is properly accounted for with anisotropic Young's moduli and Poisson's ratios idealized in a TI medium.

Results show high ratios of dynamic-static Young's moduli likely correspond to rock damage, where rocks with pre-existing fractures range between 7:1 and 5:1, compared to 3:1 for intact samples. Ratios increase due to plastic strains incurred as samples approach failure.

X-ray microtomography images highlight the impact of layering and pre-existing fractures on stress-induced fracturing and rock failure. Pre- and post-test images show layering-induced mechanical stratigraphy, layer interfaces and pre-existing fractures acting as planes of weakness, and fracture orientation changing when passing through different lithologies.

Overall, results emphasize the complex dynamic and quasi-static deformational behavior of anisotropic fractured shales. The variability of stiffness coefficients indicate that linear elasticity may be insufficient to model large strain mechanical behavior and, therefore, to calculate in-situ stresses.

5.6 SUPPORTING INFORMATION

Table 5-1 Mancos Shale sample ID, bedding orientation, bulk mass density ρ , effective confining stress, and effective axial peak stress at failure.

Mancos Shale Sample ID	Bedding Orientation	Bulk mass density ρ (g/cm ³)	Effective confining (radial) stress σ_3 (MPa)	Effective axial peak stress σ_1 (MPa)
PD-1	0°	2.53	0.69	73.82
PD-15-F	0°	2.50	0.69	70.40
PD-2	0°	2.52	3.45	104.21
PD-6	0°	2.53	6.9	97.32
PD-17	0°	2.53	20.7	159.13
PL-5	90°	2.53	0.69	82.06
PL-7-F	90°	2.51	0.69	27.49
PL-6	90°	2.54	3.45	88.39
PL-3	90°	2.55	6.9	93.37
PL-15	90°	2.53	20.7	187.54
45-1	45°	2.54	0.69	56.67
45-5-F	45°	2.52	0.69	34.64
45-6	45°	2.53	3.45	69.20
45-8	45°	2.53	6.9	89.55
45-12	45°	2.53	20.7	146.86

Table 5-2 Intact Mancos Shale sample dynamic and static Young's moduli E and Poisson's ratios ν as a function of the % of peak stress during deviatoric loading under 0.69 MPa confining stress.

0.69 MPa Confining Stress (Intact)										
% of Peak Stress	Dynamic Young's Moduli (GPa) and Poisson's ratios					Static Young's Moduli (GPa) and Poisson's ratios				
	E_{vDyn}	E_{hDyn}	ν_{12Dyn}	ν_{13Dyn}	ν_{31Dyn}	E_{vSt}	E_{hSt}	ν_{12St}	ν_{13St}	ν_{31St}
10	21.39	25.94	0.099	0.193	0.16	8.36	9.95	0.064	0.132	0.130
20	23.13	27.31	0.116	0.180	0.15	7.88	11.02	0.113	0.151	0.137
30	24.10	28.26	0.125	0.233	0.20	8.11	11.61	0.151	0.208	0.189
40	26.78	29.78	0.151	0.196	0.18	8.28	11.87	0.200	0.272	0.254
50	28.16	30.59	0.154	0.209	0.19	9.21	14.26	0.271	0.351	0.272
60	28.59	30.98	0.151	0.244	0.22	8.58	14.65	0.304	0.396	0.315
70	29.97	32.17	0.176	0.234	0.22	8.67	13.70	0.387	0.484	0.348
80	30.45	32.66	0.180	0.235	0.22	7.74	14.63	0.418	0.557	0.437
90	29.89	32.53	0.165	0.276	0.25	7.33	13.18	0.510	0.708	0.600

Table 5-3 Fractured Mancos Shale sample dynamic and static Young's moduli E and Poisson's ratios ν as a function of the % of peak stress during deviatoric loading under 0.69 MPa confining stress.

0.69 MPa Confining Stress (Pre-existing Fractures)										
% of Peak Stress	Dynamic Young's Moduli (GPa) and Poisson's ratios					Static Young's Moduli (GPa) and Poisson's ratios				
	E_{vDyn}	E_{hDyn}	ν_{12Dyn}	ν_{13Dyn}	ν_{31Dyn}	E_{vSt}	E_{hSt}	ν_{12St}	ν_{13St}	ν_{31St}
10	21.61	24.90	0.075	0.171	0.15	3.97	2.22	0.030	0.298	0.027
20	23.97	26.19	0.104	0.143	0.13	5.69	3.20	0.047	0.302	0.111
30	25.15	27.19	0.128	0.158	0.15	6.63	3.85	0.115	0.319	0.148
40	24.76	26.93	0.094	0.222	0.20	8.48	4.09	0.155	0.304	0.241
50	23.60	26.48	0.064	0.295	0.26	8.58	4.43	0.170	0.354	0.353
60	24.84	27.58	0.081	0.282	0.25	9.08	5.01	0.189	0.444	0.517
70	22.86	26.76	0.037	0.366	0.31	8.52	5.69	0.179	0.530	0.791
80	22.05	26.68	0.022	0.400	0.33	8.57	4.77	0.222	0.556	0.993
90	21.17	26.36	0.009	0.433	0.35	6.67	5.43	0.286	0.569	0.939

Table 5-4 Intact Mancos Shale sample dynamic and static Young's moduli E and Poisson's ratios ν as a function of the % of peak stress during deviatoric loading under 3.45 MPa confining stress.

3.45 MPa Confining Stress (Intact)										
% of Peak Stress	Dynamic Young's Moduli (GPa) and Poisson's ratios					Static Young's Moduli (GPa) and Poisson's ratios				
	E_{vDyn}	E_{hDyn}	ν_{12Dyn}	ν_{13Dyn}	ν_{31Dyn}	E_{vst}	E_{hst}	ν_{12st}	ν_{13st}	ν_{31st}
10	20.16	28.87	0.167	0.255	0.18	8.03	9.63	0.119	0.136	0.017
20	20.51	29.43	0.138	0.356	0.25	8.58	10.28	0.243	0.219	0.108
30	21.90	30.69	0.154	0.351	0.25	8.77	12.13	0.248	0.260	0.149
40	25.36	32.45	0.199	0.282	0.22	9.04	13.81	0.324	0.336	0.147
50	25.85	33.00	0.203	0.300	0.24	9.30	16.25	0.332	0.401	0.167
60	27.85	34.18	0.225	0.272	0.22	9.79	16.38	0.389	0.450	0.346
70	29.67	34.76	0.237	0.250	0.21	9.08	15.97	0.429	0.509	0.382
80	31.06	35.27	0.243	0.245	0.22	8.74	16.57	0.472	0.599	0.464
90	32.06	36.09	0.255	0.236	0.21	6.12	14.84	0.620	0.712	0.550

Table 5-5 Intact Mancos Shale sample dynamic and static Young's moduli E and Poisson's ratios ν as a function of the % of peak stress during deviatoric loading under 6.9 MPa confining stress.

6.9 MPa Confining Stress (Intact)										
% of Peak Stress	Dynamic Young's Moduli (GPa) and Poisson's ratios					Static Young's Moduli (GPa) and Poisson's ratios				
	E_{vDyn}	E_{hDyn}	ν_{12Dyn}	ν_{13Dyn}	ν_{31Dyn}	E_{vst}	E_{hst}	ν_{12st}	ν_{13st}	ν_{31st}
10	23.11	31.12	0.192	0.149	0.11	8.43	11.30	0.104	0.038	0.192
20	26.22	33.58	0.247	0.127	0.10	8.91	12.36	0.154	0.096	0.172
30	28.60	35.05	0.273	0.119	0.10	8.77	12.61	0.192	0.164	0.173
40	30.50	36.11	0.278	0.146	0.12	8.38	13.73	0.185	0.236	0.229
50	32.08	37.28	0.302	0.133	0.11	8.18	14.00	0.263	0.282	0.261
60	33.67	38.05	0.312	0.133	0.12	8.30	12.55	0.290	0.333	0.344
70	33.71	38.51	0.310	0.153	0.13	8.04	12.32	0.352	0.443	0.416
80	33.88	38.89	0.310	0.178	0.16	7.16	11.52	0.431	0.544	0.501
90	34.29	39.10	0.310	0.187	0.16	6.35	10.23	0.522	0.688	0.660

6. Quantifying Static and Dynamic Stiffness Anisotropy and Nonlinearity in Finely Laminated Shales: Experimental Measurement and Modeling

Matthew J. Ramos, D. Nicolas Espinoza, Stephen E. Laubach, and Carlos Torres-Verdín

6.1 CHAPTER ABSTRACT

Sedimentary rocks contain layers and a wide range of microstructures that may produce mechanical complexities including dynamic and quasi-static stiffness anisotropy and nonlinearity. However, most applications in geophysics and geomechanics disregard these mechanical complexities, which can lead to significant error and uncertainty in rock properties, and may increase the risk associated with cost-intensive drilling and completions operations in shales. We conduct simultaneous triaxial stress tests and ultrasonic wave propagation monitoring to measure and model stiffness anisotropy and nonlinearity of Mancos Shale plugs with varying bedding orientations. Results highlight the need for different sets of nonlinear coefficients to describe different stress loading paths, where isotropic loading exhibits larger increases in stiffness for a given change in mean stress (and strain) than deviatoric loading. The vertical-transverse-isotropic (VTI) nonlinear model helps to account for the appreciable anisotropy and nonlinearity of Mancos samples, where dynamic Young's moduli E_h are more than 25% higher than E_v , and E_h increases by roughly 35% during deviatoric stress loading. Measured static moduli are typically less than 50% of their dynamic equivalent and exhibit separate anisotropic and nonlinear relationships. Therefore, we developed anisotropic stress-dependent dynamic-static transforms to estimate static moduli from the nonlinear VTI model.

Although heterogeneity and discontinuities cause samples to deviate from VTI symmetry, our modified dynamic-static transforms provide an excellent fit to the experimentally measured Young's Moduli and Poisson's ratios. Post-test X-ray MicroCT imaging evidences the impact of sample layering and heterogeneity on rock failure and failure geometry. Bedding planes can act as preferential failure planes, whereas layering-induced mechanical stratigraphy can cause fractures to reorient due to changes in lithology. Our combined experimental, modeling, and imaging results provide insight into the complex deformational and failure behavior of shales. The analysis and results also highlight the need to consider both elastic and plastic deformations in shales.

6.2 INTRODUCTION

Most rocks exhibit elastic nonlinearity, i.e., the relationship between stress and strain deviates from Hooke's law and rock stiffness changes with applied stress. Nonlinearity is controlled by the mechanical compliance of grain contacts and microstructural defects such as fractures (Gueguen and Palciauskas 1994, Jaeger et al. 2009, Mavko et al. 2009). When subjected to an applied stress, these features deform more easily than the intact rock matrix, affecting the overall rock stiffness (Anders et al. 2014). Upon closure of such compliant features, contact area between matrix material (i.e. grains and cement) increases, and the overall rock mass exhibits an increase in stiffness (Walsh 1965, Batzle et al. 1980, Fortin et al. 2007, Guyer and Johnson 2009). The impact that compliant features have on stiffness relates heavily to the rock type and their orientation with respect to stress orientations and stress loading path (Lo et al. 1986, Eberhart-Phillips

et al. 1989, Schwartz et al. 1994). Elastic nonlinearity has been documented at several length scales and can be measured through static and dynamic methods (Nur and Simmons 1969, Mavko et al. 1995, Dillen et al. 1999, Scott and Abousleiman 2005, Fjaer 2009). For example, when subjected to anisotropic stresses, elastic nonlinearity causes an otherwise isotropic rock to exhibit anisotropic mechanical properties, where rock stiffness is higher in the direction of maximum stress (Sinha and Kostek, 1996, Johnson and Rasolofosaon 1996, Winkler 1996, Sayers 2002, Fang et al. 2013). Field-scale seismic and wellbore sonic studies support laboratory observations and show that (a) stiffness increases with increasing effective stress, and (b) anisotropic tectonic stresses can induce compressional and shear-wave anisotropy (Winkler et al. 1998, Sinha and Winkler 1999, Sarkar et al. 2003, Herwanger and Horne 2009, Lei et al. 2012, Fang et al. 2013, Collet et al. 2014). Although both static and dynamic rock properties exhibit nonlinear stiffness, the relationship between stiffness and stress often differs between the two measurement techniques (Simmons and Brace 1965, Cheng and Johnston 1981, Fjaer 2009, Ramos et al. 2017). Understanding these differing stress dependences is important for developing dynamic-static transforms, which use dynamic measurements to accurately characterize quasi-static rock mechanical properties and inferred variability of in-situ horizontal stresses (Pena 1999, Sone and Zoback 2013).

Elastic nonlinearity is well-described for isotropic materials subjected to isotropic and uniaxial stress loading, where third-order stiffness coefficients help to describe the complex stress-strain behavior (Thurston and Brugger 1964, Johnson and Rasolofosaon 1996, Sinha and Kostek 1996, Winkler and Liu 1996, Gurevich et al. 2011). However,

subsurface stresses are not isotropic, and most rocks exhibit some degree of anisotropy, whether it be intrinsic, stress-induced, or both (Nur 1971, Lo et al. 1986, Rasolofosaon 1998, Sarkar et al. 2003, Zoback 2007). Therefore, wellbore and field scale measurements often require interpretation of wave propagation through effectively anisotropic layered media to estimate rock properties and stresses (Sinha and Kostek 1996, Donald et al. 2013; 2015, Collet et al. 2014, Melendez-Martinez and Schmitt 2016). To address these limitations, a few studies have applied nonlinear elastic theory to describe wave propagation through anisotropic rocks (Jakobsen and Johansen 2000, Prioul et al. 2001; 2004, Donald and Prioul 2015). The modified theory is useful for describing anisotropic dynamic nonlinearity. However, nonlinearity of static properties is rarely quantified due to the complexities associated with measuring the appropriate number of independent static strains to describe anisotropic rocks (Sarkar et al. 2003). Furthermore, static and dynamic measurements have different stress dependences, which makes estimating static stiffness coefficients from nonlinear dynamic measurements nontrivial (McCall and Guyer 1994, Pena 1999, Fjaer 2009, Sone and Zoback 2013, Ramos et al. 2017).

We address the aforementioned limitations in an effort to accurately measure and model the nonlinearity of static and dynamic stiffness of anisotropic rocks. Triaxial stress testing and simultaneous ultrasonic monitoring are used to measure changes in static and dynamic rock mechanical properties as a function of applied isotropic and deviatoric stress. Measurements are carried out in finely laminated Cretaceous Mancos Shale samples at varying bedding orientations to properly quantify rock stiffness parameters and develop dynamic-static transforms. We estimate third-order nonlinear stiffness terms from

experimentally determined dynamic stiffness coefficients during isotropic loading. The utility of the isotropically derived parameters for describing stiffness nonlinearity during deviatoric loading is tested, and we provide new parameters that better fit the experimental data. Nonlinear stiffness coefficients are utilized to estimate the stress dependence of dynamic bulk moduli, Young's moduli, and Poisson's ratios. Experimentally determined ratios of static-to-dynamic moduli are applied to modeled nonlinear dynamic moduli in order to calculate their nonlinear static equivalent. We discuss the potential limitations for applying the nonlinear model, the impact of rock layering and heterogeneity on our measurements, and potential field implications of the study.

6.3 RESULTS AND ANALYSIS

6.3.1 Strain Response to Isotropic and Deviatoric Loading

Figure 6-1 A shows the relationships between mean stress and volumetric strain for the three oriented samples subjected to isotropic loading up to 82.7 MPa, then subsequent unloading to 20.7 MPa. During early loading, all three samples exhibit similar stress-strain behavior, which is fairly linear up to roughly 20 MPa. Above 20 MPa samples show nonlinear responses, where stiffness increases with stress. The nonlinear stiffening is slightly more dominant in the 0° and 90° plugs. During the unloading phase, the slopes of the three curves appear similar, and are much steeper than the loading phase. The instantaneous change in slope between loading and unloading is common and often

attributed to the loading curve being a measure of elastic and plastic strains, whereas unloading curves represent an almost purely elastic response (Fjaer 2009).

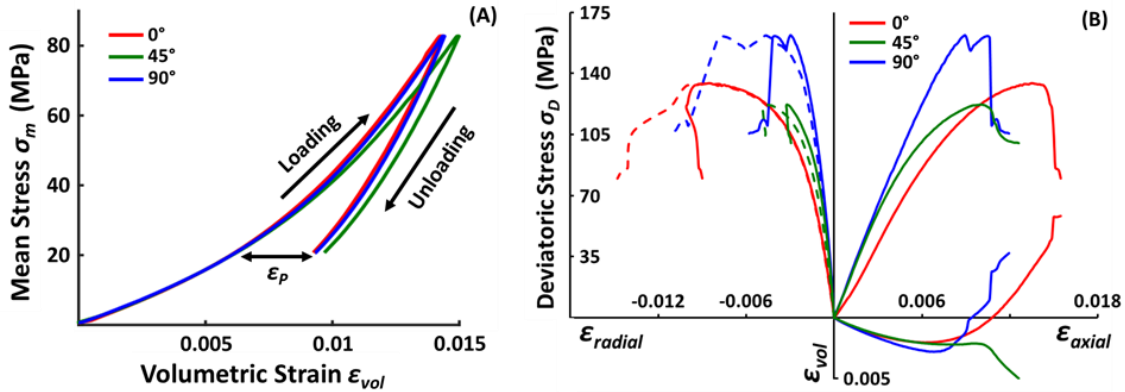


Figure 6-1 (A) Volumetric strain curves during isotropic loading up to 82.7 MPa mean stress, then subsequent unloading to 20.7 MPa mean stress. Arrows point in the direction of increasing time during the loading and unloading cycles and ϵ_p represents the plastic strains incurred during loading, and (B) axial, radial, and volumetric strain curves during deviatoric loading to failure, for 0° (red), 45° (green), and 90° (blue) samples. Radial strains (two independent measurements) are perpendicular (dashed) and parallel (solid) to bedding for the 45° and 90° samples.

After the isotropic cycle, the same three oriented plugs were loaded axially to failure at a constant confining stress of 20.7 MPa. Figure 6-1-B shows the relationships between deviatoric stress and measured axial, radial, and volumetric strains during this phase of testing. During early deviatoric loading the 0° sample exhibits slightly larger strains than the 90° and 45° samples. All three deviatoric loading curves appear fairly linear up to 70 MPa. Above 70 MPa the three sample's axial and radial strain curves deviate from each other. The 0° plug exhibits the largest values of radial and axial strain, whereas the 45° plug shows relatively little radial strain and comparable axial strain to the 0° sample. The volumetric strain curves indicate that the 0° and 90° plugs began to dilate at roughly

65% and 85% of peak stress, whereas the 45° sample failed almost immediately after dilation began. Radial strain anisotropy is also visible in Figure 6-1-B midway through their respective loading cycles, the 45° and 90° samples both exhibit higher radial strain in the direction perpendicular to bedding, which increases after failure. The 0° plug only exhibits asymmetric radial strain after failure. The 45° sample exhibited the lowest peak stress (126.6 MPa), followed by the 0° (138.7 MPa) and the 90° (166.9 MPa) samples. Strength anisotropy between plugs and azimuthal strain anisotropy within each sample further evidence the impact of layering orientation on sample mechanical behavior.

6.3.2 Nonlinear Dynamic and Static Stiffness during Isotropic Loading

Figure 6-2 shows the experimentally determined dynamic stiffness coefficients during isotropic stress loading. The data exhibit fairly linear stiffening up to a distinct change in slope close to 41 MPa, followed by another roughly linear increase in stiffness until the end of isotropic loading (82.7 MPa). The observed change in dynamic behavior occurs very close to the point at which the volumetric strain curves of the three oriented samples become increasingly nonlinear and depart from each other. This distinct change in both the dynamic and static behavior are likely due to increasing plastic strains being incurred by the sample. Therefore, we limit our application of the nonlinear-elastic model to the first half of isotropic loading (up to 41.3 MPa).

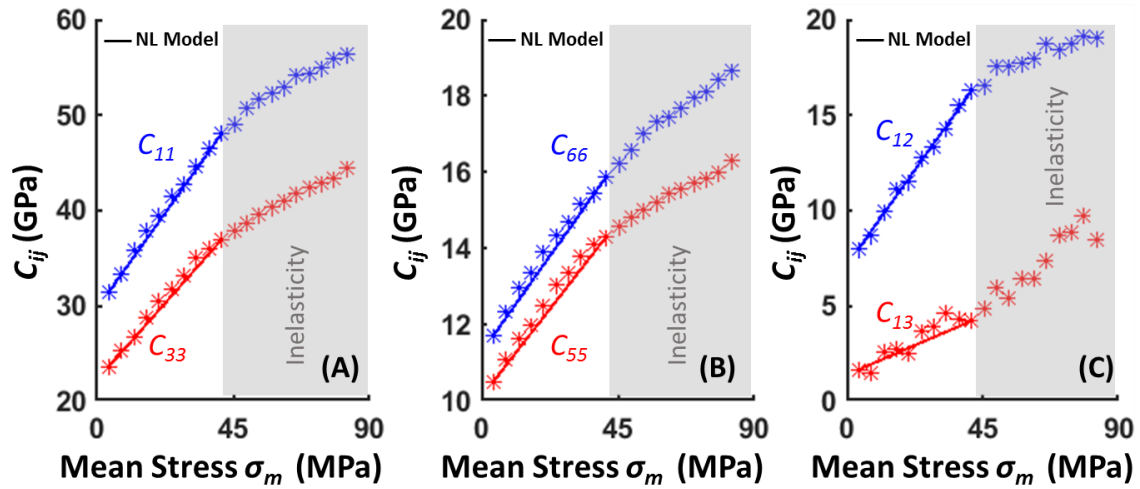


Figure 6-2 Dynamic stiffness coefficients (A) C_{11} and C_{33} , (B) C_{55} and C_{66} , and (C) C_{12} and C_{13} as a function of mean stress. Stars describe experimental data while lines represent modeled stiffness using the nonlinear parameters of Table 6-1.

The stress dependence of stiffness during isotropic loading was modeled using the quasi-static strains from the respective test and dynamic stiffness terms c_{ij}^0 at a reference mean stress of 4.13 MPa. The stiffness terms were then estimated for a mean stress of 41.3 MPa using the change in strain associated with the change of stress. The associated strain changes were input into Equations 5-11 and a least squares method was used to determine the nonlinear coefficients which best fit the observed changes in dynamic stiffness coefficients with increasing mean stress. After fitting to the data, only seven of the original seventeen third-order nonlinear c_{ijk} terms remained non-zero. Their values are presented in Table 6-1 and fit the data very well for the isotropic loading cycle (Figure 6-2).

Table 6-1 Third-order nonlinear stiffness coefficients C_{111} , C_{333} , C_{112} , C_{133} , C_{144} , C_{255} , and C_{366} for the isotropic and deviatoric stress loading cycles.

Test Type	Stress Interval	C_{111} (GPa)	C_{333} (GPa)	C_{112} (GPa)	C_{133} (GPa)	C_{144} (GPa)	C_{255} (GPa)	C_{366} (GPa)
Isotropic	4.1 - 41.3 MPa	3356	4874	3620	880	1476	1074	1177
Deviatoric	5 - 60 % of Peak	2988	1151	1913	159	-705	-621	-1302

Figure 6-3 compares the experimentally determined static and dynamic bulk moduli to those moduli estimated from the nonlinear model during the elastic portion of isotropic loading (Equations 27 and 31). The model predicts dynamic bulk modulus very well, with a slight over-prediction at lower mean stresses. Two methods were used to estimate the static bulk moduli from those calculated using the nonlinear dynamic model. The first method used an average of the ratios of dynamic to static bulk moduli during the elastic portion of isotropic loading ($K_{st} = 0.285K_{dyn}$). The second method utilized a linear equation describing the change in the ratios of dynamic to static bulk moduli as a function of mean stress ($K_{st} = 0.215 + 3.08 \times 10^{-3} \sigma_m$). Ratios of dynamic to static bulk moduli can be found in Table 6-2. Both methods were applied to the modeled dynamic bulk moduli to predict the static bulk moduli as a function of mean stress (Figure 6-3). The average value provides a good fit to the central portion of the experimental data, but over and under predicts at the beginning and end of isotropic loading, respectively. On the other hand, the linear expression provides an almost perfect match with the experimental data. The estimated

static bulk moduli actually provide a better fit to the experimental data than the modeled dynamic moduli from which they were derived.

Table 6-2 Ratios of static-to-dynamic E_h , E_v , ν_{12} , ν_{13} , and ν_{31} as a function of % of peak stress during deviatoric loading (orange), and K as a function of mean stress during isotropic loading (green). Average values used for computing static moduli are shown in the bottom row (yellow).

Deviatoric	Ratios Between Static-to-dynamic					Isotropic	
% of Peak Stress	E_h	E_v	ν_{12}	ν_{13}	ν_{31}	K	Mean Stress (MPa)
5	0.451	0.342	0.561	1.441	1.607	0.242	4.14
10	0.552	0.390	0.601	1.868	1.904	0.243	8.27
15	0.487	0.399	0.659	1.839	2.296	0.246	12.41
20	0.441	0.397	0.620	2.009	2.752	0.254	16.55
25	0.453	0.388	0.721	2.323	3.024	0.278	20.68
30	0.438	0.453	0.788	2.388	3.302	0.287	24.82
35	0.431	0.446	0.761	2.453	3.432	0.306	28.96
40	0.387	0.380	0.774	2.514	3.304	0.314	33.09
45	0.338	0.351	0.684	2.443	3.411	0.332	37.23
50	0.353	0.374	0.773	2.860	4.087	0.352	41.37
55	0.349	0.345	0.793	3.045	4.733		
60	0.300	0.322	0.739	3.191	5.377		
Average	0.415	0.382	0.706	2.365	3.269	0.285	

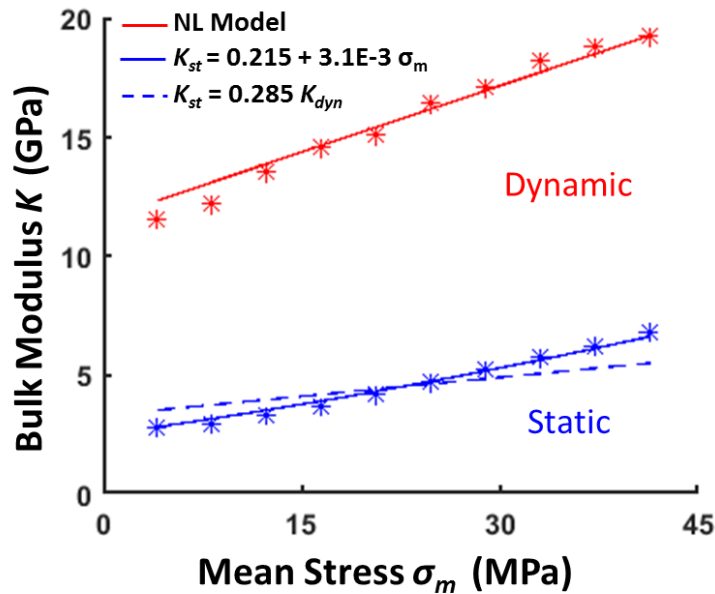


Figure 6-3 Dynamic (red) and static (blue) bulk modulus as a function of mean stress. Static bulk moduli were modeled using both the average ratio of static-to-dynamic. Stars describe experimental data while lines represent modeled stiffness using nonlinear parameters determined from isotropic loading. Static moduli were modeled using an average ratio of static-to-dynamic moduli (dashed blue line) and a linear fit to the static-to-dynamic ratios as a function of stress (solid blue line).

6.3.3 Nonlinear Dynamic and Static Stiffness During Deviatoric Loading

Figure 6-4 shows the stress dependence of dynamic stiffness coefficients during deviatoric stress loading. In general, the stiffness coefficients increase linearly with increasing deviatoric stress up to roughly 60% of peak stress. Beyond 60% of peak stress, stiffness coefficients C_{11} and C_{12} continue to increase, whereas C_{33} , C_{55} and C_{66} tend to plateau, and C_{55} then decreases considerably when approaching peak stress. C_{13} exhibits significantly different behavior than the other coefficients, remaining fairly constant during early loading and appreciably increasing after about 60% of peak stress. The C_{ij} calculated

with the VTI assumption may not be applicable beyond a certain stress limit because of loss of symmetry and plastic strains. For example, C_{13} is calculated from several other stiffness terms, therefore, the increase in C_{13} at 60% of peak stress is likely due to the decreases in C_{33} and C_{55} with increasing plastic deformation. Despite the potential impact of plastic strains, we provide these C_{ij} values as a reference (See discussion section).

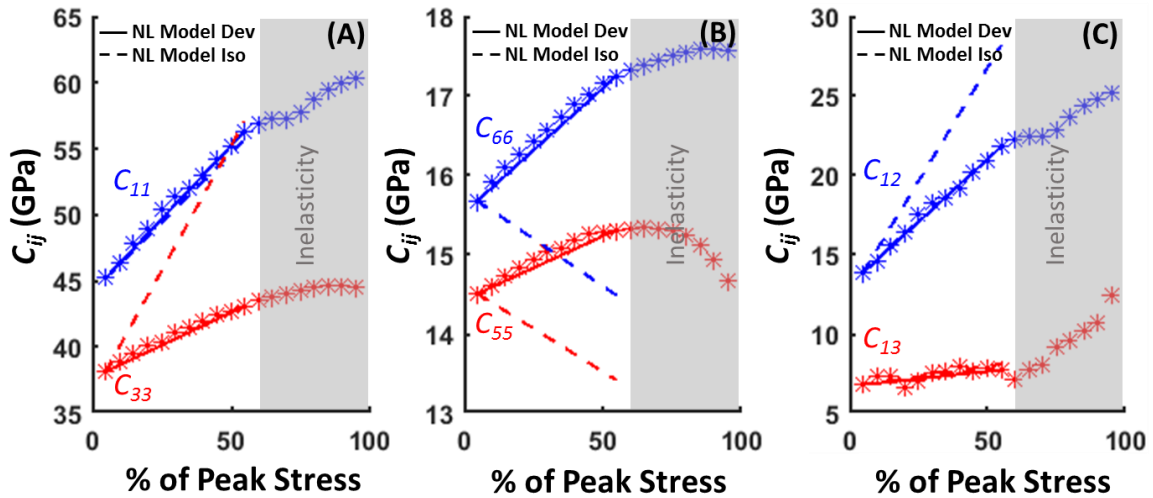


Figure 6-4 Dynamic stiffness coefficients (A) C_{11} and C_{33} , (B) C_{55} and C_{66} , and (C) C_{12} and C_{13} as a function of % of peak stress during deviatoric loading. Stars describe experimental data while lines represent modeled stiffness using nonlinear parameters determined from deviatoric (solid) and isotropic (dashed) loading.

Similar to the isotropic loading cycle, the distinct change in dynamic behavior at roughly 60% likely indicates an increase in plastic strains incurred during deviatoric loading (Winkler and Liu 1996). Therefore, static and dynamic techniques were used in order to more accurately determine the onset of significant plastic strains and thus the limit to which the elastic model could be applied. Sample dilation (inflection of the volumetric strain curve) and changes in shear-wave anisotropy between C_{44} and C_{55} are typical

indicators for appreciable plastic strains and the opening of micro-fractures (Nemat-Nasser and Obata 1988, Rawling et al. 2002, Wassermann et al. 2009, Ramos et al. 2017). Dilation occurred earliest in the 0° plug at 65% of peak stress and changes in shear-wave anisotropy were observed at roughly 60% of peak stress. Therefore, 60% was chosen as the elastic limit for modelling deviatoric loading.

The third-order nonlinear stiffness coefficients determined from the isotropic loading cycle were applied to the deviatoric loading data to determine the model's applicability to other stress loading paths (Figure 6-4). Similar to the isotropic case, changes in stiffness associated with a change in stress were estimated by applying experimentally determined changes in static strain to Equations 5-11. Figure 6-4 shows the inconsistent fit between the measured and modeled stiffness parameters using the isotropically derived third-order nonlinear coefficients. Specifically, the nonlinear parameters fit the C_{11} and C_{13} data, but over-predict C_{33} and C_{12} , and significantly under-predict C_{55} and C_{66} . Therefore, a new set of third-order stiffness coefficients were fit to the data to more accurately describe stiffness nonlinearity during deviatoric loading (Table 6-1). Figure 6-4 shows the improved fit obtained from the new set of parameters, which exhibit very good agreement with all the experimentally determined data.

Figures 6-5 and 6-6 compare the experimentally derived anisotropic static and dynamic Young's moduli E_h and E_v and Poisson's ratios ν_{12} , ν_{13} , and ν_{31} to those moduli calculated from the estimated stiffness coefficients from the nonlinear model (Equations 22-26 and 32-36). The model predicts E_v very well, but slightly-predicts E_h throughout deviatoric loading (Figure 6-5). Similar to the bulk moduli, static Young's moduli (E_v and

E_h) and Poisson's ratios (ν_{12} , ν_{13} , and ν_{31}) were estimated in two ways: first by applying the average ratio of static-to-dynamic moduli to the modeled dynamic moduli, and the second utilized the linear relationships between the static-to-dynamic ratios as a function of the fraction of peak stress (Table 6-2). Both methods provide a good fit with the static E_v data, but the linear fit more accurately describes the E_h data. In general, the experimentally derived anisotropic dynamic Poisson's ratios in Figure 6-6 match very well with the estimates from the nonlinear model. The models accurately predict the increasing dynamic Poisson's ratio ν_{12dyn} and slightly decreasing ν_{13dyn} and ν_{31dyn} with increasing deviatoric stress. The estimated static Poisson's ratios ν_{13st} and ν_{31st} also exhibit a great fit using the linear relationship of static-to-dynamic Poisson's ratios, whereas the average static-to-dynamic ratio provides a decent fit for ν_{12st} but fails to capture the increasing ν_{13st} and ν_{31st} with increasing deviatoric stress. Overall, the excellent fit between the experimental data and the modeled dynamic Young's moduli and Poisson's ratios can be attributed to the nonlinear model's ability to accurately predict all of the dynamic C_{ij} 's, during deviatoric loading. Although the nonlinear model assuming VTI symmetry fits our data well, our experimental results indicate that Mancos Shale is not a perfectly VTI medium. For example, we observe negligible differences between C_{44} and C_{55} (0.4% during isotropic and 0.1% during the modeled portion of deviatoric loading), however, our data do not fulfill the VTI requirement of $\nu_{31}/E_v = \nu_{13}/E_h$. The departure from VTI is likely due to sample heterogeneity and distinct cross-bedding, which cause some layers to deviate from the average 0°, 45°, and 90° orientations of our plugs.

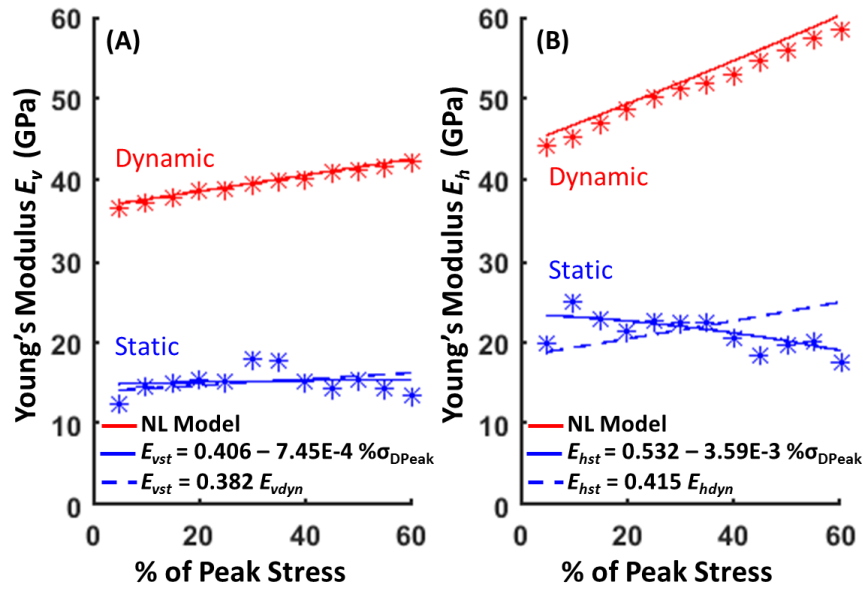


Figure 6-5 Anisotropic dynamic (red) and static (blue) Young's Moduli (A) E_v and (B) E_h as a function of % of peak stress during deviatoric loading. Stars describe experimental data while lines represent modeled stiffness using nonlinear parameters determined from deviatoric loading. Static moduli were modeled using an average ratio of static-to-dynamic moduli (dashed blue line) and a linear fit to the static-to-dynamic ratios as a function of stress (solid blue line).

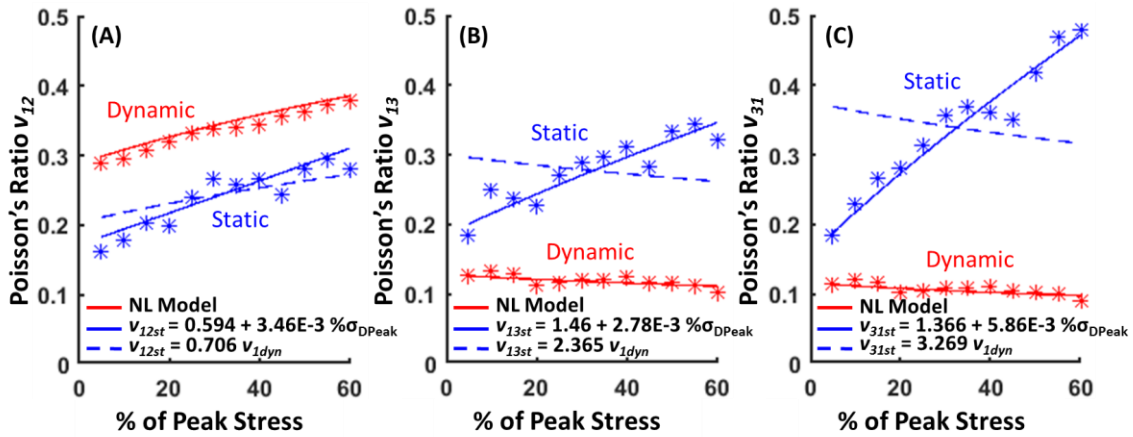


Figure 6-6 Anisotropic dynamic (red) and static (blue) Poisson's Ratios (A) v_{12} and (B) v_{13} and (C) v_{31} as a function of % of peak stress during deviatoric loading. Stars describe experimental data while lines represent modeled Poisson's ratios using nonlinear parameters determined from deviatoric loading. Static moduli were modeled using an average ratio of static-to-dynamic moduli (dashed blue line) and a linear fit to the static-to-dynamic ratios as a function of stress (solid blue line).

6.4 DISCUSSION

6.4.1 Inability of isotropically derived nonlinear coefficients to predict deviatoric nonlinearity

Results highlight the inability of isotropically derived nonlinear third-order stiffness coefficients to accurately model all of the stiffness changes during deviatoric stress loading. The combined effects of intrinsic sample anisotropy, heterogeneity between samples, and stress anisotropy may play a measurable role in this mismatch (Jakobsen and Johansen 2000, Sarkar et al. 2003). For example, during deviatoric loading of 0° samples the radial confining stress acts equally in the plane of symmetry (directions 1 and 2 –Figure 2-2) and is different from the axial stress parallel to the axis of symmetry (3 direction). This testing configuration maintains the VTI assumption. On the other hand, deviatoric loading of a 90° sample (in direction 1) would impose anisotropic stresses in the plane of symmetry. Because rocks samples behave nonlinearly, deviatoric loading along the plane of symmetry will cause the rock to exhibit anisotropic stiffness in the 1 and 2 directions, which may challenge our VTI assumption (Prioul et al. 2004). This is not an important consideration during isotropic loading because all core orientations are subjected to the same stress field. In fact, when we applied a nonlinear model assuming an isotropic third-order stiffness tensor (Prioul et al. 2004), it fit the isotropic stiffnesses fairly well, but provided a poor fit to the stiffnesses during deviatoric loading. Therefore, the addition of stress-induced anisotropy along the symmetry plane is better described by the VTI model we presented, but may be more accurately modeled assuming orthorhombic symmetry,

which would require additional measurements to fully describe the nonlinear stiffness tensor (Sarkar et al. 2003, Sayers 2010).

Another potential cause for the difference between the nonlinear coefficients determined for the isotropic and deviatoric loading cycles could be the relative directions and magnitudes of strain between the two stress paths. For example, during isotropic loading all strains are positive (compression) and smaller magnitudes of strain are required for a given increase in mean stress (and thus stiffness). During deviatoric loading, samples are able to expand radially and thus exhibit negative changes of radial strain and much larger axial strains for a given change in mean stress. Therefore, the nonlinear coefficients C_{144} , C_{255} , and C_{366} are negative for deviatoric loading to account for the radial expansion during our tests, and C_{111} , C_{333} , C_{112} , and C_{133} are smaller for deviatoric loading, implying that larger strains are required in order to cause the same increase in stiffness as the isotropic nonlinear model. This effect is amplified by the stress-induced plastic strains imposed during the isotropic cycle. The large mean stresses and associated plastic strains incurred during the isotropic loading cycle increased rock stiffness prior to deviatoric loading, i.e. most of the compliant microstructural features were closed during isotropic stress loading. This behavior resulted in the deviatoric loading cycle exhibiting higher stiffness at lower mean stresses than the isotropic cycle and decreased stress-dependence of stiffness due to the stress and strain history of the rock (McCall and Guyer 1994, Sarout and Gueguen 2008).

6.4.2 Impact of layering and heterogeneity on stress-strain response

In addition to the measured differences in directional stiffness parameters and moduli, X-ray MicroCT images provide evidence of the impact that sample layering and heterogeneity have on rock stress-strain and failure behavior. Changes in lithology often relate to changes in mechanical properties, resulting in mechanical stratigraphy (Nelson 1985, Laubach et al. 2009). The mechanical stratigraphy of anisotropic rocks is well-documented and has been shown to cause variability in the stress field and fracture arrest, and re-orientation and branching at bed boundaries (Adachi et al., 2007, Suarez-Rivera et al. 2005; 2013, Ramos et. al 2017, Sosa Massaro et al., 2017). Plugs with bedding at 45° and 90° exhibit failure planes which are mostly preferentially oriented with bedding, and the 45° plug actually appears to fail along a single bedding plane toward the top of the sample (Figure 6-7). The location of failure in the 45° plug also provides insight into why it exhibited much smaller radial strains and overall axial contraction after failure. Since radial strain gauges were placed around the center of the sample, it is likely that displacement along the failure plane was not directly measured. If the failure plane were to intersect the radial measurement axis we would expect more appreciable radial strain anisotropy from slip along the failure plane, which would also be evidenced by dilatant volumetric strain behavior. Although failure does not occur along bedding in the 0° plug, the failure plane does appear to turn when approach bedding planes and reorient as a function of the mineral composition of the layer within which it travels.

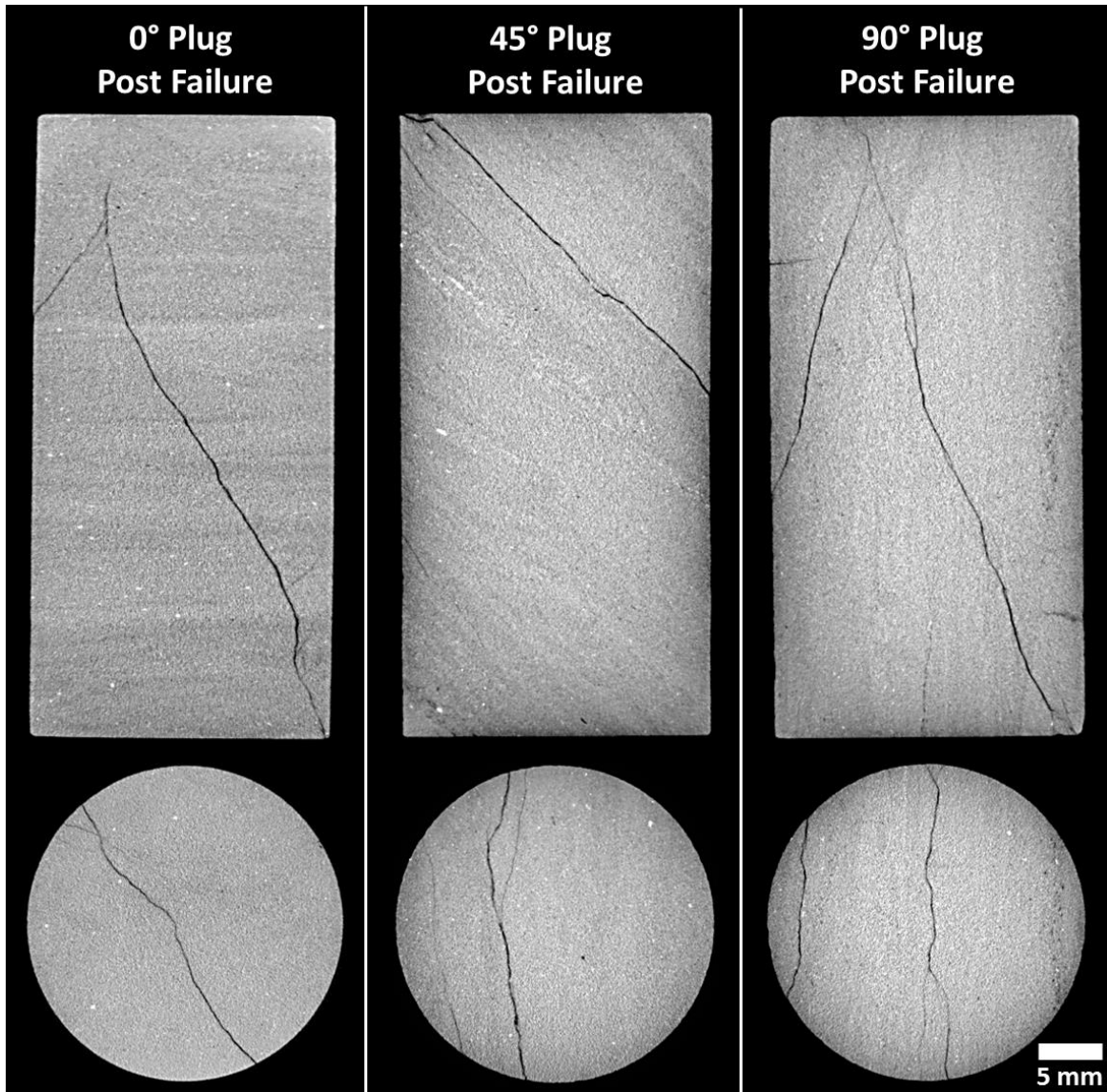


Figure 6-7 X-ray MicroCT images of oriented samples of Mancos Shale after failure. Cores are approximately 50 mm length x 25 mm diameter. Images highlight the impact of layering on fracture geometries and failure.

The observed failure plane geometries may also help to explain the clear strength anisotropy for Mancos Shale samples at several confining stresses, where 90° plugs exhibit the highest strength, followed by the 0° and 45° plugs (Figure 2-4). The 45° plugs exhibit

the least complex failure because bedding is oriented more closely to the typical shear failure angle, causing slip along a single bedding plane. Opposite to other laminated shales, the tested Mancos Shales samples exhibited significant interbedding strength without appreciable loss of strength in samples loaded at 45°. In the 0° plugs, bedding does not act as a plane of weakness due to its horizontal orientation, therefore more typical shear failure geometries are observed cutting through beds. The 90° plugs tend to exhibit fairly vertical failure planes along bedding, which is not as prevalent in Figure 6-7, but has been documented for other tested samples (Ramos et al. 2017). Although acting as planes of weakness, the vertical orientation of bedding causes the rock to split into column-like pieces of intact rock, which are more stable than an inclined shear failure plane. In order to fail, a fracture must turn and travel through these intact layers. Stress-strain curves in Figure 6-1 support the latter explanation, where the 90° plug exhibits a small amount of radial strain anisotropy as the rock preferentially expands perpendicular to bedding. When approaching peak stress, the sample shows a decrease in deviatoric stress coincident with a large increase in radial strain anisotropy, which could be linked to the initial splitting of the sample into these vertical columns. Deviatoric stress increases again on such relatively intact stiff columns until they fail in shear. Throughout this process, radial strain anisotropy increases appreciably as the failure plane opens preferentially perpendicular to bedding. The influence of layering and heterogeneity on rock mechanical properties and failure at the core scale may provide insight into similar behaviors documented at the field scale (Mayerhofer et al. 2010, Suarez-Rivera et al. 2013, Gale et al. 2014).

6.4.3 Field Implications

A nonlinear elastic model for VTI rock stiffness provides value for accurately translating measured seismic and wellbore sonic velocities into stiffness parameters and moduli. Understanding the directional- and stress-dependences of velocity (and thus stiffness) helps to identify spatial heterogeneity and discontinuities in unconventional formations (Sarout and Gueguen 2008). Our samples show that heterogeneity and discontinuities often challenge the assumption of VTI symmetry in shales. However, despite this potential limitation the VTI nonlinear model accurately predicts the stress dependence of stiffness, and dynamic moduli. Dynamic-to-static transforms can be used to convert calculated dynamic moduli into static moduli, which more accurately describe rock mechanical behavior to large strain processes such as drilling, hydraulic fracturing and depletion (Melendez-Martinez and Schmitt 2016). If lower frequency wellbore sonic or seismic measurements were to be used for the development of dynamic-static transforms, additional correction factors will likely be necessary to account for fluid- and frequency-dependent velocity dispersion.

Similar to the fractures in our tests, hydraulic fracture geometry can be severely altered due to the presence of mechanical stratigraphy and anisotropy (Suarez-Rivera et al. 2013, Mokhtari et al. 2014, Ouchi et al., 2016). More accurate estimation of static moduli can help to predict fracture propagation barriers and stress shadows effects (Roussel and Sharma 2011). Although the nonlinear model is useful for understanding the stress-dependence of stiffness, our results show that this only applies up to some threshold, where increases in plastic deformation tend to decrease the stress dependence of stiffness. Thus,

plastic strains also need to be considered when attempting to optimize completion strategies. The nonlinear VTI elastic model can help to determine the appropriate lateral depths, spacing for hydraulic fracture clusters and the potential impact on subsequent fractures (Olson 2008, Wu and Olson 2015). It is also important to apply the appropriate nonlinear coefficients for the type of stress loading path to be expected. For example, the same method could be used during uniaxial strain tests to derive nonlinear coefficients better suited to model a depletion stress loading path.

6.5 CONCLUSIONS

We used combined triaxial stress testing and ultrasonic monitoring to measure and model the isotropic and deviatoric stress dependences of static and dynamic mechanical properties in Mancos Shale plugs with bedding oriented at 0°, 45°, and 90°. Results show that nonlinear coefficients derived from an isotropic loading cycle are not suitable for modeling changes in stiffness during deviatoric loading. Potential explanations for the lack of applicability to different stress loading paths are related to stress-induced anisotropy along the symmetry axis of 90° samples, and the differing strain directions and magnitudes associated with isotropic and deviatoric loading.

Results highlight the need for nonlinear VTI models to accurately describe rock mechanical behavior and reinforce the inadequacies of assuming isotropy. Dynamic Young's moduli E_h are more than 10 GPa higher than E_v and both moduli exhibit strong stress dependences, where E_h increases by roughly 15 GPa during the first 60% of deviatoric stress loading. Measured static moduli are typically less than 50% of their

dynamic equivalent and exhibit separate anisotropic and nonlinear relationships. Therefore, when attempting to estimate static properties from dynamic measurements, dynamic-static transforms must take into consideration these complex nonlinear and anisotropic behaviors. We show that using a linear fit to the ratios of dynamic-to-static moduli as a function of stress is a reliable procedure. Averaging the ratios is also adequate for Young's moduli, but shows significant misfit for Poisson's ratios. Furthermore, although Mancos samples deviate from the assumption of VTI, the nonlinear model provides excellent matches for stiffness parameters and moduli. Since rocks exhibit different degrees of anisotropy and stress dependence, the dynamic-static transforms developed for Mancos Shale likely have limited applicability to other rocks. Performing our methodology for several shales may provide an avenue for finding common behavior and extending the applicability of these relationships.

X-ray microCT images show the important role that sample layering plays in rock failure behavior and fracture geometry. We showed evidence of layering-induced mechanical stratigraphy causing fracture reorientation in response to lithological variations. Bedding-induced variabilities in the strain field also make bedding planes a preferential failure path but do not significantly decrease sample strength. The observed impact of layering and heterogeneity on failure at the core scale calls for larger-scale observations.

Measured irrecoverable strains during isotropic and deviatoric loading indicate the need for an improved model, which more accurately describe the combined elastic and plastic deformational behavior of real shale rocks. Consideration of plastic strains will

increase the applicability of the model to processes involving large stresses and strains such as drilling, hydraulic fracturing, and depletion.

6.6 SUPPORTING INFORMATION

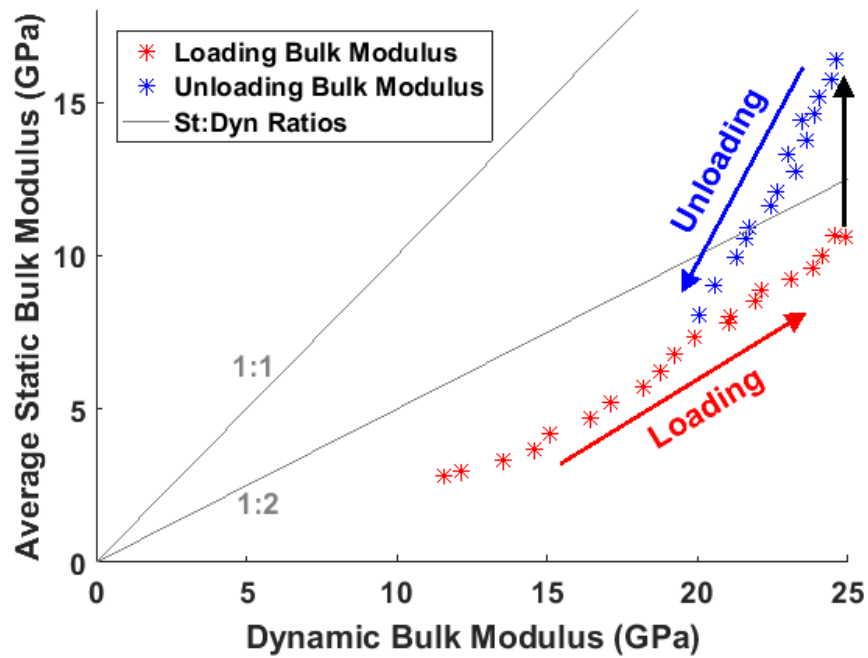


Figure 6-8 Static and dynamic bulk moduli during isotropic loading and unloading in Figure 6-3. Arrows point in the direction of increasing time during testing. Gray lines describe constant static-to-dynamic ratios. Static bulk modulus represents the average of the 3 oriented samples.

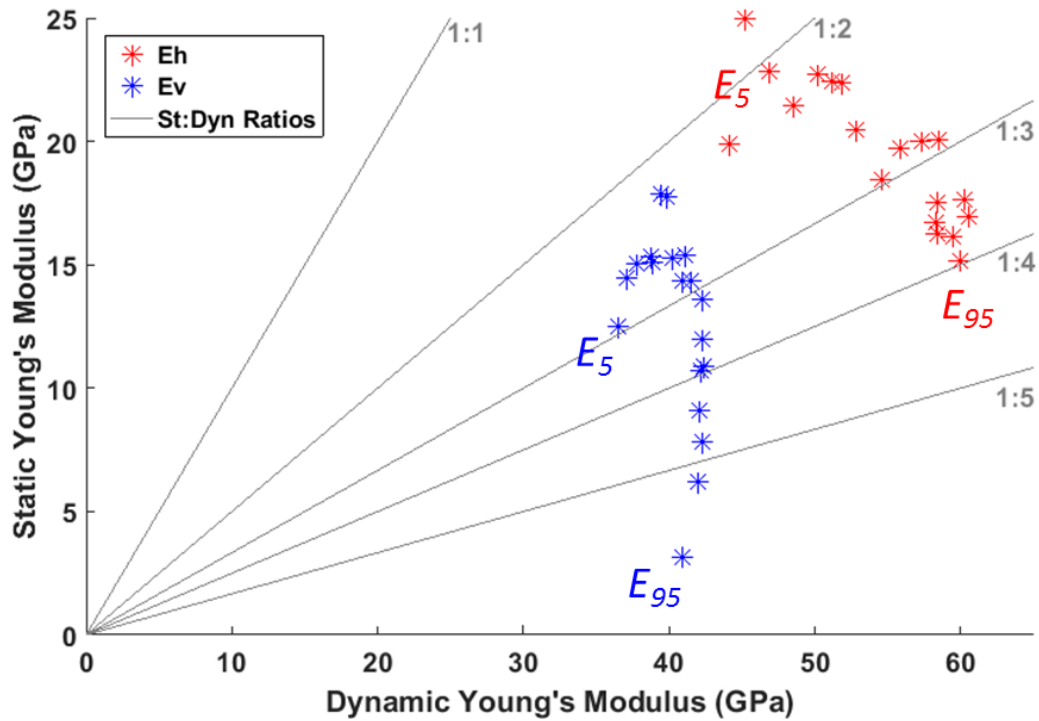


Figure 6-9 Tangent static and dynamic Young's moduli E_h (red) and E_v (blue) during deviatoric loading. E_5 and E_{95} represent the moduli at 5% and 95% of peak stress, respectively. Gray lines identify constant ratios of static-to-dynamic moduli.

Table 6-3 Results from tests at several confining stresses used to determine shear failure envelopes for oriented plugs.

Core Orientation	0°	45°	90°
Confining Stress (MPa)	Peak Deviatoric Stress (MPa)		
0.69	25.1	19.3	27.6
3.45	37.0	25.3	31.7
6.90	37.0	34.5	43.0
20.7	66.9	62.7	76.3

Table 6-4 Isotropic stresses for the three plug orientations and the corresponding stiffness coefficients C_{ij} , and dynamic and static bulk moduli, K_{Dyn} and K_{St} .

Isotropic Stress (MPa)			C_{ij} (GPa)							Bulk Moduli (GPa)	
0°	45°	90°	C_{11}	C_{12}	C_{13}	C_{33}	C_{44}	C_{55}	C_{66}	K_{Dyn}	K_{St}
3.27	4.33	5.08	31.41	7.98	1.63	23.59	10.59	10.51	11.71	36.55	12.51
7.47	8.46	9.22	33.30	8.64	1.43	25.22	11.06	11.08	12.33	37.11	14.47
11.61	12.60	13.36	35.79	9.88	2.51	26.66	11.62	11.64	12.95	37.79	15.07
15.77	16.74	17.52	37.82	11.10	2.73	28.68	11.92	11.99	13.36	38.72	15.35
19.88	20.32	21.63	39.33	11.49	2.48	30.41	12.33	12.47	13.92	38.90	15.11
24.02	24.46	25.77	41.45	12.76	3.65	31.64	12.82	13.03	14.35	39.48	17.90
28.16	28.60	29.90	42.63	13.28	3.89	33.09	13.27	13.37	14.68	39.84	17.78
32.29	32.83	34.04	44.53	14.21	4.57	34.90	13.57	13.77	15.16	40.19	15.26
36.43	36.87	38.18	46.36	15.52	4.29	35.91	14.00	14.09	15.42	40.89	14.34
40.56	41.08	42.32	47.96	16.24	4.18	36.87	14.24	14.29	15.86	41.09	15.36
44.70	45.21	46.50	48.97	16.51	4.80	37.75	14.55	14.58	16.23	41.54	14.32
48.84	49.35	50.66	50.59	17.49	5.90	38.66	14.72	14.79	16.55	42.27	13.61
52.98	53.51	54.80	51.56	17.56	5.37	39.51	14.90	15.01	17.00	42.31	11.97
57.13	57.63	58.93	52.31	17.65	6.42	40.34	15.11	15.21	17.33	42.39	10.90
61.25	61.81	61.04	52.81	17.91	6.37	41.01	15.36	15.44	17.45	42.15	10.73
65.50	65.92	67.20	54.07	18.71	7.36	41.69	15.52	15.55	17.68	42.28	7.81
69.59	70.04	69.34	54.24	18.39	8.64	42.34	15.70	15.71	17.93	42.12	9.07
73.73	74.24	73.41	54.91	18.73	8.82	42.75	15.89	15.83	18.09	41.94	6.18
77.87	78.38	79.62	55.89	19.10	9.70	43.32	15.99	15.99	18.40	40.92	3.12
82.74	82.74	82.74	56.29	19.00	8.44	44.38	16.25	16.29	18.65	39.22	0.38

Table 6-5 The *P*- and *S*- wave velocities measured during isotropic loading. Velocities were measured on 0° (red), 45° (green), and 90° (blue) plugs. Figure 2-4 shows the orientations of the measured velocities. We estimate a maximum of 5% error in the C_{ij} , which is mostly associated with picking first arrivals for velocity calculation.

Average Isotropic Stress (MPa)	Velocities (m/s)								
	V_{P33}	V_{S3a}	V_{S3b}	V_{P45}	V_{SH45}	V_{SV45}	V_{P11}	V_{SH1}	V_{SV1}
4.23	3047.9	2034.0	2041.8	3518.7	2148.9	2016.0	3164.5	2090.0	2073.3
8.38	3149.5	2087.5	2085.3	3620.8	2203.2	2059.8	3246.3	2155.4	2116.4
12.52	3236.1	2138.1	2136.3	3751.2	2256.7	2118.5	3370.6	2199.8	2182.1
16.68	3354.4	2168.9	2162.8	3853.9	2290.6	2167.2	3453.0	2225.9	2223.9
20.61	3452.1	2211.0	2198.6	3928.3	2337.1	2219.6	3515.9	2248.9	2242.1
24.75	3519.9	2259.0	2240.8	4031.1	2371.7	2263.8	3624.8	2286.1	2282.0
28.89	3598.2	2286.9	2278.6	4086.4	2397.7	2304.4	3681.4	2315.2	2326.9
33.05	3694.2	2319.9	2303.4	4175.0	2436.2	2333.5	3767.0	2345.1	2357.9
37.16	3745.7	2346.1	2338.6	4258.2	2455.7	2367.9	3814.4	2383.9	2384.8
41.32	3794.5	2362.5	2358.2	4330.0	2490.2	2395.7	3855.9	2413.9	2412.5
45.47	3838.3	2385.0	2382.6	4374.1	2518.2	2432.1	3907.6	2435.5	2437.5
49.62	3883.2	2402.0	2396.4	4444.8	2542.2	2450.4	3977.1	2457.5	2456.6
53.76	3924.7	2419.4	2410.0	4486.1	2575.9	2477.2	3997.0	2476.1	2476.3
57.90	3964.9	2434.4	2426.5	4517.4	2600.1	2498.0	4048.6	2494.9	2486.3
61.37	3996.6	2452.3	2446.3	4538.6	2608.8	2507.7	4070.9	2512.8	2500.8
66.21	4028.7	2460.6	2458.2	4590.7	2625.1	2535.6	4122.8	2527.6	2514.7
69.66	4059.2	2472.7	2472.1	4597.8	2643.2	2542.2	4166.6	2542.3	2530.9
73.79	4077.8	2481.2	2486.1	4625.1	2654.6	2557.3	4188.5	2557.7	2543.8
78.62	4104.3	2493.6	2493.9	4664.8	2676.1	2575.8	4233.8	2566.9	2558.3
82.74	4152.9	2515.8	2513.1	4680.8	2694.0	2597.8	4233.0	2580.2	2568.6

Table 6-6 Static strains for the three plug orientations during isotropic loading. The average isotropic stress is shown for reference. The 0° and 90° plugs have principal strain orientations, however the 45° plug is denoted ϵ_{ax} for strain in the axial direction, ϵ_{ra} for radial strain in the direction parallel to bedding, and ϵ_{rb} for radial strain perpendicular to bedding. ϵ_v represents the volumetric strain.

Average Isotropic Stress (MPa)	Static Strains (10^{-3})											
	0° ϵ_{33}	0° ϵ_{11}	0° ϵ_{22}	0° ϵ_v	90° ϵ_{11}	90° ϵ_{22}	90° ϵ_{33}	90° ϵ_v	45° ϵ_{ax}	45° ϵ_{ra}	45° ϵ_{rb}	45° ϵ_v
4.23	0.00	0.00	0.00	0.00	0.00	0.00	0.00	0.00	0.00	0.00	0.00	0.00
8.38	0.64	0.35	0.37	1.41	0.37	0.37	0.59	1.37	0.53	0.40	0.39	1.37
12.52	1.16	0.67	0.70	2.67	0.68	0.70	1.09	2.61	0.94	0.76	0.75	2.59
16.68	1.66	0.98	1.02	3.79	0.98	1.03	1.58	3.72	1.35	1.11	1.10	3.71
20.61	2.10	1.26	1.31	4.78	1.25	1.32	2.00	4.67	1.70	1.43	1.42	4.59
24.75	2.48	1.51	1.58	5.65	1.49	1.59	2.37	5.55	2.01	1.73	1.72	5.51
28.89	2.81	1.74	1.81	6.44	1.71	1.84	2.70	6.33	2.29	2.00	1.99	6.34
33.05	3.12	1.94	2.03	7.15	1.92	2.06	3.00	7.04	2.55	2.25	2.25	7.13
37.16	3.39	2.13	2.22	7.80	2.10	2.27	3.27	7.69	2.79	2.48	2.49	7.81
41.32	3.65	2.31	2.40	8.41	2.28	2.45	3.51	8.29	3.01	2.69	2.72	8.47
45.47	3.89	2.47	2.57	8.97	2.44	2.63	3.74	8.84	3.22	2.88	2.93	9.07
49.62	4.11	2.62	2.73	9.48	2.59	2.79	3.95	9.36	3.41	3.06	3.12	9.63
53.76	4.32	2.77	2.87	9.99	2.72	2.92	4.13	9.84	3.60	3.22	3.31	10.16
57.90	4.52	2.91	3.01	10.46	2.86	3.07	4.31	10.31	3.78	3.38	3.49	10.65
61.37	4.71	3.04	3.15	10.91	2.98	3.19	4.47	10.53	3.95	3.53	3.65	11.14
66.21	4.90	3.17	3.27	11.36	3.09	3.31	4.62	11.17	4.11	3.67	3.81	11.62
69.66	5.06	3.29	3.39	11.77	3.21	3.44	4.78	11.37	4.27	3.81	3.97	12.06
73.79	5.25	3.42	3.52	12.18	3.34	3.57	4.95	11.76	4.44	3.95	4.12	12.50
78.62	5.43	3.55	3.64	12.53	3.46	3.70	5.11	12.34	4.60	4.09	4.27	12.93
82.74	5.66	3.70	3.79	13.15	3.58	3.83	5.27	12.68	4.77	4.24	4.43	13.43

Table 6-7 The % of peak stress during deviatoric loading with the respective deviatoric stresses for the three plug orientations, and the corresponding stiffness coefficients C_{ij} . We estimate a maximum of 5% error in the C_{ij} , which is mostly associated with picking first arrivals for velocity calculation.

% of Peak Stress	Deviatoric Stress (MPa)			C_{ij} (GPa)								
	0°	45°	90°	C_{11}	C_{12}	C_{13}	C_{33}	C_{44}	C_{55}	C_{66}		
5	7.57	6.96	7.17	45.17	13.82	6.76	38.10	14.44	14.50	15.67		
10	13.36	12.17	17.74	46.37	14.56	7.30	38.86	14.57	14.60	15.90		
15	20.34	19.56	26.24	47.78	15.60	7.34	39.49	14.71	14.73	16.09		
20	27.78	26.00	34.67	48.87	16.36	6.62	40.06	14.79	14.83	16.25		
25	33.75	31.46	42.61	50.31	17.47	7.00	40.34	14.89	14.93	16.42		
30	41.58	39.00	50.24	51.33	18.22	7.47	41.09	15.02	15.03	16.55		
35	47.53	43.95	58.01	51.96	18.51	7.55	41.46	15.06	15.06	16.72		
40	55.40	51.23	65.74	52.94	19.18	7.87	41.91	15.17	15.18	16.88		
45	62.91	55.97	75.77	54.17	20.14	7.62	42.45	15.22	15.26	17.01		
50	68.34	62.59	83.27	55.16	20.86	7.77	42.67	15.25	15.28	17.15		
55	75.32	68.87	92.48	56.25	21.76	7.71	43.06	15.25	15.30	17.24		
60	83.32	74.84	99.57	56.85	22.21	7.05	43.52	15.24	15.32	17.32		
65	89.45	82.07	109.14	57.19	22.45	7.70	43.81	15.27	15.34	17.37		
70	96.64	88.88	116.15	57.27	22.38	8.04	44.01	15.26	15.32	17.45		
75	103.16	94.90	124.90	57.77	22.78	9.13	44.22	15.24	15.30	17.50		
80	110.40	100.24	133.46	58.71	23.62	9.52	44.48	15.22	15.23	17.55		
85	117.56	107.46	141.66	59.47	24.32	10.16	44.59	15.13	15.11	17.57		
90	124.82	113.24	150.29	59.90	24.76	10.63	44.61	14.98	14.94	17.57		
95	131.74	119.44	158.67	60.32	25.19	12.40	44.51	14.81	14.67	17.57		
100	138.31	125.86	166.01	60.50	25.36	13.46	43.43	14.20	14.10	17.57		

Table 6-8 The *P*- and *S*-wave velocities measured at each % of peak stress during deviatoric loading. Velocities were measured on 0° (red), 45° (green), and 90° (blue) plugs. Figure 2-4 shows the orientations of the measured velocities. We estimate a maximum of 5% error in the C_{ij} , which is mostly associated with picking first arrivals for velocity calculation.

% of Peak Stress	Velocities (m/s)								
	V_{P33}	V_{S3a}	V_{S3b}	V_{P45}	V_{SH45}	V_{SV45}	V_{P11}	V_{SH1}	V_{SV1}
5	3857.1	2379.6	2374.3	3898.8	2417.4	2401.5	4203.0	2475.7	2397.3
10	3894.8	2387.4	2385.4	3942.2	2429.6	2409.8	4258.0	2493.7	2414.1
15	3925.9	2397.8	2395.7	3976.0	2440.8	2420.9	4321.7	2507.7	2427.2
20	3953.8	2405.8	2402.1	3985.1	2449.5	2427.9	4370.3	2520.3	2437.6
25	3967.4	2413.3	2410.4	4022.4	2455.5	2434.8	4433.9	2533.1	2450.9
30	4003.6	2421.5	2420.6	4060.2	2469.8	2445.0	4478.1	2542.9	2458.7
35	4021.5	2424.0	2423.5	4076.3	2474.2	2449.1	4505.1	2556.0	2469.4
40	4043.0	2433.0	2432.5	4107.3	2483.0	2458.2	4547.1	2567.6	2477.3
45	4068.7	2439.6	2435.9	4128.3	2489.1	2462.0	4599.0	2577.4	2489.3
50	4079.2	2441.3	2438.1	4149.0	2494.1	2469.1	4640.6	2587.6	2497.3
55	4097.3	2442.7	2438.5	4167.8	2500.0	2476.3	4685.8	2594.4	2503.6
60	4119.2	2443.8	2437.3	4166.3	2506.0	2479.9	4710.4	2599.9	2510.2
65	4132.5	2445.2	2439.6	4189.0	2510.7	2485.1	4723.9	2603.5	2513.5
70	4142.2	2443.7	2439.1	4198.4	2509.5	2489.3	4727.1	2609.1	2518.6
75	4152.1	2442.2	2437.5	4230.9	2513.2	2492.1	4747.7	2612.7	2522.0
80	4164.6	2437.0	2435.8	4252.3	2514.0	2493.6	4786.0	2616.3	2531.4
85	4170.4	2428.0	2429.3	4272.8	2516.1	2497.3	4816.5	2618.4	2530.2
90	4172.6	2414.6	2418.4	4281.6	2519.3	2500.1	4834.3	2618.4	2539.8
95	4170.5	2394.2	2405.3	4313.4	2517.8	2499.5	4852.3	2618.5	2543.9
100	4127.1	2351.2	2359.5	4305.0	2512.9	2492.8	4861.4	2619.8	2539.2

Table 6-9 Static strains for the three plug orientations during deviatoric loading. The % of peak stress is shown for reference. The 0° and 90° plugs have principal strain orientations, however the 45° plug is denoted ϵ_{ax} for strain in the axial direction, ϵ_{ra} for radial strain in the direction parallel to bedding, and ϵ_{rb} for radial strain perpendicular to bedding. ϵ_v represents the volumetric strain.

% of Peak Stress	Static Strains (10^{-3})											
	0° ϵ_{33}	0° ϵ_{11}	0° ϵ_{22}	0° ϵ_v	90° ϵ_{11}	90° ϵ_{22}	90° ϵ_{33}	90° ϵ_v	45° ϵ_{ax}	45° ϵ_{ra}	45° ϵ_{rb}	45° ϵ_v
5	0.00	0.00	0.00	0.00	0.00	0.00	0.00	0.00	0.00	0.00	0.00	0.00
10	0.48	-0.11	-0.11	0.28	0.44	-0.08	-0.09	0.31	0.28	-0.05	-0.07	0.13
15	0.94	-0.22	-0.24	0.52	0.82	-0.15	-0.17	0.51	0.57	-0.12	-0.15	0.33
20	1.39	-0.35	-0.36	0.73	1.20	-0.23	-0.26	0.71	0.87	-0.18	-0.24	0.47
25	1.83	-0.47	-0.49	0.87	1.56	-0.31	-0.35	0.91	1.16	-0.25	-0.32	0.58
30	2.26	-0.61	-0.63	1.04	1.92	-0.39	-0.45	1.09	1.46	-0.33	-0.42	0.74
35	2.69	-0.76	-0.78	1.16	2.31	-0.49	-0.56	1.26	1.75	-0.40	-0.51	0.83
40	3.12	-0.91	-0.94	1.29	2.69	-0.59	-0.67	1.41	2.06	-0.49	-0.61	0.98
45	3.56	-1.08	-1.10	1.40	3.10	-0.69	-0.80	1.62	2.38	-0.58	-0.72	1.07
50	4.04	-1.27	-1.29	1.48	3.51	-0.80	-0.93	1.77	2.71	-0.68	-0.84	1.20
55	4.52	-1.47	-1.50	1.57	3.94	-0.93	-1.07	1.97	3.07	-0.78	-0.98	1.31
60	5.03	-1.70	-1.73	1.65	4.35	-1.05	-1.21	2.09	3.48	-0.91	-1.14	1.42
65	5.58	-1.96	-1.99	1.67	4.78	-1.19	-1.37	2.25	3.91	-1.06	-1.31	1.55
70	6.18	-2.28	-2.31	1.66	5.22	-1.34	-1.54	2.34	4.37	-1.22	-1.50	1.67
75	6.83	-2.66	-2.68	1.59	5.67	-1.50	-1.74	2.45	4.90	-1.41	-1.73	1.77
80	7.58	-3.14	-3.18	1.43	6.15	-1.69	-1.99	2.55	5.48	-1.63	-1.99	1.85
85	8.44	-3.79	-3.84	1.11	6.68	-1.92	-2.36	2.56	6.15	-1.90	-2.33	1.94
90	9.66	-4.95	-5.07	0.52	7.26	-2.19	-2.91	2.47	7.11	-2.25	-2.90	2.00
95	10.86	-6.05	-6.23	-0.62	7.86	-2.48	-3.48	2.04	8.06	-2.61	-3.45	2.02
100	12.85	-8.31	-8.70	-4.16	8.54	-2.86	-4.46	1.21	9.66	-3.15	-4.54	1.97

Table 6-10 Dynamic and static Young's moduli E and Poisson's ratios ν as a function of the % of peak stress during deviatoric loading.

% of Peak Stress	Dynamic Moduli (GPa)					Static Moduli (GPa)				
	E_{vDyn}	E_{hDyn}	ν_{12Dyn}	ν_{13Dyn}	ν_{31Dyn}	E_{vSt}	E_{hSt}	ν_{12St}	ν_{13St}	ν_{31St}
5	36.55	44.17	0.29	0.13	0.11	12.51	19.91	0.16	0.18	0.18
10	37.11	45.24	0.29	0.13	0.12	14.47	24.97	0.18	0.25	0.23
15	37.79	46.90	0.31	0.13	0.12	15.07	22.84	0.20	0.24	0.27
20	38.72	48.58	0.32	0.11	0.10	15.35	21.44	0.20	0.23	0.28
25	38.90	50.21	0.33	0.12	0.10	15.11	22.74	0.24	0.27	0.31
30	39.48	51.16	0.34	0.12	0.11	17.90	22.43	0.27	0.29	0.35
35	39.84	51.83	0.34	0.12	0.11	17.78	22.37	0.26	0.30	0.37
40	40.19	52.87	0.34	0.12	0.11	15.26	20.46	0.27	0.31	0.36
45	40.89	54.59	0.36	0.12	0.10	14.34	18.43	0.24	0.28	0.35
50	41.09	55.83	0.36	0.12	0.10	15.36	19.73	0.28	0.33	0.42
55	41.54	57.36	0.37	0.11	0.10	14.32	20.03	0.29	0.34	0.47
60	42.27	58.43	0.38	0.10	0.09	13.61	17.50	0.28	0.32	0.48
65	42.31	58.49	0.38	0.11	0.10	11.97	20.05	0.38	0.44	0.47
70	42.39	58.32	0.37	0.11	0.10	10.90	16.69	0.37	0.41	0.56
75	42.15	58.36	0.37	0.13	0.11	10.73	16.24	0.37	0.43	0.56
80	42.28	59.48	0.38	0.13	0.12	7.81	16.13	0.38	0.45	0.63
85	42.12	60.22	0.38	0.14	0.12	9.07	17.64	0.45	0.63	0.73
90	41.94	60.60	0.39	0.15	0.13	6.18	16.94	0.56	1.04	0.88
95	40.92	59.95	0.38	0.17	0.14	3.12	15.16	0.55	1.75	1.00
100	39.22	59.61	0.38	0.19	0.16	0.38	4.19	0.73	1.80	1.24

7. Microstructural Controls on Elastic Anisotropy of Finely Laminated Mancos Shale

Matthew J. Ramos, D. Nicolas Espinoza, Eric J. Goldfarb, Nicola Tisato, Stephen E. Laubach, and Carlos Torres-Verdín

7.1 CHAPTER ABSTRACT

Shales commonly exhibit anisotropy in their elastic wave velocity, which directly impacts the accuracy of seismic imaging and their geomechanical response to drilling and completions. Anisotropy is often caused by mineralogical layering, fractures, and rock fabric (i.e. oriented grains and intrinsic anisotropy of clay sediments). However, the relative impact of each of these features on macroscopic shale properties is not well understood. We combined scanning electron microscopy (SEM) and X-ray micro-computed tomography (CT) to image the mineralogical and structural heterogeneity of Mancos Shale and converted the acquired CT and SEM images into heterogeneous 2D elastic models. We used wave propagation numerical simulations to understand the effects that layering and fractures have on elastic wave velocity anisotropy. Consistent V_p/V_s ratios around 1.46 for modeled and measured velocities validates SEM observations of a quartz-dominated shale lithology. CT-derived models containing layering and fractures exhibit 28.6% and 58.8% of the V_p and V_s anisotropy observed in the laboratory, whereas SEM derived models exhibit 74.5% and 73.2%, respectively. The increased anisotropy of SEM-derived elastic models is a result of the ability of the SEM to discern individual mineral grains and microstructural features, whereas the CT models require the use of an effective medium theory to model variations of lithology. Overall, modeled wave propagation perpendicular to bedding more closely captures the experimental velocities than parallel to

bedding. Therefore, sub-resolution rock fabric anisotropy likely accounts for the relatively larger velocity mismatch in the parallel direction, and is likely responsible for the decreased anisotropy in coarse rock models. Future modeling would require higher resolution images to structurally constrain these features and/or anisotropic elements to account for fabric anisotropy. Despite some limitations, our study provides a reliable procedure to estimate anisotropy of rock dynamic mechanical properties using SEM and CT imaging combined with numerical simulation of wave propagation.

7.2 INTRODUCTION

The directional dependence of elastic wave velocity in sedimentary rocks is governed by several lithological properties such as presence of layering, aligned fractures and discontinuities, and the intrinsic anisotropy of clay minerals and clay sediments (Gueguen and Palciauskas 1994, Mavko et al. 2009). The relative importance of each of these properties depends on the scale of investigation (Nur 1971, Lo et al. 1986, Vernik and Nur 1992, Rasolofosaon 1998, Sayers 2004, Valcke et al. 2006, Zoback 2007, Sone and Zoback 2013). For example, seismic-scale anisotropy is mostly a result of variations in bulk physical properties (mass density and elastic stiffness) in rock layers (10-100 m scale) and it is often associated with major changes in depositional environment (Sayers 2005, Anderson and Harris 2006). At a much smaller scale, individual clay minerals exhibit intrinsic crystallographic elastic anisotropy (Johnston and Christensen 1995). When clays are preferentially oriented during compaction and lithification of shales and other clay-rich rocks, clay-rich layers become an important contributor to velocity anisotropy at the seismic scale (Wang 2002, Dewhurst and Siggins 2006).

Structural diagenesis may also cause anisotropy (Siegesmund et al. 1996). Compaction-induced changes in grain orientation/aspect ratio can give rise to a distinct fabric and associated cleavage, and deviatoric tectonic-stresses can cause rock failure at several scales (Powell 1979, Laubach et al. 2010, Milliken and Reed 2010). Wave velocities have been shown to be higher in the direction parallel to rock fabric/cleavage and fractures, and lower in the direction orthogonal to these features (Nur 1971, Scott et al 1993, Ramos et al. 2017). Diagenetic healing (mineralization) of fractures can reduce their compliance and overall impact on anisotropy (Anders and Laubach 2014, Gale et al. 2014). Elastic nonlinearity can also manifest in velocity anisotropy when a rock is subjected to deviatoric stresses, which closes preferentially oriented and compliant fractures, grain boundary porosity, and other microstructural defects (Nur and Simmons 1969, Schwartz et al. 1994). Elastic nonlinearity is known to cause an otherwise isotropic rock to exhibit faster velocities in the direction of maximum stress (Sinha and Kostek, 1996, Johnson and Rasolofosaon 1996, Winkler 1996, Sayers 2002, Fang et al. 2013, Ramos et al. - Undergoing Review).

Although several studies have emphasized the importance of individual rock unit characteristics (such as layering, clay crystallographic anisotropy, rock fabric, fractures, and microstructural compliance) on velocity anisotropy, rarely do shales contain only one of these features. Furthermore, such features are heterogeneously distributed throughout the rock. For example, a number of shales exhibit mm- to cm-thick clay-rich laminations, however during deposition of these layers, the unlithified sediments are often reworked and mixed with other fine-grained material by bottom currents (Slatt and Abousleiman

2011). Over time, these fine laminations aggregate into meter thick packages that are compacted and develop a preferentially oriented fabric during burial (Birgenheier et al. 2017). The stratigraphic boundaries between these micro and macro-scale layers often act as planes of weakness. The mechanical stratigraphy induced by these lithologic variations may dictate the location and orientation of natural fractures (Laubach et al. 2009, Gale et al. 2014). Natural fractures and pore space may also be preferential sites for the growth of secondary minerals such as carbonate cements or clays, which could decrease or increase velocity anisotropy depending on their orientation.

The measured velocity anisotropy of shales is a cumulative response to all of the above lithological characteristics. In shales, fractures may be in subparallel sets at a high angle to bedding, but they also commonly occur parallel or subparallel to bedding (Hancock 1985, Gale et al. 2014). Thus, both sedimentary layering and fractures can potentially produce anisotropy in this configuration. Decoupling and quantifying their relative impacts on macroscopic rock anisotropy may be useful for revealing information about hydrocarbon-bearing formations. For example, changes in sonic anisotropy along a horizontal wellbore may be related to spatial variations in the degree of natural fracturing, where decreases in anisotropy may be linked to the presence of bed-normal fractures. Since bed-normal fractures are less likely to be sampled during coring of the vertical exploration well, the ability to quantify their sonic response and identify naturally fractured zones can have important implications for hydraulic fracturing and enhancing hydrocarbon production from shales reservoirs (Crampin 1985, Germanovich and Astakhov 2004, Suarez-Rivera et al. 2013, Bosziak et al. 2014, Laubach et al. 2016). Accurately

determining the impact of these lithological features on dynamic elastic anisotropy may also provide a means for estimating their influence on the rock static mechanical response to the large stresses and strains imposed during drilling and completions (Ramos et al. 2017, Ramos et al. Undergoing Review).

We present a combination of imaging and numerical simulations for analyzing the relative importance of lithologic characteristics such as mineralogical variability, layering, and the presence of bed-parallel fractures on the anisotropy of elastic wave velocity. First, we present laboratory measurements of Mancos Shale velocity anisotropy, and provide X-Ray micro-computed tomography (CT) and Scanning Electron Microscopy (SEM) images to highlight the mineralogical and structural features likely contributing to the measured anisotropy. We present methods for combining the information gained from CT and SEM imaging to construct velocity models, which account for the mineralogical and structural heterogeneity of Mancos Shale at several scales. We focus on the simulation of elastic wave propagation in the directions parallel and perpendicular to layering and/or fractures within the various models. We compare simulation results to the laboratory measurements to quantify the relative contribution of the aforementioned lithologic features on the measured velocity anisotropy.

7.3 MANCOS SHALE CHARACTERIZATION

7.3.1 Elastic Anisotropy

Thomsen's parameters in Figure 7-1 emphasize the prominent *P*- and *S*-wave velocity anisotropy and nonlinearity of Mancos Shale prior to and during triaxial stress testing

(Ramos et al. 2017). Figures 7-1-A to 7-1-C compare Thomsen’s parameters for the set of unconfined plugs (0°, 45°, and 90°) to sets of plugs subjected to constant confining stress (0.69, 3.45, and 6.9 MPa) and then loaded axially until failure. Anisotropy parameters tend to decrease with increasing deviatoric stress. For example, ϵ and δ decrease by roughly 50% and γ decreases by almost 30% during deviatoric loading. The decrease in anisotropy with increasing deviatoric stress indicates that velocities perpendicular to bedding increase more upon stress loading than those parallel to bedding. This behavior supports previous observations that bed-parallel fractures and other compliant microstructural features play an important role in Mancos elastic anisotropy and nonlinearity (Chandler et al. 2016, Ramos et al. 2017, Ramos et al. - Undergoing Review). For reference, Table 7-1 shows the velocity measurements and corresponding Thomsen’s parameters for the set of unconfined Mancos plugs. The Appendix details the experimental methods used for sample preparation and testing, while Table SII summarizes peak stresses for each test.

Table 7-1 Experimental measurements of P - and S -wave velocities on unconfined cores with bedding oriented at 0°, 45°, and 90°. Velocities were used to calculate the Thomsen anisotropy parameters ϵ , γ , and δ . The 0° and 90° measurements correspond to wave propagation perpendicular and parallel to bedding, respectively. For the 45° and 90° samples, perpendicular shear wave measurements V_{sa} and V_{sb} were oriented parallel and perpendicular to bedding, respectively, and had no preferred orientation for the 0° sample.

Bedding Orientation	V_p (m/s)	V_{sa} (m/s)	V_{sb} (m/s)
0°	3058	2150	2140
45°	3295	2226	2105
90°	3495	2382	2096
Thomsen Parameter	ϵ	γ	δ
	0.150	0.122	0.154

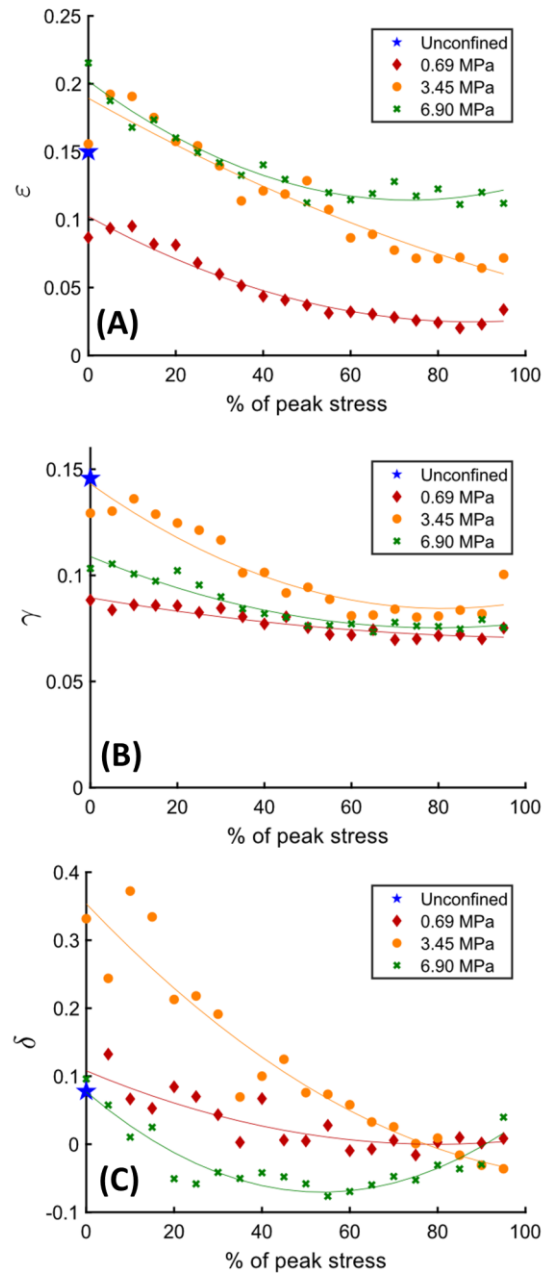


Figure 7-1 Experimentally determined Thomsen anisotropy parameters (A) ϵ , (B) γ , and (C) δ for Mancos Shale sample sets: unconfined (blue), and subjected to a deviatoric stress loading path until failure with a constant confining stress of 0.69 MPa (red diamonds), 3.45 MPa (orange circles), 6.9 MPa (green x's). Since Thomsen parameters are a combination of measurements from three oriented plugs (0° , 45° , and 90°), they are calculated and plotted as a function of the % of peak stress for each test. The peak stresses for each core orientation and confining stress can be found in Table 6-3.

7.3.2 Mineralogical Variations Measured from SEM

In order to better understand the mechanisms contributing to velocity anisotropy of Mancos Shale and its stress-dependence, we examined samples at several scales. Mancos samples exhibit mm-thick dark and light colored layers at both the core and thin section scales, which are easily distinguished by the unaided eye (Figures 7-2-A and 7-2-B). We performed SEM analyses to identify and quantify the mineralogy within each layer. SEM results show that the photographed light and dark variations in lithology correspond to predominantly quartz-rich and clay-rich (kaolinite, illite, and smectite) layers, respectively (Figure 7-2-C) (Grigg 2016). Diagenetic calcite cements are prominent in the quartz-rich facies and are also present to a lesser degree in the clay-rich facies, whereas dolomite and pyrite are slightly more abundant in the clay-rich facies. Albite and orthoclase are also present throughout the sample, but less abundant than other minerals. Although Mancos samples appear to have an overall laminated quartz-clay composition, dispersed clays (both grain-coating and pore-filling) are present within the quartz-rich layers, and the clay-rich layers contain an abundance of finer grained quartz. Table 7-2 summarizes the average mineralogical composition for the two endmembers (quartz-rich and clay-rich) facies in Mancos samples. The endmember compositions represent only 25% of the imaged scanline, whereas the remainder of the sample is comprised of an intermediate composition with almost equal parts of clay and quartz.

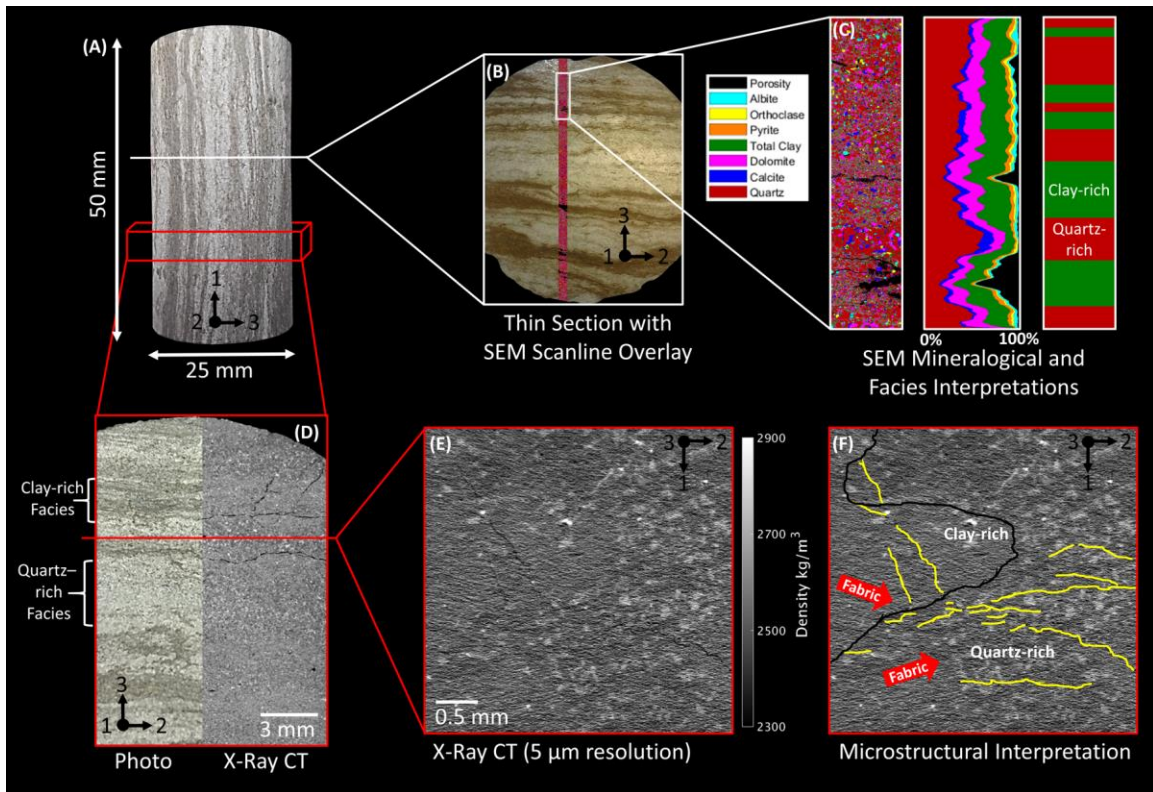


Figure 7-2 Evidence of layering, fractures, and rock fabric in the same sample at different scales. (A) Image of Mancos core with bedding at 90°, (B) photograph of thin section from center of the core with SEM scanline overlain (red), (C) sub-section of SEM scanline colored by the identified mineral phase, and associated mineralogy log showing volume % of minerals along the scanline, (D) comparison of photograph and 13 μm resolution X-ray CT scan of the same sub-section of the core, (E) 5 μm resolution X-ray CT scan, (F) annotated version of E, showing the interpreted facies boundary (black line), fabric direction (blue arrows), and interpreted fractures (yellow lines).

Table 7-2 Major minerals present in Mancos Shale and their respective mass density (ρ), bulk (K) and shear (μ) moduli. In order from left to right, quartz, calcite, dolomite, kaolinite, illite, smectite, pyrite, orthoclase, albite. Endmember mineralogical composition (volume %) of quartz-rich (light) and clay-rich (dark) facies from SEM-EDS analysis. Total clay is the sum of kaolinite, illite, and smectite. Volume fraction is the volume percent of each layer in the SEM images. Average density (ρ) and Effective bulk (K) and shear (μ) moduli are calculated from the volume % of each mineral and their mineral density or moduli.

Minerals	Qtz	Cal	Dol	Kaol	Ill	Smec	Pyr	Orth	Alb					
Mass Density ρ (kg/m ³)	2650	2710	2870	2440	2600	2400	5010	2640	2610					
Bulk Modulus K (GPa)	37	70	80	46	45	9.5	140	65	55					
Shear Modulus μ (GPa)	41	28	45	22	20	6.9	125	30	30					
Facies Types	Volume % of Each Mineral									Total % Clay	Volume %	Eff K (GPa)	Eff μ (GPa)	Avg ρ (kg/m ³)
Quartz-rich	52.5	16.1	11.4	5.3	7.6	0.1	1.6	1.8	1.1	13	64	46.9	35	2663
Clay-rich	14.9	4.9	19.3	10.2	30	6	4.7	1.6	3.2	46.2	36	47	28	2614

7.3.3 Structural Variability from X-ray Micro-Computed Tomography

X-Ray micro-computed tomography (CT) images provide insight into the degree to which variations in lithology (i.e. quartz- vs clay-rich layers) relate to variations in X-ray attenuation/transmission (CT number), which depends on electron and mass density. Comparison between a photograph and a 13 μm resolution CT image of a Mancos sample shows that the light colored and quartz-rich facies generally appears slightly duller (lower CT number) than the darker colored and clay-rich layers (Figure 7-2-D). However, these dull quartz-rich layers are abundant in bright spots, whereas clay-rich layers exhibit fewer and smaller bright spots. Bright spots are possibly related to calcite and dolomite with a small amounts of pyrite, which have higher levels of X-ray attenuation (CT number), due to their higher mass densities. Because quartz and most of the clay minerals present in the sample are known to have very similar mineral densities, the background variation in CT number between the major facies might be due to variations in porosity or the relative

abundance of denser secondary carbonate minerals. For example, clay-rich facies are marginally brighter than the quartz-rich facies. Therefore, the increased brightness could be due to a decrease in intergranular porosity with increasing clay content, or the increased amount of dolomite. SEM and CT imaging confirm the presence of fractures close to interfaces between the quartz-rich and clay-rich facies, and higher density of fractures in clay-rich layers than in quartz-rich layers (Figures 7-2-C and 7-2-D).

Figure 7-2-E shows a 5 μm resolution CT scan of a sub-section of the same Mancos Shale sample in Figure 7-2-D, which reveals more details about the rock microstructure than images at 40 μm . Figure 7-2-F shows annotations of a few key microstructural interpretations. First, the rock exhibits a distinct fabric due to the alignment of oriented grains, which in general appears to trend left to right in the image, with a slight counter-clockwise rotation when moving from the clay-rich facies in the left-center of the image to the quartz-rich facies surrounding it. Fractures within the rock also seem to re-orient due to the change in facies type and fabric orientation. Fractures also appear more continuous in the clay-rich facies, whereas quartz-rich facies exhibit fractures which tend to end abruptly and appear as fabric-parallel fracture sets. The fractures also appear to re-orient around the carbonate-grains. Because Mancos Shale samples exhibit a distinct fabric, and the fabric appears to play an appreciable role in dictating micro-fracture orientation, it is likely that the fabric also contributes to the measured velocity anisotropy.

7.4 METHODS FOR CONSTRUCTING MINERALOGICALLY AND STRUCTURALLY HETEROGENEOUS VELOCITY MODELS

7.4.1 Combining SEM and CT Imaging Results

The SEM and CT results were combined to construct density and velocity models which capture the mineralogical and structural heterogeneity of Mancos Shale samples. First, SEM Energy Dispersive X-Ray Spectroscopy (EDS) maps of major elements (Al, Ca, Fe, K, Mg, Na, and Si) were overlain to quantify mineralogy and identify mineralogical variations across the sample (Figure 7-3). SEM Back-scattered Electron detection (BSE) maps were also used to differentiate between minerals with similar elemental compositions. Results were used to quantify the mineralogical compositions of the quartz-rich and clay-rich endmember facies. To test the impact of mineralogical variations on velocity anisotropy, a “Synthetic” layered model was constructed by populating a perfectly layered model with the mineralogical properties and volume fractions of the dominant facies (Table 7-2). This provided a baseline prior to adding the structural complexity from the CT imaging. Details of SEM and CT imaging are provided in Chapter 2.

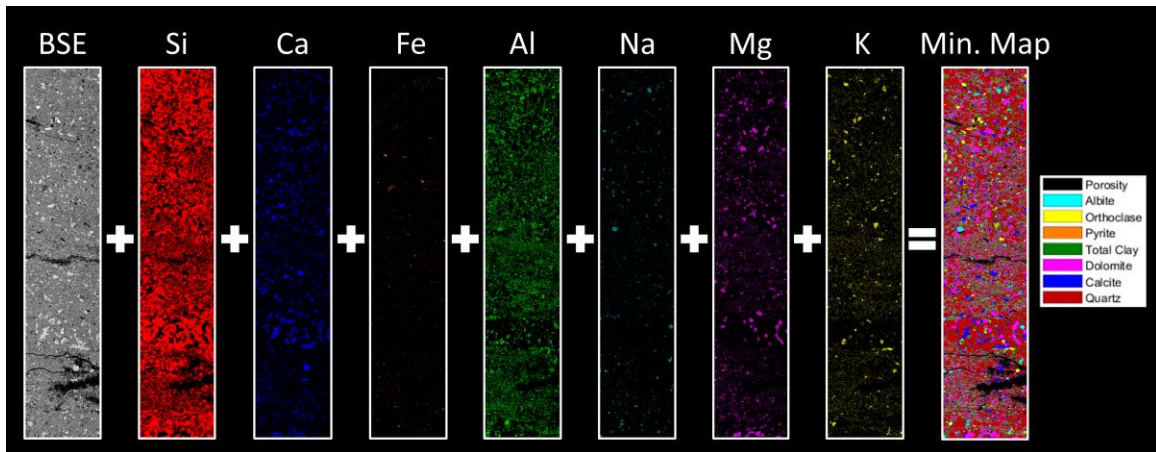


Figure 7-3 Workflow for determining mineralogy map (Min. Map) from SEM-derived Back-scatter Electron (BSE) map and elemental maps of Silica (Si), Calcium (Ca), Iron (Fe), Aluminum (Al), Sodium (Na), Magnesium (Mg), and Potassium (K). Element maps were overlain to determine mineral locations, e.g. areas where Mg and Ca overlap were assumed to represent dolomite.

Several models were generated by using the imaged CT volumes as the model domain in order to preserve the spatial changes in lithology and structure. Figure 7-4 shows the workflow for transforming CT scans into density and then velocity models. Samples were scanned alongside several objects with known density in order to help constrain the relationship between CT number and density (Figures 7-4-A and 7-4-B). The relationship between CT number and density was applied to each CT volume to generate maps of mass density (Figure 7-4-C). A density threshold was then used to spatially separate the two major facies (quartz- and clay-rich) (Figure 7-4-D). Effective mechanical properties of each layer (bulk and shear elastic moduli) were then estimated based on the SEM-derived mineralogical compositions, mineral moduli, and assumed values of grain aspect ratios to account for non-spherical grains such as clays (Table 7-2) (Berryman 2005). Individual mineral moduli represent average values of several reported values (Wang et al. 2001, Mavko et al 2009). Variations in aspect ratio did not have a noticeable impact on the model,

thus conservatively estimated values of 1 and 0.1 were assigned to non-clay and clay minerals, respectively.

Due to the fine-grained nature of shales, it is difficult to discern and accurately segment shale grains from the pore space. Therefore, a segmentation-less method was used to account for porosity (bulk density) variations within the samples (Tisato and Spikes 2016, Goldfarb et al. 2017). A density-to-porosity conversion curve was used to estimate the porosity of each voxel from the CT-derived density maps. Air ($0 \text{ kg/m}^3 = 100\%$ porosity) and dolomite ($2870 \text{ kg/m}^3 = 0\%$ porosity) were used as lower and upper bounds for the conversion, respectively. A null porosity was assigned to any voxel with a higher mass density than dolomite. All voxels were assigned a porosity value and a mineralogical composition from either the quartz- or clay-rich layer endmembers. The Modified Voigt-Reuss-Hill (MVRH) effective medium theory was then applied to each voxel to adjust its effective shear and bulk moduli based on the estimated porosity (Hill 1952, Nur et al. 1998). The MVRH bulk and shear moduli were used to calculate the *P*- and *S*-wave velocities for each voxel within the CT volume (Figures 7-4-E and 7-4-F).

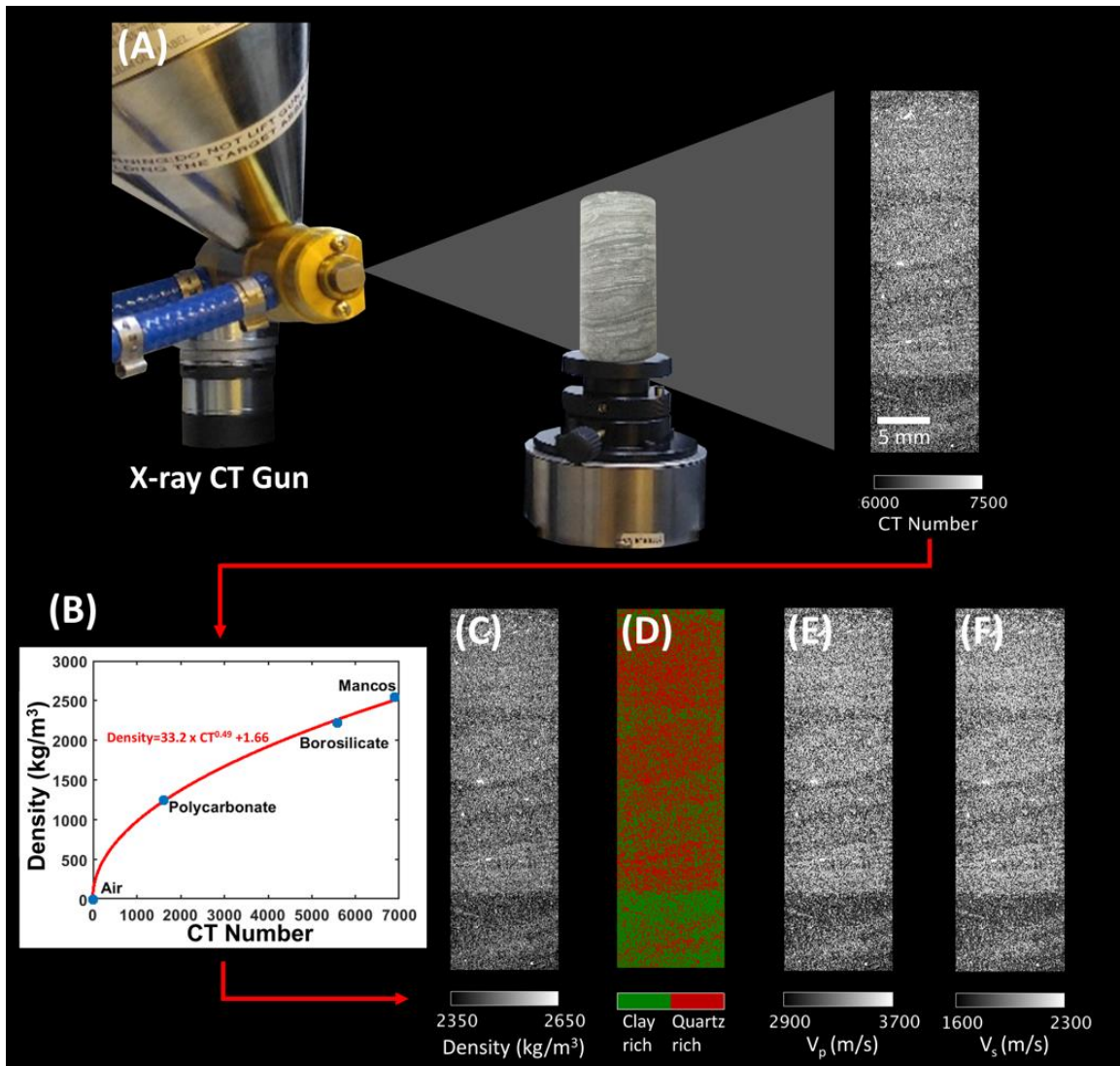


Figure 7-4 Workflow for creating velocity models from X-ray micro CT scans. (A) X-ray CT gun (left) scans sample (middle) resulting in the map of CT Number (right). (B) A relationship is developed between the average CT number and known density for the sample and reference objects (Air, Polycarbonate, and Borosilicate), which are also scanned with the sample. (C) A density map is created from the map of CT number. (D) A cutoff density is selected to differentiate between the clay-rich (green) and quartz-rich (red) facies determined by SEM analyses. The average mineralogical compositions and associated elastic properties (Table 7-2) are assigned to each facies and scaled based on their relative density (porosity) using the Modified Voigt-Reuss-Hill effective medium theory to develop maps of (E) V_p and (F) V_s .

In addition to using the CT images as model domains, SEM images were also used to investigate wave propagation at a higher resolution. However, because many individual grains and pores were discernable in the SEM models, the MVRH model was not used. Instead the previously identified mineral grains were segmented and assigned reference values of density and velocities, and pores were treated as air (Table 7-2).

All CT and SEM models were constructed to capture the mineralogical and structural features (i.e. layering, fractures, etc.) that are presumed to contribute to the *P*-wave velocity anisotropy (432 m/s) and the *S*-wave velocity anisotropy (242 m/s) of Mancos Shale (Table 7-3). Velocity anisotropy is defined as $(V_{90^\circ} - V_{0^\circ}) / V_{0^\circ}$, where V_{0° and V_{90° represent the wave velocities perpendicular and parallel to bedding, respectively. We simulated wave propagation perpendicular and parallel to these features in order to determine their impact on velocities and overall macroscopic anisotropy.

Table 7-3 *P*- and *S*-wave velocities, volume average densities ($\langle\rho\rangle$), and velocity anisotropies from experimental measurements (Exp) and simulation results. Velocity anisotropy is defined as $(V_{0^\circ} - V_{90^\circ}) / V_{90^\circ}$, where V_{0° and V_{90° represent the wave velocities parallel and perpendicular to bedding, respectively. Models are shown in the following figures: 40 μm resolution core-scale CT model (40 μm _Core) (Figure 7-4, 7-6), synthetic layered model (Synthetic) (Figure 7-5), CT model at 13 μm focused on layering (13 μ _Layer) (Figure 7-6-C), fractures (13 μ _Frac) (Figure 7-6-D), and encompassing both (13 μ _All) (Figure 7-6-B), and SEM models focused on layering (SEM_Layer) (Figure 7-7-D and E) and fractures (SEM_Frac) (Figures 7-7-B and C). Densities do not vary for the 13 μm CT or SEM models because the same physical model is used for wave propagation, but is rotated to simulate the 0° and 90° bedding/fractures. SEM models are constructed using the actual mineral velocities and densities, whereas the CT models use the MVRH effective medium theory to determine effective elastic properties and velocities.

Dataset Name	V_p (m/s)	V_s (m/s)	$\langle\rho\rangle$ (kg/m ³)	V_p anisotropy (m/s)	V_s anisotropy (m/s)
Exp_0°	3058	2150	2673	437	232
Exp_90°	3495	2382	2666		
CT 40 μm _Core_0°	2956	1901	2477	42	32
CT 40 μm _Core_90°	2998	1933	2484		
Synthetic_0°	3448	2113	2645	64	109
Synthetic_90°	3512	2222	2645		
CT 13 μm _Layer_0°	2649	1700	2518	31	18
CT 13 μm _Layer_90°	2680	1718	2518		
CT 13 μm _Frac_0°	2320	1575	2543	95	100
CT 13 μm _Frac_90°	2415	1675	2543		
CT 13 μm _All_0°	2702	1725	2525	98	109
CT 13 μm _All_90°	2800	1834	2525		
SEM_Layer_0°	3600	2420	2659	300	130
SEM_Layer_90°	3900	2550	2659		
SEM_Frac_0°	3520	2380	2574	375	188
SEM_Frac_90°	3895	2568	2574		

7.4.2 Wave Propagation Modeling

Once mass density ρ , V_p , and V_s models were constructed from the various CT and SEM scans, elastic wave propagation was numerically simulated using the software Seismic mOdeling with FInite differences (SOFI-2D), which is a 2D viscoelastic time domain parallel modeling code for P - and S -waves (Bohlen 2002). The finite differences code is 8th order in the time domain and 2nd order in the space domain, and explicitly solves for pressure and particle velocity for each time step. In order to mimic the quartz piezoelectric transducers used to measure ultrasonic velocities in the laboratory, the seismic source and receiver elements in the SOFI-2D were placed within simulated endcaps that have the density and velocity properties of quartz (Figure 7-5). Each model was sub-divided into elements the size of the model resolution (e.g. 0.9 μm for SEM-derived models), and models were surrounded by a 30 element thick air boundary to mimic the unconfined conditions. An attenuation factor of 8% was applied to the air boundaries (and 0% elsewhere) in order to dampen waves exiting the model domain and avoid reflections back into the area of interest. Elastic waves were simulated using a plane wave Ricker wavelet source function at a central frequency of 1 MHz (the central frequency of the ultrasonic transducers), and P - and S -waves were respectively mimicked by imposing vertical and horizontal displacements on the source elements, then we evaluated the seismograms of vertical and horizontal displacements recorded at the receivers elements. The seismograms for each simulation and wave type were merged together to represent an average wave trace and first arrivals were picked using an algorithm detecting changes in the slope of the seismogram. The sensitivity of the algorithm was adjusted for S -waves in

order to avoid detecting the small amounts of *P*-wave noise present in the seismograms (Figure 7-5). We assume wave propagation behaves similar to the effective medium limit (long wavelength with respect to scale of heterogeneity) because all models have a resolution (element size) at least 100 times smaller than the wavelength (Backus 1962, Marion et al. 1994).

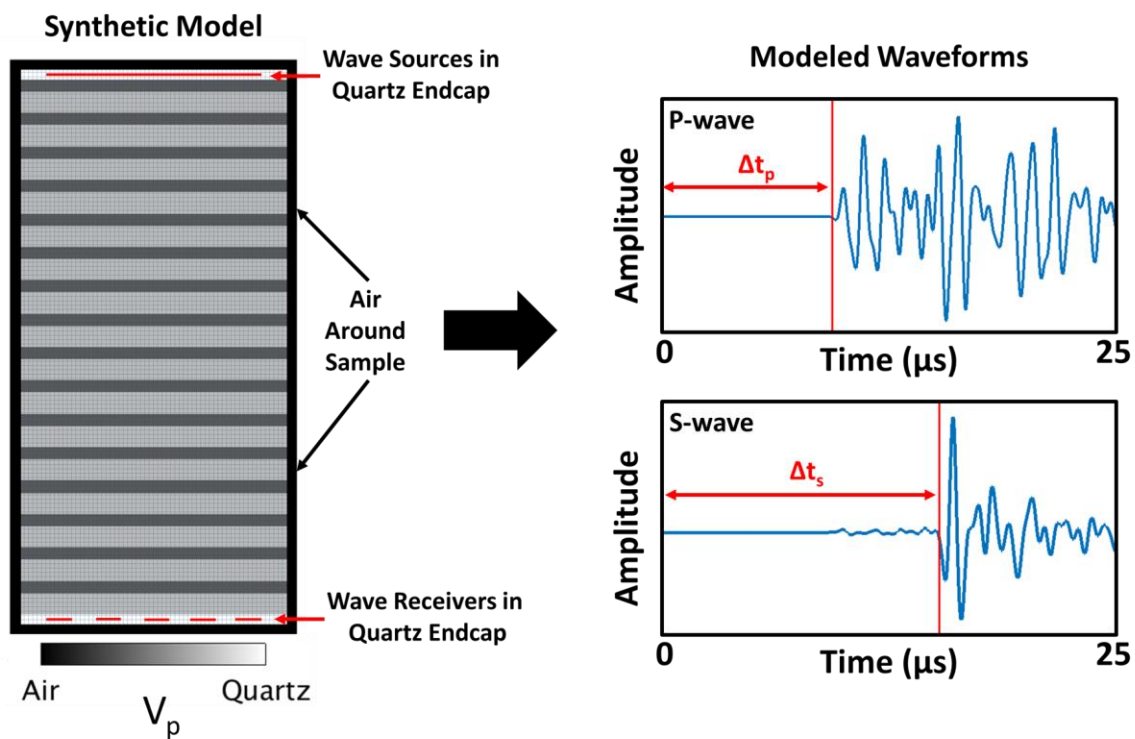


Figure 7-5 (Left) Example of the Synthetic V_p model with 0° bedding orientation and wave propagation perpendicular to bedding. Sources and receivers are placed in quartz endcaps in order to mimic the quartz piezoelectric transducers used in laboratory experiments, and the whole domain is surrounded by a wave-damping air boundary. Models are discretized to grid blocks the size of the resolution of the images from which they are derived (i.e. $40\mu\text{m}$ and $13\mu\text{m}$ for CT models, and $0.9\mu\text{m}$ for SEM models). (Right) The modeled *P*- and *S*-waveforms from the simulation, with Δt representing the travel time for the wave through the sample before reaching the receivers. Velocities are calculated from the travel times.

7.5 RESULTS AND ANALYSIS

7.5.1 Synthetic Layered Models

Figure 7-5 shows the Synthetic model constructed to test the effects due to layering of endmembers without structural variability. The V_p and V_s of the Synthetic models were 112% and 99% of the experimental velocities with bedding at 0°, and 100% and 93% with bedding at 90°, respectively (Table 7-3 and Figure 7-9). The Synthetic model also exhibited 13% and 48% of the experimental V_p and V_s anisotropy, respectively (Figure 7-10). The higher anisotropy in V_s than in V_p is likely due to the effective shear moduli of the quartz-rich facies being 7 GPa higher than clay-rich facies, whereas the effective bulk moduli of the two facies only differ by 0.1 GPa (Table 7-2). Overall, results from the synthetic example show that our simple two facies model predicts velocities within 12% of the experimental measurements; however, these results show that the 14.3% and 10.8% V_p and V_s anisotropy measured in the laboratory is unlikely to be caused solely (or even predominantly) by layering. Because layering alone could not reproduce the experimentally measured anisotropy, we also tested models which incorporated the structural complexity observed in Mancos samples using CT imaging.

7.5.2 CT Models of Oriented Cores

Figure 7-6 shows the V_p models of the Mancos Shale cores from which the experimental velocities were measured. These Core models were developed from 40 μm resolution CT scans and the results are shown in Table 7-3 and Figure 7-9. V_p and V_s of the

Core models were 97% and 89% of the experimental velocities with bedding at 0°, and 86% and 81% with bedding at 90°, respectively (Table 7-3 and Figure 7-9). It is important to notice that the distinct color variations between the quartz-rich and clay-rich facies in Figure 7-2 do not necessarily relate to dramatic differences in density or velocity. Therefore, the resulting amount of velocity anisotropy from the model is fairly low, with V_p and V_s anisotropy being roughly 10% and 15.6% of those measured experimentally (Figure 7-10). Although the Core model exhibited relatively low anisotropy, the velocities in the 0° model were within 11% of the experimental values, but the 90° model were off by as much as 19%. Because the 40 μm Core models did not capture the experimental anisotropy, we tested smaller scale and higher resolution models to evaluate the impact of fractures and other microstructural features on the P - and S -wave velocities.

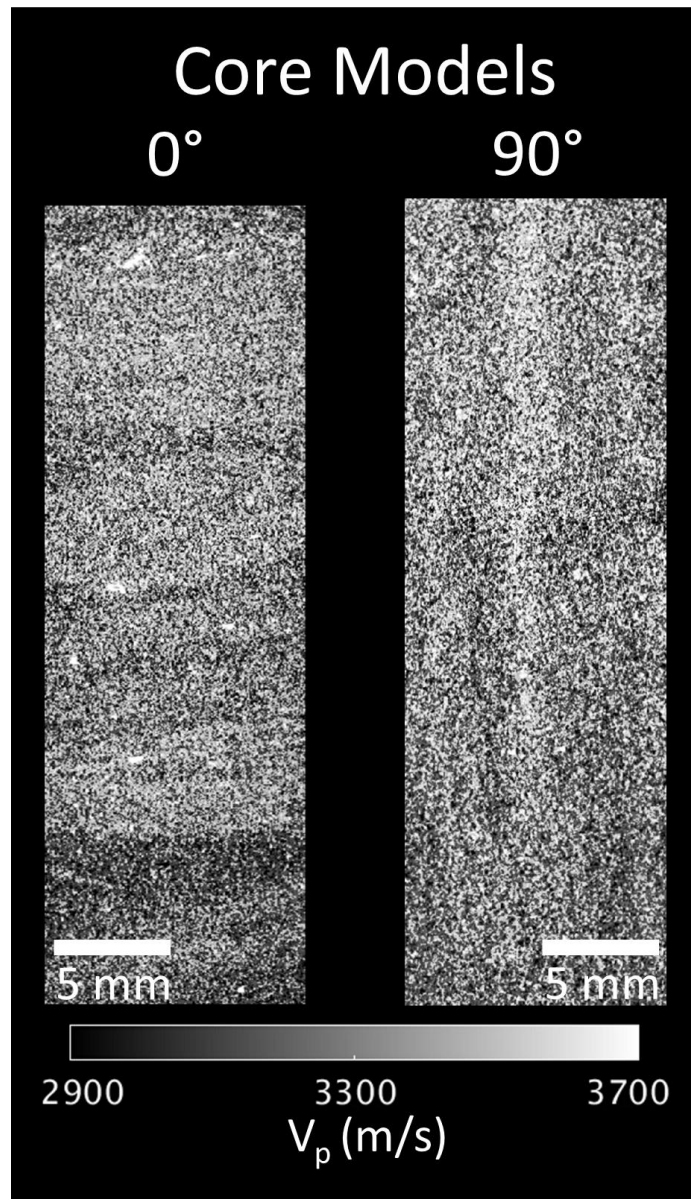


Figure 7-6 P-wave velocity models derived from 40 μm resolution CT scan of Mancos Shale cores with bedding at 0° (left) and 90° (right). Model results listed in Table 7-3 as Core_0° and Core_90°.

7.5.3 CT Models at 13 μm Resolution Testing the Impacts of Layering and Fractures

Figure 7-7-A shows the V_p map from the rock sample in Figure 7-2 derived from a CT scan at 13 μm resolution. Figures 7-7-B, 7-7-C, and 7-7-D show the subsections of the sample tested to evaluate the impacts of layering and fractures on velocities and anisotropy at this higher resolution. The subsection in Figure 7-7-C shows model “13 μm _Layer”, which exhibits distinct bedding but does not have visible fractures. Contrary to the Core simulations, this model contains some distinctly oriented pores and visible carbonate cements. Despite the additional microstructural details captured at higher resolution, V_p and V_s of the 13 μm _Layer model were only 87% and 79% of the experimental velocities with bedding at 0°, and 77% and 72% with bedding at 90°, respectively (Table 7-3 and Figure 7-9). The resulting V_p and V_s anisotropy was 8.2% and 9.8% of the experimental values, which are the lowest of all our tested models.

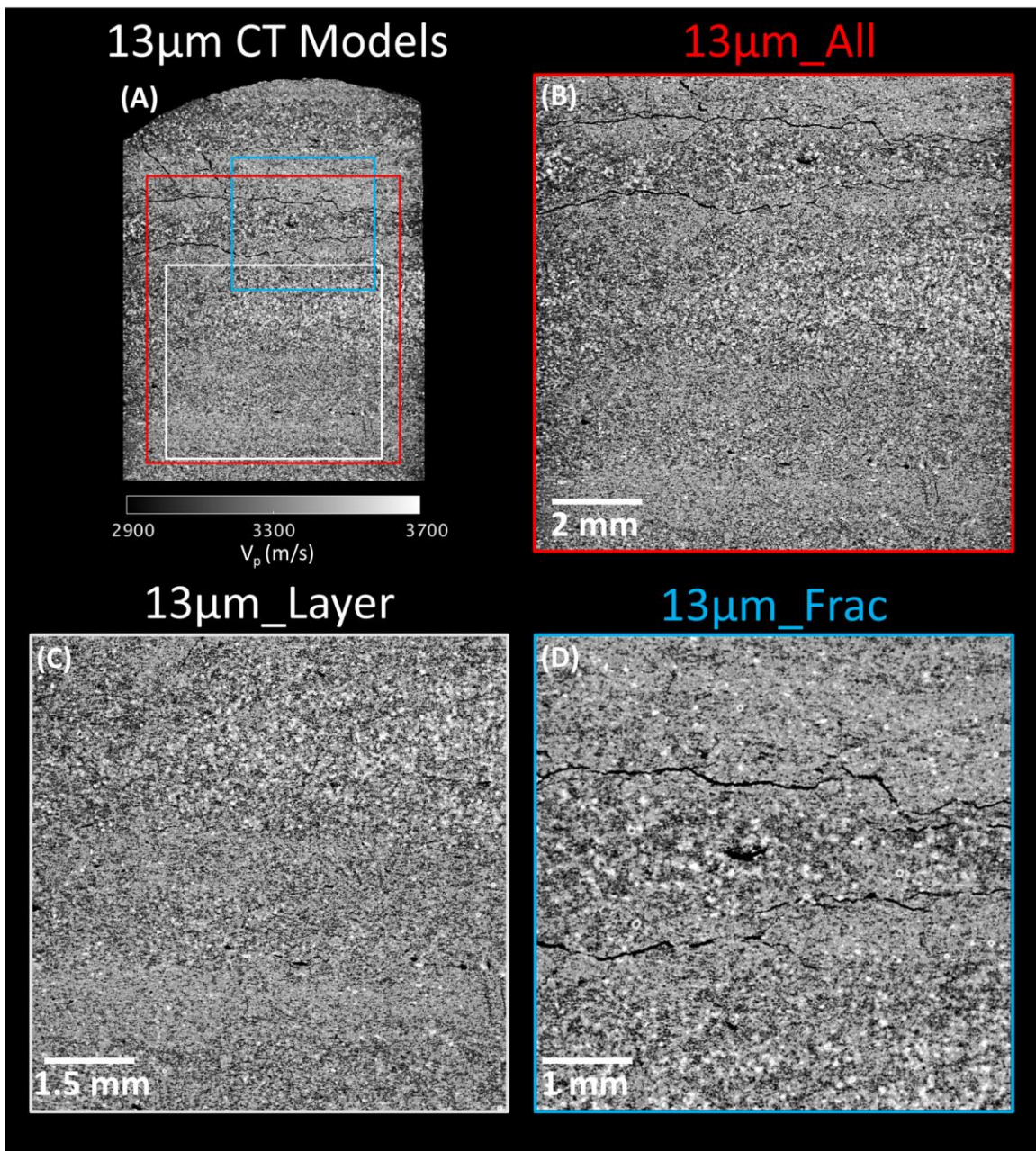


Figure 7-7 *P*-wave velocity models derived from 13 μm resolution CT scan of Mancos Shale shown in Figure 7-2-D. (A) Whole model from which subsections B-D were taken, (B) larger scale model to test the combined effects of C and D on velocity anisotropy (C) model used to test impact of layering, and (D) model used to test the impact of fractures. Model results listed in Table 7-3 as 13μm_All (B), 13μm_Layer (C), and 13μm_Frac (D).

Figure 7-7-D shows the “13 μm _Frac” model, which tested the impact of fractures by comparing wave propagation parallel and perpendicular to the prominent bed-parallel fractures. As expected, modeled velocities decreased with the addition of fractures. V_p and V_s were 76% and 74% of the experimental velocities with bedding/fractures at 0°, and 69% and 70% with bedding/fractures at 90°, respectively (Table 7-3 and Figure 7-9). Results show that V_p and V_s anisotropy increased, however, to 28.6% and 58.8% of the experimental measurements, indicating that fractures have an impact on velocity anisotropy, particularly for V_s . It should be noted that because fractures tend to form along bed boundaries, these anisotropy values are likely a combination of the effects of layering and fractures. Variations in fracture orientation would likely influence the measured anisotropy. Despite their seemingly open appearance in the 2D models, 3D volumes show that fractures faces often exhibit asperities, which have frictional stiffness. Fractures also exhibit finite strength, which allows samples to remain intact without confinement. Therefore, the fractures in the 13 μm CT models were given the V_p and mass density of air (335 m/s, and 1.225 kg/m³), but a non-zero V_s (110 m/s) to account for fracture shear stiffness.

Figure 7-7-B shows model 13 μm _All, which captures most of the sample in Figure 7-7-A and incorporates both the layering and fractures in the 13 μm _Layer and 13 μm _Frac models. The resulting V_p and V_s increased to 88% and 80% of the experimental velocities with bedding/fractures at 0°, and 80% and 76% with bedding/fractures at 90°, respectively (Table 7-3 and Figure 7-9). V_p anisotropy decreased slightly from the 13 μm _Frac model (28.6%) to 25.4% and V_s anisotropy was roughly the same at 58.5% of the experimentally

measured anisotropy. Overall the 13 μm _All model results show that incorporating both layering and fractures at higher resolution improves the accuracy of velocities and increases anisotropy. However, anisotropy is still significantly lower than the experimentally measured anisotropy.

7.5.4 SEM Models at 0.9 μm Resolution Testing the Impacts of Layering and Fractures

Figure 7-8-A shows the 0.9 μm SEM scan-line from which the models SEM_Layer and SEM_Frac were derived to test the impacts of layering and fractures, respectively. Figures 7-8-B to 7-8-E compare the mineralogy and V_p maps for the SEM derived models. The unfractured SEM_Layer model exhibited higher V_p and V_s , which were 117% and 113% of the experimental velocities with bedding at 0°, and 111% and 107% with bedding at 90°, respectively (Table 7-3 and Figure 7-9). The resulting V_p and V_s anisotropies were 58.3% and 49.8% of the experimental values, respectively. The V_p anisotropy was over twice as large as the highest value for the CT-derived models. However, the V_s anisotropy was lower than the 13 μm _Frac and 13 μm _All models, both of which were roughly 58.5%.

Figures 7-8-B and 7-8-C show the SEM_Frac model, which exhibits a distinct fracture and some larger pores oriented relatively parallel to bedding. Model results show slightly lower V_p and V_s than the SEM_Layer model with bedding/fractures at 0° (115% and 111% of the experimental velocities), and slightly higher V_p and V_s with bedding/fractures at 90° (114% and 109%), respectively (Table 7-3 and Figure 7-9). Furthermore, V_p and V_s anisotropy increased with the addition of fractures and was 74.5%

and 73.2% of the laboratory measurements, respectively. Overall, SEM models exhibit the highest velocities, which were similar for the SEM_Layer and SEM_Frac models. V_p and V_s anisotropies also increased significantly for the SEM-derived models, particularly for SEM_Frac, which included both layering and fractures.

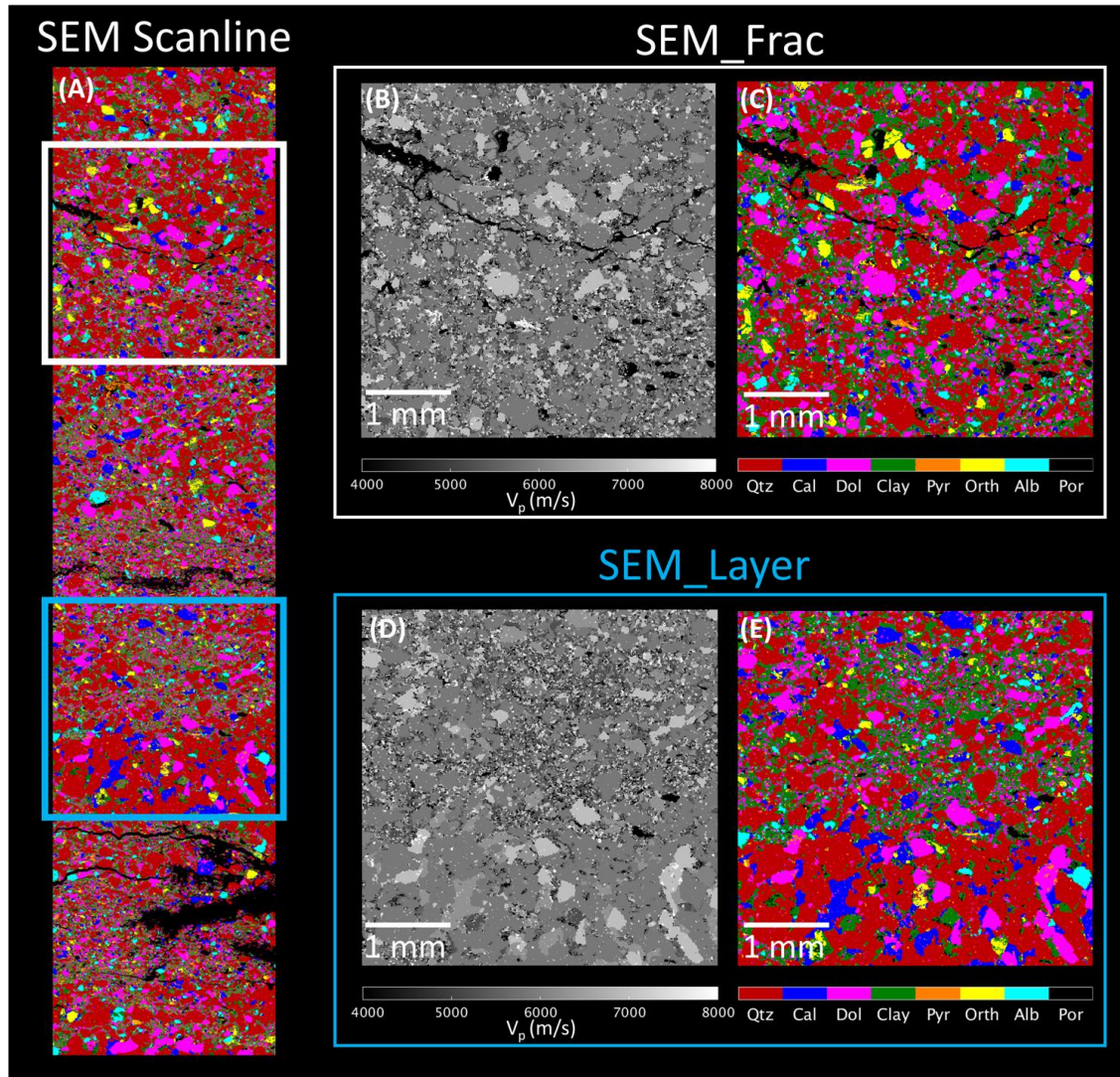


Figure 7-8 SEM mineralogy maps and P -wave velocity models derived from $0.9 \mu\text{m}$ resolution SEM scanline shown in Figure 7-2-C. (A) Top of model from which subsections B-E were taken, (B) V_p model of SEM_Frac used to test impact of fractures, (C) mineralogy map of SEM_Frac, (D) V_p model of SEM_Layer used to test the impact of layering, and (E) mineralogy map of SEM_Layer. Model results listed in Table 7-3 as SEM_Frac (B, C) and SEM_Layer (D, E).

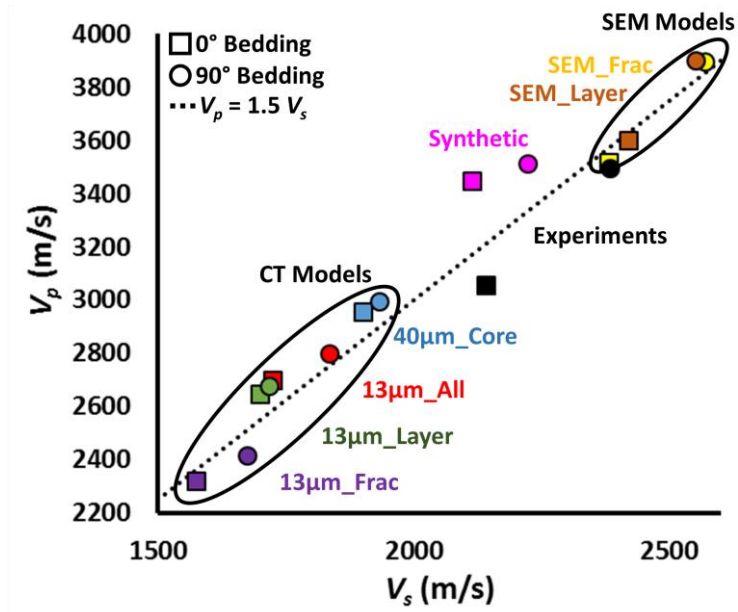


Figure 7-9 Comparison between the P - and S -wave velocities from experimental and modeled results. Squares represent results from wave propagation with layering at 0° and circles are for layering at 90° . Dashed line represents a V_p/V_s ratio of 1.5.

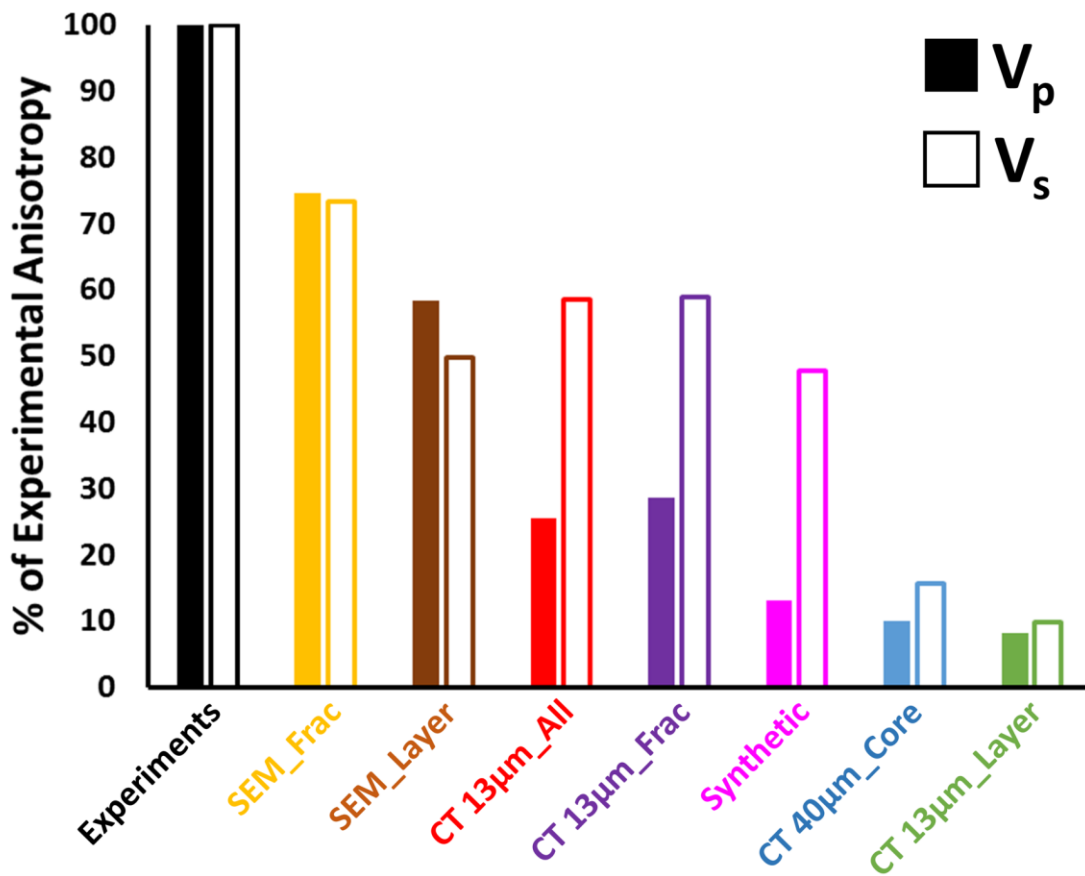


Figure 7-10. Comparison of the percent of P -wave (filled bar) and S -wave (checked bar) anisotropy from the various models normalized to the experimental measurements. Velocity anisotropy is defined as $(V_{90^\circ} - V_{0^\circ}) / V_{0^\circ}$, where V_{0° and V_{90° represent the wave velocities perpendicular and parallel to bedding, respectively. P - and S -wave velocities and the absolute anisotropies are shown in Figure 7-9 and summarized in Table 7-3.

7.6 DISCUSSION

7.6.1 Impact of Model Type on Velocities

Modeled velocities in Table 7-3 and Figure 7-9 range between 69% and 117% of their equivalent experimental measurement. This range is wide, yet the focus of this study is not to match the absolute velocities but to evaluate velocity anisotropy. Furthermore, the

relative error in velocities appears to be specific to the scale and type of the model tested. For example, the SEM models account for 3 of the 4 results with higher P -wave velocities than the experiments, and the Synthetic model is almost a perfect match parallel to bedding (90°), but is 112% of the experiment perpendicular to bedding (0°). In contrast to the SEM models, the CT derived models all exhibit lower velocities than those measured experimentally. Finally, we simulate wave propagation in 2D, which could also contribute to the velocity mismatch when compared to the 3D laboratory measurements.

SEM models provide the closest estimates of the 14.3% and 10.8% V_p and V_s anisotropy measured in the laboratory. The increased anisotropy of the SEM models likely originate from two sources: the high resolution of the SEM (discussed in the next section) and the use of individual mineral properties (velocities and densities) rather than assuming a two-layer system. By identifying minerals and assigning their properties separately, the SEM models accounted for the small scale mineralogical and structural heterogeneity that was missed when using the average endmembers to represent the two facies in the CT models. Therefore, although CT models were able to capture the larger scale layering, the use of the two endmember facies hindered accounting for lithological variability.

Although results show a range of velocities from the various models, all of our simulations exhibit V_p / V_s ratios around 1.46, which is consistent with experimental values of 1.43-1.48 (Figure 7-9). In the absence of fluids, changes in V_p / V_s ratio is related to lithology (Tatham, 1982, Castagna et al 1985, Mavko et al 2009). The relatively low V_p / V_s ratios observed are indicative of quartz-rich lithologies such as tight sandstones and siltstones (Mavko et al. 2009). This is consistent with our SEM analyses, which revealed

that these rocks are extremely quartz-rich, even within the darker and more clay-rich layers. Therefore, the good match of V_p / V_s ratios provides validation for modeling and capturing the important lithologic characteristics that influence wave propagation in the laboratory.

7.6.2 Impact of SEM Resolution on Velocities

The relatively high resolution of SEM-derived models allowed us to capture the intricate mineralogical layering, boundaries and orientations of major grains and pores, and some micro-scale fractures. All of these features likely play a measurable role in the higher velocity anisotropy of the SEM-derived models. Despite the relatively high resolution, many microstructural features were not incorporated into the models. For example, the relatively fast velocities in the SEM models can be attributed partly to the inability of the SEM to image much of the existing micro-porosity at this resolution. Higher resolution SEM images exhibit porosity at grain boundaries and within the clay-rich layers, whereas the 0.9 μm resolution SEM models show most grains in perfect contact with one another and only identify larger-scale pores and fractures. The stress dependence of velocities observed in the laboratory provides additional evidence for the important impact that these compliant grain boundaries and microfractures ($< 5\mu\text{m}$) have on velocity anisotropy (Figure 7-1) (Anders et al. 2014). Although we did not incorporate much of the grain boundary porosity or microfractures in the numerical simulations, the mass densities of the SEM models were very similar to experimental measurements (Table 7-3). Therefore, the addition of these features (as porosity) would require increased density elsewhere in the model (i.e. unidentified denser mineral phases) to maintain a realistic overall mass density.

7.6.3 Impact of CT Resolution on Velocities

The velocity mismatch between experiments and CT models increases with decreasing model size, increasing resolution, and more so in the direction parallel to bedding. For example, the 40 μm resolution Core models are 22% closer to the experimental V_p than the 13 μm _Frac model. The increased velocity mismatch with decreasing model size is intuitive because the smaller models are less likely to capture the range of mineralogical and structural heterogeneity observed in Mancos Shale. This behavior is further evidenced by comparing the 13 μm models. The smaller 13 μm _Frac model exhibited higher anisotropy and lower velocities likely due to the disproportionate amount of fracture porosity and lack of higher velocity carbonates, respectively. The opposite is true for the 13 μm _Layer model, which exhibited higher velocities but very little anisotropy. However, when these two models were incorporated into the 13 μm _All model, both higher velocities and increased anisotropy were preserved.

The decreased velocities in the higher resolution CT models could also point to limitations for estimating elastic properties using the segmentationless method and Modified Voigt-Reuss-Hill (MVRH) effective medium theory (Goldfarb et al. 2017). In the 40 μm resolution Core model, MVRH successfully accounted for the lack of discernable porosity by modifying mechanical properties based on the calibrated CT-derived mass density (Figure 7-4). However, at a higher resolution some larger pores and fractures were visible and modeled as low velocity zones, which further decreased the overall velocity of the 13 μm models. Additionally, the segmentationless method may be more accurate in monomineralic lithologies such as sandstone, where variations in density

are associated directly with variations in porosity, rather than the complex variations in mineralogy observed in Mancos samples. Relating density variations with mineralogical changes is not straightforward, and the simplification of Mancos samples as having only two facies in our CT models could have also caused the decreased velocity results. For example, the higher resolution CT models highlighted the complex spatial variability of the carbonate minerals within the quartz- and clay-rich facies, which likely challenges the validity of our assumption of two dominant facies. Therefore, in the future carbonates could potentially be modeled as their own facies, which would likely increase the overall velocities of the high resolution models. Despite the lower velocities at higher resolution, the ability to more accurately capture the lithological variability allowed the 13 μm models to exhibit higher densities than the 40 μm Core models, but still appreciably lower than the experimental, SEM, and Synthetic models (Table 7-3).

7.6.4 Insights into the Controls on Shale Velocity Anisotropy

The Synthetic and CT models results showed that layering alone contributes less than 13% of the experimentally measured V_p anisotropy. Furthermore, CT models capturing sample layering and fractures account for a maximum of 28.6% and 58.8% of the experimental P - and S -anisotropy, respectively. Therefore, the anisotropy of Mancos Shale is likely due to different microstructural features, including microfractures, clay-rich rock intrinsic anisotropy. Our SEM models showed the intricate mineralogical layering and micro-scale fractures associated with fabric, which resulted in higher amounts of anisotropy. Our CT models did not exhibit high enough resolution to capture these

microstructural features, and higher resolution models would likely limit the application of the segmentationless method used in this study. In addition to the fabric and associated micro-fractures shown in Figure 7-2, the intrinsic anisotropy of oriented clays also could not be captured with any of our models. Accounting for these features would likely have an appreciable impact on velocity results, particularly parallel to bedding, and may provide the answer to why our models exhibit lower anisotropy than the experimental measurements. However, directly capturing the structural distribution of fabric and micro-fractures in our models would require CT imaging at significantly higher resolutions. The orientation of fabric can also be estimated from high resolution SEM imaging or through use of X-ray texture goniometry (Valcke et al. 2006). Furthermore, accounting for rock fabric and the intrinsic anisotropy of layered clays would require wave propagation software which allows for anisotropic elements and discerning fabric and clay intrinsic anisotropy. Such estimation could be obtained theoretically from the estimated orientation and abundance of the various clay mineral phases present in the sample (Mainprice and Humbert 1994, Mainprice et al. 2011).

7.7 CONCLUSIONS

We utilized SEM and CT scanning to develop elastic models which honor the structural and mineralogical heterogeneity of Mancos Shale at several scales. The impacts of mineralogical layering and fractures on velocity anisotropy were investigated by simulating *P*- and *S*-wave propagation perpendicular and parallel to these features within each model. The following conclusions are a result of this work.

- A simplified mineralogy model consisting of two endmember facies (quartz-rich and clay-rich) is adequate for estimating velocities using CT-derived models at the core scale. However, CT-derived models at higher resolutions exhibit decreased accuracy, likely due to limitations in the segmentationless method when individual grains and pores are visible at high resolution. Furthermore, additional velocity error arises from converting variations in mass density into variations in lithology and thus V_p and V_s , where we simplify the complex mineralogy of Mancos Shale into 2 facies.
- SEM scale models containing layering and fractures account for 74.5% and 73.2% of the experimentally measured P - and S -wave anisotropy compared to CT models which at most exhibit 28.6% and 58.8%, respectively. More detailed mapping of mineral phases and their spatial distribution likely caused SEM models to exhibit higher anisotropy than CT models.
- Modeled velocities ranged between 69% and 117% of their experimental equivalent, however, large variations in model resolution (40 to 0.9 μm) and type (SEM vs CT) accounted for the seemingly large range. Despite the velocity spread, modeled V_p / V_s ratios cluster around 1.46, which is consistent with the experimental values of 1.43-1.48, and typical values for quartz-rich rocks.
- Modeled wave propagation perpendicular to bedding more closely captures the experimental velocities than parallel to bedding. The likely cause for the relatively larger mismatch between modeled and measured velocities parallel to bedding and resulting in overall lower velocity anisotropy is the inability to model microstructural fabric (oriented clays and microfractures) and the intrinsic anisotropy of clays. Future modeling would

require higher resolution images to structurally constrain these features and anisotropic elements.

- The method described in this paper provides a new avenue for quantifying the relative impacts of rock microstructural features on velocity anisotropy and estimating rock mechanical properties using SEM and CT imaging combined with elastic wave numerical simulation.
- Potential new applications of the presented method include determining the impact of microfracturing in kerogen phases on dynamic rock properties and determining the impact of layering and fractures on quasi-static mechanical response at large strains.

7.8 SUPPORTING INFORMATION

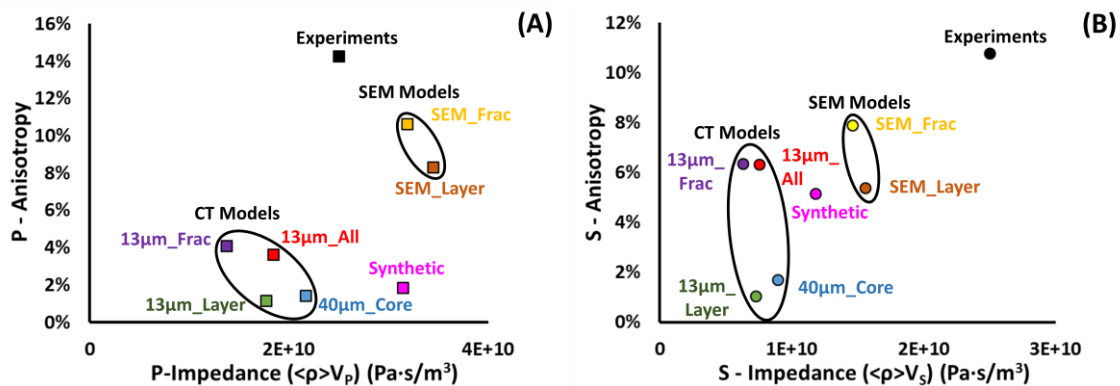


Figure 7-10 Velocity Anisotropy and Impedance for (A) *P*-waves and (B) *S*-waves. Velocity Anisotropy is calculated as $(V_{90^\circ} - V_{0^\circ}) / V_{0^\circ}$, where V_{0° and V_{90° represent the wave velocities perpendicular and parallel to bedding. Impedance is calculated by multiplying the volume average density of each model by its *P*-wave velocity. For consistency, all impedances plotted represent the 0° samples.

8. Conclusions

This study documents the complexity of rock mechanical behavior, which dictates robust mechanical characterization to accurately predict a rock's response to human-induced stress changes during hydrocarbon exploitation. The dissertation research used simultaneous triaxial stress-testing and ultrasonic monitoring, in addition to CT and SEM imaging to highlight the impacts of rock type (sandstone, dolomite, shale), confining stress, stress loading path (isotropic and deviatoric), lithological heterogeneity and layering, and fractures (pre-existing and stress-induced) on static and dynamic mechanical properties and rock failure. My results provide new methods for: (1) detecting the onset of stress-induced microfracturing in isotropic rocks using shear wave crossover (SWX) (changes in shear wave anisotropy), (2) combining measurements from several cores as a function of the % of peak stress to evaluate the deviatoric stress-dependences of anisotropic static and dynamic mechanical properties, (3) developing dynamic-static transforms, which account for stress, anisotropy, and rock damage, and (4) modeling and decoupling the relative impacts of layering and fractures on shale velocity anisotropy by combining CT and SEM imaging to develop mineralogically and structurally heterogeneous velocity models.

8.1 SWX FOR IDENTIFYING THE ONSET OF STRESS-INDUCED DAMAGE

Results show that despite the presence of inelastic processes throughout deviatoric loading, elastic models are adequate for describing rock mechanical behavior up to some threshold, after which an inelastic model likely needs to be incorporated. Stress-induced damage has a more appreciable impact on *S*-waves than *P*-waves. Thus, the use of shear wave anisotropy, specifically the SWX, provides a reliable estimate of the onset of inelasticity for isotropic rocks. However, in order to extend this method to anisotropic

rocks, the threshold of 1% anisotropy cannot be used. For example, Mancos samples also exhibit distinct changes in c_{44} and c_{55} with increasing deviatoric stress, but the threshold of 1% does not necessarily capture the onset of these changes. Chapters 5 and 6 show distinct changes in dynamic behavior associated with inelastic processes during deviatoric loading of Mancos Shale. Therefore, rather than using a threshold of 1% anisotropy, detecting changes in the slope of the relationship between shear wave anisotropy and deviatoric stress is a potential method for determining the onset of damage in both isotropic and anisotropic rocks. Using this slope-based method would allow for damage characterization in plugs at all orientations since the initial magnitudes of shear wave anisotropy would not matter.

8.2 USING PERCENT OF PEAK FAILURE STRESS FROM ORIENTED CORES TO EVALUATE THE DEVIATORIC STRESS DEPENDENCES OF ANISOTROPIC MECHANICAL PROPERTIES

Rock mechanical properties change significantly during deviatoric stress loading both due to elastic nonlinearity and the transition from primarily elastic to more inelastic deformational processes. Since anisotropic mechanical properties require measurements from several cores (which exhibit strength variability), we developed a method to quantify these stress-induced mechanical changes by normalizing each measurement with respect to the % of peak failure stress at which it was measured. Results from isotropic rocks in Chapter 4 support this method, where peak stress is linearly related to dynamic and static indicators of the onset of inelastic deformation, the SWX, and PPD (dilation), respectively. By normalizing with respect to peak stress, we quantified changes in anisotropic mechanical properties such as dynamic Young's moduli E_v and E_h , which increase by over 8 GPa and 15 GPa during the first 60% of deviatoric loading, respectively. Understanding the deviatoric stress dependences of these properties can be useful for estimating the mechanical response of rocks to tectonic and human-induced subsurface stress changes.

8.3 DYNAMIC-STATIC TRANSFORMS

Chapters 4, 5, and 6 show that dynamic and static mechanical properties exhibit considerably different responses to changes in stress and damage. During isotropic and early deviatoric loading, both isotropic and anisotropic rocks generally exhibit increases in dynamic and static Young's moduli, with dynamic moduli typically increasing more quickly than static. However, at higher deviatoric stresses, stress-induced damage causes static moduli to decrease, whereas dynamic Young's moduli typically continue to increase or remain fairly constant until failure. For anisotropic rocks, the stress dependences of dynamic and static moduli are further complicated by the influence by bedding orientation and the presence of pre-existing fractures.

Results show that a single tangent moduli is not adequate for describing the complex rock mechanical behavior. Therefore, we developed dynamic-static transforms which account for the changes in stress, damage, and bedding orientation. Dynamic-static transforms are likely only applicable for the rock types from which they were developed. Tested rock types exhibit differences in mineralogy, fabric, diagenetic history, layering, degree of fractures, etc., which all impact their stress-strain behavior and limit generalizing dynamic-static transforms across rock types. The inability to develop an all-encompassing dynamic-static transform further highlights the need to perform this type of in-depth mechanical analyses for all formations in order to understand the baseline rock mechanical properties and range of expected properties under various stress conditions and with changes in damage.

8.4 MICROSTRUCTURAL CONTROLS ON ELASTIC ANISOTROPY

Elastic anisotropy is caused by several lithological features, and the degree of measured anisotropy is strongly a function of the applied stress. Modeling results in

Chapter 7 show that velocity anisotropy in Mancos Shale is a function of mineralogical layering and heterogeneity, the presence of pre-existing fractures and compliant grain boundaries, and rock fabric (oriented grains and pores). When combined, these features account for approximately 86% of the V_p and 78% of the V_s anisotropy measured in the laboratory. Clay intrinsic anisotropy is likely the source of the unaccounted for velocity anisotropy.

Fractures and compliant grain boundaries play an important role in anisotropy because their impact depends on the applied stress. At ambient stress conditions, these features may be open, and thus act as additional pore space, which decreases wave velocities. Since bedding planes act as planes of weakness, most pre-existing fractures in Mancos samples were parallel to bedding, they had an appreciable impact on velocity anisotropy at low stresses. However, when samples were loaded in the direction perpendicular to bedding, anisotropy decreased dramatically due to the closure of these compliant features.

In addition to pre-existing fractures, stress-induced fractures and damage increased shear-wave anisotropy in isotropic and anisotropic rocks at high deviatoric stresses. The formation and subsequent dilation of stress-induced fractures caused an increase in pore space. However, the relative impact of fractures depends on their orientation with respect to the orientation of each measurement axis. Therefore, waves with particle motion perpendicular to fractures exhibited decreased velocities, whereas those waves with particle motion parallel to fractures exhibited little to no change in velocity. Decoupling and quantifying the relative impacts that fractures and other lithological features have on velocity anisotropy at the core scale may provide value for accurately estimating rock structural heterogeneity and mechanical properties from larger well-log and scale seismic measurements.

Appendix: Recommendation for Best Practices: Sample Preparation and Laboratory Measurements

Triaxial stress testing requires careful sample preparation. Plug geometry and dimensions are two of the most important factors for reliable test results. Core plugs were taken from large quarried blocks, after which an endface grinder was utilized to ensure the sample had parallel and smooth ends. Tests involving samples with non-parallel ends showed inconsistent stress-strain results, including failure upon initial loading, and also tend to exhibit more noise in ultrasonic measurements. Increased noise is believed to be caused by poor coupling between the sample and endcaps, where wave energy can be lost in the gap between the two. In addition to sample geometry, final sample length must be 2 – 2.5 times the sample diameter, which was 25 mm. Proper slenderness is important in order for the rock to develop a true shear plane that does not pass through the end of the sample, and is not altered by sample size. If possible, X-ray microtomography imaging should be performed prior to and post testing, as a quality check for natural microfracturing, as well as for analysis of stress-induced fracture orientation and comparison with static and dynamic measurements.

Proper oscilloscope settings are also necessary for reliable ultrasonic measurements. As stress increases during testing, enhanced endcap coupling and sample compression increase the amplitude of ultrasonic waves. Therefore, the oscilloscope must be set such that the higher amplitude waveforms will be recorded throughout the

anticipated stress range of the test. Oscilloscope setup is done typically after the sample has been “seated”, or in contact with the loading piston, and the appropriate confining stress has been imposed on the sample. At this stress, the waveforms should be barely discernable, and will become more pronounced as stress increases. If the oscilloscope is setup prior to seating and confining the sample, the waveforms will likely grow beyond the recordable amplitude range during the test. Changing oscilloscope setting mid-test will then be required, which may disrupt measurements.

References

- Adachi, J., E. Siebrits, A. Peirce, J. Desroches, 2007, Computer simulation of hydraulic fractures. *International Journal of Rock Mechanics and Mining Sciences*, **44**, 739-757.
- Alsaman, M.E., M.T. Myers, and M.H. Sharf-Aldin, 2015, Comparison of multistage to single stage triaxial tests: American Rock Mechanics Association, ARMA-15-767.
- Amadei, B., 1996, Importance of anisotropy when estimating and measuring in situ stresses in rock. *International Journal of Rock Mechanics and Mining Sciences & Geomechanics Abstracts*. **33**(3) 293-325.
- Anders, M.H., S.E. Laubach, and C.H. Scholz, 2014, Microfractures: a review. *Journal of Structural Geology*, **69**, Part B, 377-394.
- Anderson, D.S., and N.B. Harris, 2006, Integrated sequence stratigraphic and geochemical resource characterization of the lower Mancos Shale, Uinta Basin, Utah. Utah Geological Survey.
- Armstrong, P., B. Chmela, K. Dodds, C. Esmersoy, B. Hornby, S. Leaney, and H. Lynn, 1994, The promise of elastic anisotropy: *Oilfield Review*, **6**, 36-47.
- Ass'ad, J.M., R.H. Tatham, and J.A. McDonald, 1992, A physical model study of microcrack-induced anisotropy: *Geophysics*, **57**, 1562-1570.
- ASTM International, 2014. Standard test methods for compressive strength and elastic moduli of intact rock core specimens under varying states of stress and temperatures. ASTM-D7012-14.
- Ayling, M., P. Meredith, and S. Murrell, 1995, Microcracking during triaxial deformation of porous rocks monitored by changes in rock physical properties, I. Elastic-wave propagation measurements on dry rocks: *Tectonophysics*, **245**, 205-221.
- Backus, G.E., 1962, Long-wave elastic anisotropy produced by horizontal layering. *Journal of Geophysical Research*, **67**(11), 4427-4440.
- Batzle, M.L., G. Simmons, and R.W. Siegfried, 1980, Microcrack closure in rocks under stress: Direct observation: *Journal of Geophysical Research Solid Earth*, **85**, 7072-7090.
- Baud, P., E. Klein, and T. Wong, 2004, Compaction localization in porous sandstones: spatial evolution of damage and acoustic emission activity: *Journal of Structural Geology*, **26**, 603-624.
- Berryman, J.G., 1995, Mixture theories for rock properties. In *Rock Physics & Phase Relations*, T. J. Ahrens (Ed.)

- Bergbauer, S., and D.D. Pollard, 2004, A new conceptual fold-fracture model including prefolding joints, based on the Emigrant Gap anticline, Wyoming. *Geological Society of America Bulletin* **116**(3-4), 294-307.
- Bésuelle, P., J. Desrues, and S. Raynaud, 2000, Experimental characterization of the localization phenomenon inside a Vosges sandstone in a triaxial cell: *International Journal of Rock Mechanics and Mining Sciences*, **37**, 1223-1237.
- Birgenheier, L.P., B. Horton, A.D. Mccauley, C.L. Johnson, and A. Kennedy, 2017, A depositional model for offshore deposits of the lower Blue Gate Member, Mancos Shale, Uinta Basin, Utah, USA. *Sedimentology*, **64**, 1402-1438.
- Bodziak, R., K. Clemons, A. Stephens, and R. Meek, 2014, The role of seismic attributes in understanding the hydraulically fracturable limits and reservoir performance in shale reservoirs: An example from the Eagle Ford Shale, south Texas: *AAPG Bulletin* **98**(11), 2217–2235.
- Bohlen, T., 2002, Parallel 3-D viscoelastic finite difference seismic modelling. *Computers and Geosciences*, 887-899.
- Bornert, M., 2010, X-ray micro CT for studying strain localization in clay rocks under triaxial compression: *Advanced X-ray Tomography of Geomaterials*, **118**, 35.
- Brie, A., T. Endo, D. Hoyle, M. Mueller, D. Codazzi, C. Esmersoy, K. Hsu, S. Denoo, T. Plona, R. Shenoy, and B. Sinha, 1998, *New Directions in Sonic Logging: Oilfield Review*, 40-55.
- Byun, B.S., 1984, Seismic parameters for transversely isotropic media. *Geophysics*, **49**(11), 1908-1914.
- Caia, M., P.K. Kaisera, Y. Tasakab, T. Maejimac, H. Moriokac, and M. Minamic, 2004, Generalized crack initiation and crack damage stress thresholds of brittle rock masses near underground excavations: *International Journal of Rock Mechanics & Mining Sciences*, **41**, 833–847.
- Castagna, J.P., M.L. Batzle, and R.L. Eastwood, 1985, Relationships between compressional-wave and shear-wave velocities in clastic silicate rocks. *Geophysics*, **50**(4), 571-581.
- Chandler, M.R., P.G. Meredith, N. Brantut, and B.R. Crawford, 2016, Fracture toughness anisotropy in shale. *Journal of Geophysical Research: Solid Earth*, **121**(3), 1706-1729.
- Cheng, C.H., and D.H. Johnston, Dynamic and static moduli. *Geophysical Research Letters*, **8**(1), 39-42.
- Ciccotti, M., and F. Mulargia, 2004, Differences between static and dynamic elastic moduli of a typical seismogenic rock. *Geophysical Journal International*, **157**(1), 474-477.

- Collet, O., B. Gurevich, M. Madadi, and M. Pervukhina, 2014, Modeling elastic anisotropy resulting from the application of triaxial stress: *Geophysics*, **79**(5), C135-C145.
- Crampin, S., 1981, A review of wave motion in anisotropic and cracked elastic-media: *Wave Motion*, **3**, 343-391.
- Crampin, S., and R. McGonigle, 1981, The variation of delays in stress-induced anisotropic polarization anomalies: *Geophysical Journal International*, **64**, 115-131.
- Crampin, S., 1985, Evaluation of anisotropy by shear-wave splitting. *Geophysics*, **50**(1), 142-152.
- de Almeida, C.M.C., R.L.C. Melo, B.B. Holzberg, and C. Guimaraes, 2008, Using open and cased hole sonic anisotropy for hydraulic fracturing evaluation: A case study – Carmopolis Field, northeast Brazil: *International Petroleum Technology Conference*, IPTC-12183.
- de Figueiredo, J.J.S., J. Schleicher, R.R. Stewart, and N. Dyaour, 2012, Estimating fracture orientation from elastic wave propagation: An ultrasonic experimental approach: *Journal of Geophysical Research*, **117**, B08304.
- De Paola, N., D.R. Faulkner, and C. Collettini, 2009, Brittle versus ductile deformation as the main control on the transport properties of low-porosity anhydrite rocks: *Journal of Geophysical Research Solid Earth*, **114**, B06211.
- Dewhurst, D.N., and A.F. Siggins, 2006, Impact of fabric, microcracks and stress field on shale anisotropy. *Geophysics Journal International*, **165**, 135-148.
- Dillen, M.W.P., H.M.A. Cruts, J. Groenenboom, J.T. Fokkema, and A.J.W. Duijndam, 1999, Ultrasonic velocity and shear-wave splitting behavior of a Colton sandstone under a changing triaxial stress: *Geophysics*, **64**, 1603-1607.
- Donald, A., and T. Bratton, 2006, Advancements in acoustic techniques for evaluating open natural fractures: *Society of Petrophysicists and Well Log Analysts 47th Annual Logging Symposium*, Veracruz, Mexico June 4-7.
- Donald, J. A., R. Prioul, T. Lei, and B. Sinha, 2013, Stress characterization in deep boreholes using acoustoelasticity, in X.-T. Feng, J. A. Hudson, and F. Tans, eds., *Rock characterisation, modelling and engineering design methods*: Taylor & Francis Group, 309–314.
- Donald, J.A., E.J. Wielemaker, F. Karpfinger, F. Gomez, X. Liang, and M. Tingay, 2015, Qualifying stress direction from borehole shear sonic anisotropy. *American Rock Mechanics Association*, 15-364.
- Donald, J. A., and R. Prioul, 2015, In situ calibrated velocity-to-stress transforms using shear sonic radial profiles for time-lapse production analysis. *The Leading Edge: Borehole geophysics and sonic logging*, 286-294.

- Eberhart-Phillips, D., D-H. Han, and M.D. Zoback, 1989, Empirical relationships among seismic velocity, effective pressure, porosity, and clay content in sandstone: *Geophysics*, **54**, 82-89.
- Eberhardt, E., D. Stead, B. Stimpson, and R.S. Read, 1998, Identifying crack initiation and propagation thresholds in brittle rock. *Canadian Geotechnical Journal*, **35**(2), 222-233.
- U.S. Energy Information Administration (EIA), 2018, Annual Energy Outlook.
- Fang, X., M. Fehler, Z. Zhu, T. Chen, S. Brown, A. Cheng, and M. N. Toksoz, 2013, An approach for predicting stress-induced anisotropy around a borehole. *Geophysics*, **78**(3), D143-D150.
- Far, M.E., J.A. Quirein, and N. Mekic, 2016, Geomechanics of Orthorhombic Media. *Petrophysics*, **57**, 588-596.
- Fisher, M.K., C.A.M. Wright, B.M. Davidson, E.O. Fielder, W.S. Buckler, and N.P. Steinsberger, 2002, Integrating Fracture Mapping Technologies to Optimize Stimulations in the Barnett Shale. Society of Petroleum Engineers SPE-77441.
- Fjaer, E. 1999. Static and dynamic moduli of weak sandstones. American Rock Mechanics Association The 37th U.S. Symposium on Rock Mechanics (USRMS), 7-9 June, Vail, Colorado.
- Fjaer, E. 2008, Petroleum Related Rock Mechanics: Elsevier Publishing.
- Fjaer, E. 2009, Static and dynamic moduli of a weak sandstone: *Geophysics*, **74**(2), WA103-WA112.
- Fjaer, E., and O.M. Nes, 2013, Strength anisotropy of Mancos shale. American Rock Mechanics Association 47th US Rock Mechanics / Geomechanics Symposium held in San Francisco, CA, USA, 23-26 June.
- Fortin, J., Y. Gueguen, and A. Schubnel, 2007, Effects of pore collapse and grain crushing on ultrasonic velocities V_p/V_s : *Journal of Geophysical Research Solid Earth*, **112**, B08207.
- Fortin, J., S. Stanchits, G. Dresen, and Y. Gueguen, 2009, Acoustic emissions monitoring during inelastic deformation of porous sandstone: comparison of three modes of deformation: *Rock Physics and Natural Hazards*, **166**, 823-841.
- Frydman, M., F. Pacheco, J. Pastor, F.C. Canesin, J. Caniggia, and H. Davey, 2016, Comprehensive determination of the far-field earth stresses for rocks with anisotropy in tectonic environment. SPE Argentina Exploration and Production of Unconventional Resources Symposium, 1-3 June, Buenos Aires Argentina.
- Gale, J.F.W., S.E. Laubach, J.E. Olson, P. Eichhubl, and A. Fall, 2014, Natural fractures in shale: a review and new observations. *AAPG Bulletin*, **98**(11), 2165-2216.

- Gale, J.F.W., R.M. Reed, and J. Holder, 2007, Natural fractures in the Barnett Shale and their importance for hydraulic fracture treatments: *AAPG Bulletin*, **91**, 603-622.
- Gao, Y. and S. Crampin, 2003, Temporal variations of shear-wave splitting in field and laboratory studies in China: *Journal of Applied Geophysics*, **54**, 279–287
- Gatelier, N., F., Pellet, and B. Loret, 2002, Mechanical damage of an anisotropic porous rock in cyclic triaxial tests: *International Journal of Rock Mechanics and Mining Sciences*, **39**, 335-354.
- Germanovich, L.N., and D.K. Astakhov, 2004, Fracture closure in extension and mechanical interaction of parallel joints. *Journal of Geophysical Research*, **109**(B2).
- Goldfarb, E.J., K. Ikelda, and N. Tisato, 2017, Segmentation-less digital rock physics using different effective medium theories, *SEG Technical Program Expanded Abstracts*, 3908-3913.
- Grechka, V., and M. Kachanov, 2006, Seismic characterization of multiple fracture sets: Does orthotropy suffice?: *Geophysics*, **71**(3), D93-D105.
- Grigg, J.J., 2016, Macroscopic and microscopic controls on mechanical properties of mudstones. Master of Science Thesis, New Mexico Institute of Mining and Technology.
- Gueguen, Y., and V. Palciauskas, 1994, *Introduction to the physics of rocks*. Princeton University Press.
- Gueguen, Y. and A. Schubnel, 2003, Elastic wave velocities and permeability of cracked rocks: *Tectonophysics*, **370**, 163-176.
- Gurevich, B., M. Brajanovski, R.J. Galvin, T.M. Müller, and J. Toms-Stewart, 2009, P-wave dispersion and attenuation in fractured and porous reservoirs-poroelasticity approach: *Geophysical Prospecting*, **57**, 225-237.
- Gurevich, B., M. Pervukhina, and D. Makarynska. 2011, An analytical model for stress-induced anisotropy of dry rocks. *Geophysics*, **76**(3), WA125–WA133.
- Guyer, R.A., P.A. Johnson, 2009, *Nonlinear mesoscopic elasticity: The complex behavior of granular media including rocks and soil*. Wiley-VCH Verlag GmbH & Co. KGaA.
- Hancock, P.L., 1985, Brittle microtectonics: principles and practice. *Journal of Structural Geology*, **7**(3-4), 437-457.
- Hazzard, J.F., R.P. Young, and S.C. Maxwell, 2000, Micromechanical modeling of cracking and failure in brittle rocks: *Journal of Geophysical Research*, **105**, 16683-16697.

- Herwanger, J.V., and S.A. Horne, 2009, Linking reservoir geomechanics and time-lapse seismics: Predicting anisotropic velocity changes and seismic attributes. *Geophysics*, **74**(4), W13-W33.
- Hill, R. 1952, The elastic behavior of a crystalline aggregate. *Proceedings of the Physical Society, Section A* **65**, 349-354.
- Hoek, E., C. Carranza-Torres, and B. Corkum, 2002, Hoek-Brown failure criterion-2002 edition. *Proceedings of North American Rock Mechanics Symposium-Tunnelling Association of Canada*, **1**, 267-273.
- Holt, R.M., P. Ingsoy, and M. Mikkelsen, 1989, Rock mechanical analysis of North Sea reservoir formations. Society of Petroleum Engineers, SPE Formation Evaluation.
- Holt, R.M., O.M. Nes, J.F. Stenebraten, and E. Fjaer, 2012, Static vs dynamic behavior of shale. American Rock Mechanics Association 46th US Rock Mechanics / Geomechanics Symposium held in Chicago, IL, USA, 24-27 June.
- Holt, R.M., E. Fjaer, and A. Bauer, 2013, Static and Dynamic Moduli – so equal, and yet so different. American Rock Mechanics Association 47th US Rock Mechanics / Geomechanics Symposium held in San Francisco, CA, USA, 23-26 June.
- Horii, H. and S. Nemat-Nasser, 1985, Compression-induced microcrack growth in brittle solids: axial splitting and shear failure: *Journal of Geophysical Research Atmospheres*, **90**, 3105-3125.
- Horsrud, P. 2001, Estimating Mechanical Properties of Shale from Empirical Correlations. Society of Petroleum Engineers Drilling and Completion, **16**, 68-73.
- Hudson, J.A., 1981, Wave speeds and attenuation of elastic waves in material containing cracks: *Journal of Geophysical Research*, **64**, 133-150.
- Jaeger, J., N. Cook, and R. Zimmerman, 2009, *Fundamentals of Rock Mechanics*: Wiley Publishing.
- Jakobsen, M., and T.A. Johansen, 2001, Determination of the elastic properties of shales using single test specimens. *Advances in Anisotropy: Selected Theory, Modeling and Case Studies*, 143-157.
- Jin, G., S.S. Ali, and A.A. Al Dhamen, 2016, Mechanical Anisotropy of Unconventional Shale – Build the Correct Relationship between Static and Dynamic Properties. Society of Petroleum Engineers Abu Dhabi International Petroleum Exhibition & Conference, 7-10 November, Abu Dhabi, UAE.
- Johnson, J.E., and N.I. Christensen, 1995, Seismic anisotropy of shales. *Journal of Geophysical Research*, **100**(B4), 5991-6003.
- Johnson, P.A., and P.N.J. Rasolofosaon, 1996, Nonlinear elasticity and stress-induced anisotropy in rock: *Journal of Geophysical Research*, **101**, 3113-3124.

- Lacy, L.L., 1997, Dynamic Rock Mechanics Testing for Optimized Fracture Designs. Society of Petroleum Engineers SPE Annual Technical Conference and Exhibition. 5-8 October, San Antonio, Texas.
- Laubach, S.E., J.E. Olson, and J.F.W. Gale, 2004, Are open fractures necessarily aligned with maximum horizontal stress? *Earth & Planetary Science Letters*, **222**(1), 191-195.
- Laubach, S.E., J.E. Olson, M.R. Gross, 2009, Mechanical and fracture stratigraphy. *AAPG Bulletin*, **93**(11), p. 1413-1426.
- Laubach, S.E, P. Eichhubl, C. Hilgers, R.H. Lander, 2010, Structural diagenesis. *Journal of Structural Geology*, **32**(12), 1866-1872.
- Laubach, S.E., A. Fall, L.K. Copley, R. Marrett, and S. Wilkins, 2016, Fracture porosity creation and persistence in a basement-involved Laramide fold, Upper Cretaceous Frontier Formation, Green River Basin, U.S.A. *Geological Magazine* **153**(5/6), 887-910.
- Lee, H.P., Olson, J.E., Holder, J., Gale, J.F.W., Myers, R. 2015. The interaction of propagating opening mode fractures with pre-existing discontinuities in shale. *Journal of Geophysical Research: Solid Earth*, **120**(1), 169–181.
- Lei, T., B.K. Sinha, and M. Sanders, 2012, Estimation of horizontal stress magnitudes and stress coefficients of velocities using borehole sonic data. *Geophysics*, **77**, WA181-WA196.
- Lenoir, N., M. Bornert, J. Desrues, P. Bésuelle, and G. Viggiani, 2007, Volumetric digital image correlation applied to X-ray microtomography images from triaxial compression tests on argillaceous rock. *Strain*, **43**, 193-205.D.
- Liming, L., and E. Fjaer, 2012, Modeling of stress-dependent static and dynamic moduli of weak sandstones. *Journal of Geophysical Research*, **117**, B05206.
- Liu, E., and A. Martinez, 2013, *Seismic Fracture Characterizaion*: EAGE Publications.
- Lo, T., K.B. Coyner, and M.N. Toksoz, 1986, Experimental determination of elastic anisotropy of Berea sandstone, Chicopee shale, and Chelmsford granite. *Geophysics*, **51**, 164-171.
- Lockner, D.A., 1993, The role of acoustic emission in the study of rock fracture: *International Journal of Rock Mechanics and Mining Sciences & Geomechanics Abstracts*, **30**, 883-899.
- Lockner, D. A., 1995, *Rock failure, Rock Physics & Phase Relations: A Handbook of Physical Constants*: Cambridge University Press. 127-147.
- Madadi, M., M. Pervukhina, and B. Gurevich, 2013, Modelling elastic anisotropy of dry rocks as a function of applied stress: *Geophysical Prospecting*, **61**, 391 - 403.

- Mainprice, D., and M. Humbert, 1994, Methods of calculating petrophysical properties from lattice preferred orientation data. *Surveys in Geophysics*, **15**, 575-592.
- Mainprice, D., R. Hielscher, and H. Schaeben, 2011, Calculating anisotropic physical properties from texture data using the MTEX open-source package. *Geological Society of London, Special Publications*, **360**, 175-192.
- Marion, D., Mukerji, T., Mavko, G. 1994. Scale effects on velocity dispersion: From ray to effective medium theories in stratified media. *Geophysics*, **59**(10), 1613-1619.
- Mavko, G., T. Mukerji, and N. Godfrey, 1995, Predicting stress-induced velocity anisotropy in rocks: *Geophysics*, **60**, 1081-1087.
- Mavko, G., T. Mukerji, and J. Dvorkin, 2009, *The rock physics handbook: tools for seismic analysis of porous media*. 2nd edition: Cambridge University Press.
- Mayerhofer, M.J., E.P. Lolon, N.R. Warpinski, C.L. Cipolla, D. Walser, and C.M. Rightmire, 2010, What is Stimulated reservoir volume?. *SPE Production and Operations*, 89-98.
- McCall, K. R., and R. A. Guyer, 1994, Equation of state and wave propagation in hysteretic nonlinear elastic materials, *Journal of Geophysical Research*, **99**(B12), 23,887-23,897.
- Melaku, M.T., 2007, Velocity anisotropy of shales and sandstone from core samples and well logs on the Norwegian continental shelf. Master's Thesis, University of Oslo.
- Melendez-Martinez, J., and D.R. Schmitt, 2016, A comparative study of the anisotropic dynamic and static elastic moduli of unconventional reservoir shales: Implication for geomechanical investigations. *Geophysics*, **81**(3), D245-D261.
- Mikhaltsevitch, V., N. Lebedevm and B. Gurevich, 2016, A laboratory study of the elastic anisotropy in the Mancos shale at seismic frequencies. *SEG International Exposition and 86th Annual Meeting*, 3174-3178.
- Milliken, K.L., and R.M. Reed, 2010, Multiple causes of diagenetic fabric anisotropy in weakly consolidated mud, Nankai accretionary prism, IODP Expedition 316. *Journal of Structural Geology*, **32**(12), 1887-1898.
- Mody, F.K., U., Tare, and G. Wang, 2007, Sustainable deployment of geomechanics technology to rescuing well construction costs. *SPE/IADC Middle East Drilling Technology Conference and Exhibition*, 22-24 October Cairo, Egypt SPE/IADC 108241.
- Mokhtari, M., B.T. Bui, and A.N. Tutuncu, 2013, Tensile failure of shales: Impacts of layering and natural fractures. *SPE Western North American and Rocky Mountain Joint Regional Meeting* 16-18 April, Denver, Colorado.
- Mokhtari, M., B.T., Bui, and A.N. Tutuncu, 2014, Tensile failure in shales: impacts of layering and natural fractures. *Society of Petroleum Engineers Western North*

- American and Rocky Mountain Joint Meeting, 17-18 April, Denver, Colorado SPE-169520.
- Nelson, R. A., 1985, Geologic analysis of naturally fractured reservoirs: Houston, Gulf Publishing.
- Nemat-Nasser, S., and M. Obata, 1988, A microcrack model of dilatancy in brittle materials: *Journal of Applied Mechanics*, **55**, 24-35.
- Nur, A., and G. Simmons, 1969, Stress-induced velocity anisotropy in rocks: An experimental study: *Journal of Geophysical Research*, **74**, 6667-6674.
- Nur, A., 1971, Effects of stress on velocity anisotropy in rocks with cracks, *Journal of Geophysical Research*, **76**(8), 2022-2034.
- Nur, A., Mavko, G., Dvorkin, J., Galmudi, D., 1998, Critical porosity: a key to relating physical properties to porosity in rocks. *The Leading Edge*, **17**(3), 357-362.
- Olson, J.E., 2008, Multi-fracture propagation modeling: Applications to hydraulic fracturing in shales and tight gas sands. American Rock Mechanics Association, 08-327.
- Ouchi, H., Katiyar, A., York, J., Foster, J. T., & Sharma, M. M. (2015). A fully coupled porous flow and geomechanics model for fluid driven cracks: a peridynamics approach. *Computational Mechanics*, **55**(3), 561-576.
- Pena, F.J.R, 1999, Elastic properties of sedimentary anisotropic rocks. Massachusetts Institute of Technology Master's Thesis.
- Powell, C. M., 1979, A morphological classification of rock cleavage. *Tectonophysics*, **58**(1-2), 21-34.
- Prioul, R., A. Bakulin, and V. Bakulin, 2001, Three-parameter model for predicting acoustic velocities in transversely isotropic rocks under arbitrary stress: 71st Annual International Meeting, Society of Exploration Geophysicists, Expanded Abstracts, 1732-1735.
- Prioul, R., A. Bakulin, and V. Bakulin, 2004, Nonlinear rock physics model for estimation of 3D subsurface stress in anisotropic formations: theory and laboratory verification: *Geophysics*, **69**, 415-425.
- Prioul, R., A. Donald, R. Koepsell, E. El Marzouki, and T. Bratton, 2007, Forward modeling of fracture-induced sonic anisotropy using a combination of borehole image and sonic logs: *Geophysics*, **72**(4), E135-E147.
- Prioul, R., and J. Jocker, 2009, Fracture characterization at multiple scales using borehole images, sonic logs, and walk around vertical seismic profile: *AAPG Bulletin*, **93**, 1503-1516.
- Prioul, R., Karpfinger, F., Deenadayalo, C., Suarez-Rivera, R. 2011. Improving fracture initiation predictions on arbitrarily oriented wells in anisotropic shales. *Canadian*

- Society for Unconventional Gas, Canadian Unconventional Resources Conference held in Calgary, Alberta, Canada, 15-17 November.
- Pyrak-Nolte, L.J., L.R. Myer, and N.G.W. Cook, 1990, Transmission of seismic waves across single natural fractures: *Journal of Geophysical Research*, **95**, 8617-8638.
- Ramos, M.J., D.N. Espinoza, C. Torres-Verdin, K.T. Spikes, and S.E. Laubach, 2017, Stress-Dependent Dynamic-Static Transforms of Anisotropic Mancos Shale. *American Rock Mechanics Association*, 17-182.
- Ramos, M.J., D.N. Espinoza, C. Torres-Verdin, and T. Grover, 2017. Use of s-wave anisotropy to quantify the onset of stress-induced microfracturing. *Geophysics*, **82**(6), MR201-MR212.
- Ramos, M.J., D.N. Espinoza, S.E. Laubach, and C. Torres-Verdin, (Undergoing Review), Quantifying static and dynamic stiffness anisotropy and nonlinearity in finely laminated shales: experimental measurement and modeling.
- Ramos, M.J., D.N. Espinoza, E.J. Goldfarb, N. Tisato, S.E. Laubach, and C. Torres-Verdin, (Undergoing Review), Microstructural Controls on Elastic Anisotropy of Finely Laminated Mancos Shale.
- Rasolofosaon, P., 1998, Stress-induced seismic anisotropy revisited. *Oil & Gas Science and Technology - Rev. IFP*, **53**(5), 679-692.
- Rawling, G.C., P. Baud, and T. Wong, 2002, Dilatancy, brittle strength, and anisotropy of foliated rocks: experimental deformation and micromechanical modeling: *Journal of Geophysical Research*, **107**, 2234.
- Roussel, N.P., and M.M. Sharma, 2011, Optimizing fracture spacing and sequencing in horizontal-well fracturing. *SPE Production and Operations*, 173-184.
- Santos, L.K., J.J.S. de Figueiredo, B. Omoboya, J. Schleicher, R.R. Stewart, and N. Dyaour, 2015, On the source-frequency dependence of fracture-orientation estimates from shear-wave transmission experiments: *Journal of Applied Geophysics*, **114**, 81-100.
- Sarkar, D., A. Bakulin, and R. Kranz, 2003, Anisotropic inversion of seismic data for stressed media: theory and a physical modeling study on Berea Sandstone. *Geophysics*, **68**, 690–704.
- Sarker, R., and M. Batzle, 2010, Anisotropic elastic moduli of the Mancos B Shale – an experimental study. *SEG Technical Program Expanded Abstracts 2010*, 2600-2605
- Sarout, J., and Y. Gueguen, 2008, Anisotropy of elastic wave velocities in deformed shales: Part 1- Experimental results. *Geophysics*, **72**(5), D71-D89.
- Sayers, C.M., and Allen, D.R. 1984. The influence of stress on principal polarization directions of ultrasonic shear waves in textured steel plates. *Journal of Physics D: Applied Physics*, **17**(7), 1399-1413.

- Sayers, C.M., J.G. Van Munster, and M.S. King, 1990, Stress induced ultrasonic anisotropy in berea sandstone: *International Journal of Rock Mechanics, Mineral Science and Geomechanics Abstracts*, **27**, 429-436.
- Sayers, C.M., and M. Kachanov, 1995, Microcrack-induced elastic wave anisotropy of brittle rocks: *Journal of Geophysical Research*, **100**, 4149-4156.
- Sayers, C.M., 2002, Stress-dependent elastic anisotropy of sandstones: *Geophysical Prospecting*, **50**, 85-95.
- Sayers, C.M., 2004, Monitoring production-induced stress changes using seismic waves: *SEG Technical Program Expanded Abstracts*: 2287-2290.
- Sayers, C.M., 2004, Seismic anisotropy of shales: What determines the sign of Thomsen's delta parameter?. *SEG, Expanded Abstracts*, 103-106.
- Sayers, C.M., 2005, Seismic anisotropy of shales. *Geophysical Prospecting*, **53**, 667-676.
- Sayers, C.M., 2010, *Geophysics Under Stress: Geomechanical Applications of Seismic and Borehole Acoustic Waves*, Society of Exploration Geophysicists Distinguished Instructor Series.
- Schoenberg, M., and K. Helbig, 1994, Orthorhombic media: modeling elastic wave behavior in a vertically fractured earth: *Geophysics*, **62**, 1954-1974.
- Scholz, C.H., 1968, Microfracturing and the inelastic deformation of rock in compression: *Journal of Geophysical Research*, **73**, 1417-1432.
- Schwartz, L. M., W. F. Murphy III, and J. G. Berryman, 1994, Stress-induced transverse isotropy in rocks: *Society of Exploration Geophysicists Technical Program Expanded Abstracts*, 1081-1085.
- Scott, T. E., Jr., Q. Ma, and J.-C. Roegiers, 1993, Acoustic velocity changes during shear enhanced compaction of sandstone. *International Journal of Rock Mechanics and Mining Sciences & Geomechanics Abstracts*, **30**(7), 763-769.
- Scott, T.E., and Y. Abousleiman, 2005, Acoustic measurements of the anisotropy of dynamic elastic and poromechanics moduli under three stress/strain pathways: *Journal of Engineering Mechanics*, **131**, 937-946.
- Shapiro S. A., 2003, Piezosensitivity of porous and fractured rocks: *Geophysics*, **68**, 482-486.
- Shapiro, S.A., and A. Kaselow, 2005, Porosity and elastic anisotropy of rocks under tectonic stress and pore-pressure changes: *Geophysics*, **70**(5), N27-N38.
- Shen, B., O. Stephansson, H.H. Einstein, B. Ghahreman, 1995, Coalescence of fractures under shear stresses in experiments. *Journal of Geophysical Research*, **100**, 5597-5990.

- Siegesmund, S., J. H. Kruhl, and E. Lüschen, 1996, The significance of rock fabrics for the geological-interpretation of geophysical anisotropies. *Geotectonic Research*, **85**, 163 p.
- Simmons, G., and Brace, W. F., 1965, Comparison of static and dynamic measurements of compressibility of rocks. *Journal of Geophysical Research*, **70**(22), 5649-5656.
- Sinha, B.K., and S. Kostek, 1996, Stress-induced azimuthal anisotropy in borehole flexural waves: *Geophysics*, **61**, 1899-1907.
- Sinha, B.K., and K.W. Winkler, 1999, Formation nonlinear constants from sonic measurements at two borehole pressures: *Geophysics*, **64**, 1890-1900.
- Slatt R.M., and Y. Abousleiman, 2011, Merging sequence stratigraphy and geomechanics for unconventional gas shales. *The Leading Edge*, **30**(3), 274-282.
- Sone, H., and M.D. Zoback, 2013, Mechanical properties of shale-gas reservoir rocks – Part 1: Static and dynamic elastic properties and anisotropy. *Geophysics*, **78**(5), D381-D392.
- Sosa Massaro, A., Espinoza, D. N., Frydman, M., Barredo, S., & Cuervo, S. (2017). Analyzing a suitable elastic geomechanical model for Vaca Muerta Formation. *Journal of South American Earth Sciences*, 79, 472-488.
- Stanchits, S., S. Vinciguerra, and G. Dresen, 2006, Ultrasonic velocities, acoustic emission characteristics and crack damage of basalt and granite: *Pure and Applied Geophysics*, **163**, 974-993.
- Stanchits, S., J. Fortin, Y. Gueguen, and G. Dresen, 2009, Initiation and propagation of compaction bands in dry and wet bentheim sandstone: *Pure and Applied Geophysics*, **166** 843-868.
- Stanchits, S., A. Surdi, E. Edelman, and R. Suarez-Rivera, 2012, Acoustic emission and ultrasonic transmission monitoring of hydraulic fracture initiation and growth in rock samples: 30th European Conference on Acoustic Emission Testing & 7th International Conference on Acoustic Emission, University of Grenada, 12-15 September.
- Suarez-Rivera, R., D. Handwerker, J. Kieschnick, W. Martin, S. Green, 2005, Accounting for heterogeneity provides a new perspective for completions in tight gas shales. *American Rock Mechanics Association*, 05-758.
- Suarez-Rivera, R., Burghardt, J., Stanchits, S., Edelman, E., Surdi, A. 2013. Understanding the effect of rock fabric on fracture complexity for improving completion design and well performance. *International Petroleum Technology Conference*, 26-28 March, Beijing, China.
- Tatham, R.H. 1982, Vp/Vs and lithology. *Geophysics*, **47**(3), 336-344.
- Thomsen, L. 1986. Weak elastic anisotropy. *Geophysics*, **51**, 1954-1966.

- Thurston, R. N., and K. Brugger, 1964, Third-order elastic constants and the velocity of small amplitude elastic waves in homogeneously stressed media. *Physical Review*, **133**, A1604–A1610.
- Timoshenko, S.P., and J.N. Goodier, 1934. *Theory of Elasticity*. New York: McGraw Hill.
- Tisato, N., and K. Spikes, 2016, Computation of effective elastic properties from digital images without segmentation: 86th Annual International Meeting, SEG, Expanded Abstracts, 3256–3260.
- Valcke, S.L.A., M. Casey, G.E. Lloyd, J.-M. Kendall, and Q.J. Fisher, 2006, Lattice preferred orientation and seismic anisotropy in sedimentary rocks. *Geophysical Journal International*, **166**(2), 652-666.
- Vernik, L., and A. Nur, 1992, Ultrasonic velocity and anisotropy of hydrocarbon source rocks. *Geophysics*, **57**(5), 727-735.
- Vernik, L. 1993. Microcrack-induced versus intrinsic elastic anisotropy in mature HC-source shales. *Geophysics*, 58(11) 1703-1706.
- Walsh, J.B., 1965, The effect of cracks on the compressibility of rock: *Journal of Geophysical Research*, **70**, 381–389.
- Wang, Z., H. Wang, M.E. Cates, 2001, Effective elastic properties of solid clays. *Geophysics*, **66**(2), 428-440.
- Wang, Z, 2002, Seismic anisotropy in sedimentary rocks, part 2: Laboratory data. *Geophysics*, **67**(5), 1423-1440.
- Warpinski, N.R., and L.W. Teufel, 1987, Influence of geologic discontinuities on hydraulic fracture propagation. Society of Petroleum Engineers.
- Warpinski, N. R. 1991. Hydraulic fracturing in tight, fissured media. *Journal of Petroleum Technology*, **43**(02), 146-209.
- Wassermann, J., G. Senfaute, D. Amitrano, and F. Homand, 2009, Evidence of dilatant and non-dilatant damage processes in oolitic iron ore: p-wave velocity and acoustic emission analyses. *Geophysical Journal International*, **177**, 1343-1356.
- Winkler, K.W., 1996, Azimuthal velocity variations caused by borehole stress concentrations: *Journal of Geophysical Research*, **101**(B4), 8615-8621.
- Winkler K.W., and X. Liu, 1996, Measurements of third-order elastic constants in rocks: *Journal of the Acoustic Society of America*, **100**, 1392–1398.
- Winkler, K.W., B.K. Sinha, and T.J. Plona, 1998, Effects of borehole stress concentrations on dipole anisotropy measurements: *Geophysics*, **63**, 11-17.
- Wu, K., Olson, J. E., 2015, A simplified three-dimensional discontinuity method for multiple fracture simulations. *International Journal of Fracture*, **193**(2), 191-204.

- Yale, D.P., and W.H. Jamieson Jr, 1994, Static and dynamic rock mechanical properties in the Hugoton and Panoma fields, Kansas. Society of Petroleum Engineers, SPE27939.
- Zhang, J., T.F. Wong., and D.M. Davis, 1990, Micromechanics of pressure-induced grain crushing in porous rocks: Journal of Geophysical Research, **95**, 341 –352.
- Zheng, Z., 2000, Seismic anisotropy due to stress-induced cracks: International Journal of Rock Mechanics and Mining Sciences, **37**, 39-49.
- Zoback, M.D., 2007. Reservoir Geomechanics. Cambridge University Press.